Atomistic Studies of Structure and Dynamics of Aggregation in Solution: From Traditional Surfactant Micelles to Surfactant-Free Microemulsions

Dissertation

zur Erlangung des Doktorgrades
der Naturwissenschaften (Dr. rer. nat.)
der Fakultät für Chemie und Pharmazie
der Universität Regensburg

vorgelegt von
Sebastian Schöttl
aus
Lichtenfels

im Jahr 2018

Promotionsgesuch eingereicht am: 30.05.2018

Die Arbeit wurde angeleitet von: Prof. Dr. Dominik Horinek

Prüfungsausschuss:	Vorsitzender:	Prof. Dr. Joachim Wegener
	1. Gutachter:	Prof. Dr. Dominik Horinek
	2. Gutachter:	Prof. Dr. Thomas Zemb
	Weiterer Prüfer:	Prof. Dr. Werner Kunz

Abstract

The properties of the micellar structures formed by surfactant molecules in aqueous solution has been a widely discussed topic for the last century. Numerous hypotheses evolved in the effort to characterize the shape, internal structure, and driving force in the emergence of these aggregates. Many of the disputes can be ascribed to the fact that precise examination would require observations on a molecular level, which is difficult to achieve with experimental techniques in such dynamic colloidal systems. Therefore, theories often necessarily rely on the interpretation of circumstantial evidence rather than direct proof. In this study, the subject is approached with atomistic molecular dynamics simulations, that provide atomistic insight into the assembly of micelles formed by the ionic surfactants *n*-octyltrimethylammonium bromide, *n*-decyltrimethylammonium bromide, *n*-dodecyltrimethylammonium bromide, sodium octanoate, and sodium decanoate in water. In the course of these simulations, the spontaneous aggregation of surfactant molecules from initially homogeneous distribution is sampled and data acquisition is progressed far beyond the point where dynamic equilibrium is reached. This converged stage is in each case characterized by a noticeable degree of polydispersity that describes a bell-shaped peak in a histogram of aggregation numbers. Targeted analysis of micelles close to the most probable aggregation number reveals objects of globular shape with a diffuse interfacial region. In this assembly, the molecular subunits preferably occupy certain radial positions with the apolar alkyl tails in the micelle center and the polar groups oriented towards the solvent. Compared to idealized representations, however, this ordering is significantly defused and even the terminal methyl groups have a finite probability to be located at the micelle/water interface. The internal configuration that leads to this occurrence is a combination of a few surfactant molecules constituting a radially aligned molecular scaffold and a number of tangentially attached monomers. In case of the C_X—trimethylammonium bromide micelles, a consequence of this mixed array is a rough aggregate surface with deep crevices that allow for significant water penetration up to a buried hydrophobic core. The anionic species form a notably smoother boundary by tighter packing and comprise a larger water-free region in the micelle center, that, however, still only makes up 40 % of the micelle volume. The immediate solvent shell of the aggregates is characterized by a substantial decrease of water-water hydrogen bonds that is more pronounced in case of the anionic compounds, where the carboxylate group represents a dedicated hydrogen-bonding site. The monomer exchange rate is found to be strongly decelerated with increasing aliphatic tail length and ranges between $10^7\ s^{-1}$ and $10^9\ s^{-1}$ for the cationic and $10^7\ s^{-1}$ and $10^8\ s^{-1}$ for the anionic micelles.

The acquired insights on traditional surfactant micelles provide a useful background for the characterization of aggregation in solutions without surfactants. Speculation on such surfactant-free microemulsions dates back to the 1970s but the idea was dismissed for a long time, not least due to the absence of experimental evidence. Recent studies, however, confirmed this conjecture with direct proof of micelle-like oil-in-water aggregates

in the ternary system water/ethanol/octan-1-ol. The weakly associated structures occur for a certain range of compositions that constitute the so-called “pre-Ouzo region” in the monophasic part of the ternary phase diagram. The hydrotrope ethanol enables the stability of these octanol droplets on the nanometer scale by accumulating to a film at the interface similar to that formed by surfactant molecules in conventional microemulsions. A variety of aggregation numbers is observed, that encompasses a continuous spectrum of nano-ordering. The smaller clusters are of globular shape and feature a roughly radial symmetric assembly with a core region composed of mostly terminal carbon units and an outer shell enriched with hydroxyl groups. This resemblance to traditional micelles fades towards larger aggregation numbers, where increasingly amorphous structures are detected. The system is governed by quick rearrangements and the mechanisms of micelle growth due to inter-particle collisions and shrinkage by decomposition into smaller aggregates play a major role. Not all of the cluster sizes that occur during these fluctuations are equally stable and certain aggregation numbers can be characterized as transitory stages during processes of swelling or depletion. The surfactant-free microemulsion exhibits excellent solubilizing properties for the apolar substances propane and squalene. For the first, the solvation free energy in the micelle interior is close to the favorable value predicted for a similarly composed binary octanol/ethanol solution, whereas the aqueous pseudo-phase poses a poor solvent. In the presence of the C_{30} compound, octanol domains expand to enclose the large organic molecules in comparatively stable structures. This leads to significantly enhanced solubilization over a binary water/ethanol mixture of equal proportions. The primary consequence of the addition of the electrolytes NaI and LiCl is a stabilization of the aggregates via the salting-out of ethanol. Preferential adsorption of I^- or Li^+ at the interface is only weakly observed due to the local accumulation of ethanol and octanol hydroxyl groups that leave little apolar surface exposed. In further analogy to traditional microemulsion systems, oil-in-water aggregation reverses to water-in-oil aggregation in excess of octanol. These two regimes are linked by a bicontinuous region, where the octanol and water pseudo-phases entwine to form a sponge-like network.

Kurzzusammenfassung

Die Eigenschaften von Tensid-Mizellen wurden im letzten Jahrhundert ausgiebig diskutiert. Im Bestreben, ihre Gestalt, ihren inneren Aufbau und die Triebkraft hinter ihrer Entstehung zu verstehen, entstanden zahlreiche Hypothesen. Viele der bestehenden Streitpunkte lassen sich darauf zurückführen, dass eine exakte Charakterisierung Untersuchungen auf molekularer Ebene erfordern würde, die mit experimentellen Methoden für derart dynamische, kolloidale Systeme schwer zu realisieren sind. Aus diesem Grund bauen viele Theorien auf Indizien anstelle von klaren Beweisen auf. In dieser Studie

werden Molekulardynamiksimulationen durchgeführt, um Einblicke in den Aufbau von n-Octyltrimethylammoniumbromid-, n-Decyltrimethylammoniumbromid-, n-Dodecyltrimethylammoniumbromid-, Natriumoctanoat- und Natriumdecanoat-Mizellen in Wasser auf atomarem Niveau zu ermöglichen. Im Laufe dieser Simulationen wird die spontane Mizellbildung in anfänglich homogenen Lösungen beobachtet. Die Aufzeichnung der Trajektorien wird dabei weit über den Zeitpunkt hinaus fortgesetzt, an dem sich ein dynamisches Gleichgewicht einstellt. Dieses ist für alle untersuchten Tenside durch einen beträchtlichen Grad an Polydispersität gekennzeichnet, welche sich in einem glockenförmigen Maximum in der Clustergrößenverteilung widerspiegelt. Eine gezielte Analyse von Mizellen in einem kleinen Bereich um diese wahrscheinlichste Größe charakterisiert diese als runde Objekte mit einer unscharfen Grenzfläche. Die Tensidmoleküle haben innerhalb dieser Strukturen eine gewisse radiale Ordnung, wobei die unpolaren Alkylreste das Zentrum der Mizelle ausmachen und die polaren Kopfgruppen nach außen gerichtet sind. Im Vergleich zu idealisierten Darstellungen ist diese Ordnung jedoch deutlich entschärft und sogar endständige Methylgruppen sind gelegentlich an der Mizelle/Wasser-Grenzfläche zu finden. Dies kann auf eine Dichtomie der internen Konfiguration zurückgeführt werden: Ein Teil der Tensidmoleküle bildet ein Gerüst aus radial angeordneten Kohlenwasserstoffketten aus, an das weitere Moleküle tangential anknüpfen. Im Falle der C_X-trimethylammoniumbromid-Mizellen führt diese räumliche Anordnung zu einer zerklüfteten Oberfläche, die tiefes Eindringen von Wassermolekülen erlaubt. Das anschließende Zentrum der Mizelle hingegen ist wasserfrei. Die anionischen Spezies bilden eine vergleichsweise homogene Oberfläche und schließen durch die dichtere Anordnung einen deutlich größeren hydrophoben Bereich ein, der sich jedoch selbst in diesem Fall nur auf etwa 40 % des Gesamtvolumens beläuft. Wassermoleküle in der unmittelbaren Solvathülle bilden deutlich weniger gegenseitige Wasserstoffbrückenbindungen aus, als außerhalb des Einflussbereichs der Mizellen. Dieser Effekt macht sich für die anionischen Verbindungen aufgrund der Carboxygruppe, die als Akzeptor fungiert, stärker bemerkbar als für die kationischen. Die Austauschrate von Monomeren nimmt schnell mit der Länge der Kohlenstoffkette ab. Für die kationischen Mizellen liegt sie zwischen $10^7\,s^{-1}$ und $10^9\,s^{-1}$; für die anionischen zwischen $10^7\,s^{-1}$ und $10^8\,s^{-1}$.

Die gewonnenen Erkenntnisse über klassische Tensid-Mizellen erweisen sich als nützlich für die Untersuchung der Aggregation in tensidfreien Lösungen. Spekulationen über tensidfreie Mikroemulsionen tauchten erstmals in den 1970er Jahren auf. Allerdings wurde dieser These lange Zeit wenig Aufmerksamkeit geschenkt; nicht zuletzt, weil stichfeste experimentelle Beweise fehlten. Neuere Studien bestätigten diese Spekulationen allerdings vor kurzer Zeit mit dem direkten Nachweis von mizellenartigen Aggregaten im ternären System Wasser/Ethanol/Octan-1-ol. Diese schwach assoziierten Strukturen treten für bestimmte Zusammensetzungen im einphasigen Bereich des ternären Phasendiagramms auf, die den sogenannten „pre-Ouzo“ Bereich definieren. Die Stabilität dieser Octanoltröpfchen auf der Nanometerskala wird durch das Hydrotrop Ethanol gewährleistet. Es reichert sich an der Grenzfläche zu einem Film an, wie ihn Tenside in herkömmlichen Mikroemulsionen bilden. Eine große Spanne an Aggregationszahlen ist die Folge starker Polydispersität,

die ein kontinuierliches Spektrum an strukturellen Charakteristika umfasst. Die kleineren Aggregate sind globulär und der innere Aufbau folgt einer radialen Hierarchie. Die Kernregion besteht überwiegend aus den Methylresten, während die Hydroxylgruppen an der Aggregatsoberfläche angereichert sind. Mit zunehmender Aggregationszahl erscheinen die Octanoldomänen immer ungeordneter und verlieren an Symmetrie, womit die Parallelen zu klassischen Tensidmizellen verschwinden. Das System ist von raschen Umlagerungen gekennzeichnet, im Rahmen derer Zuwachs- und Zerfallsprozesse durch Eingliederung anderer Aggregate und Zerfall in kleinere Aggregate eine wesentliche Rolle spielen. Die auftretenden Octanolcluster sind unterschiedlich stabil und einige Aggregationszahlen fallen als kurzlebige Übergangsgrößen auf. Diese tensidfreie Mikroemulsion zeichnet sich durch sehr gute Solubilisierungseigenschaften hinsichtlich der unpolaren Substanzen Propanol und Squalen aus. Die Bedingungen innerhalb der Octanolmizellen sind für Ersteres ähnlich günstig wie in einer gleichwertigen binären Octanol/Ethanol Lösung, wohingegen die wässrige Pseudophase ein schlechtes Lösungsmittel darstellt. In Gegenwart der C_{30}-Verbindung findet eine grundlegende Umstrukturierung hin zu größeren Aggregaten statt, die in der Lage sind, die großen Moleküle zu umschließen. Das Resultat ist eine deutlich erhöhte Löslichkeit von Squalen im Vergleich zu einem binären Wasser/Ethanol Gemisch. Zugabe der Salze NaI und LiCl führt primär zu einer Stabiliserung der Mizellen aufgrund der Aussalzung von Ethanol. Der zusätzliche Effekt einer Ladungstrennung aufgrund der bevorzugten Adsorption von I^- oder Li^+ an der Grenzfläche macht sich nur schwach bemerkbar. Dies lässt sich durch eine erhöhte Konzentration an Ethanol- und Octanol-Hydroxylgruppen an der Oberfläche erklären, durch die nur wenig unpolare Fläche frei liegt. Analog zu herkömmlichen Mikroemulsionen kehrt sich das Aggregationsverhalten im Überschuss von Octanol um: Statt Öl-in-Wasser-Aggregaten entstehen Wasser-in-Öl-Aggregate. Die beiden Regimes sind verbunden durch eine bikontinuierliche Region, in der die Octanol- und Wasser-Pseudophasen eine schwammähnliche Struktur ausbilden.

Contents

Nomenclature

Acronyms

CMC	critical micelle concentration
COG	center of geometry
GDS	Gibbs dividing surface
IQR	interquartile range
MD	molecular dynamics
RDF	radial distribution function
SBS	smallest bounding sphere
SFME	surfactant-free microemulsion
SWANS	small and wide angle neutron scattering
SWAXS	small and wide angle X-ray scattering
UFME	ultraflexible microemulsion

System Labels

(composition) α	water/ethanol/octanol mixture with molar ratios specified in Table 1.4
(composition) β	water/ethanol/octanol mixture with molar ratios specified in Table 1.4
(composition) γ	water/ethanol/octanol mixture with molar ratios specified in Table 1.4
(composition) I	water/ethanol/octanol mixture with molar ratios specified in Table 1.4
(composition) II	water/ethanol/octanol mixture with molar ratios specified in Table 1.4

(composition) III	water/ethanol/octanol mixture with molar ratios specified in Table 1.4
CAP	binary mixture of water and sodium octanoate with surfactant concentration stated in Table 1.2
DEC	binary mixture of water and sodium decanoate with surfactant concentration stated in Table 1.2
DeTA	binary mixture of water and *n*-decyltrimethylammonium bromide with surfactant concentration stated in Table 1.2
DTA	binary mixture of water and *n*-dodecyltrimethylammonium bromide with surfactant concentration stated in Table 1.2
OTA	binary mixture of water and *n*-octyltrimethylammonium bromide with surfactant concentration stated in Table 1.2

Aliases

t-butanol	*tert*-butyl alcohol, 2-methyl-propan-2-ol
octanol	octan-1-ol
propanol	propan-1-ol

Definitions

Unless otherwise stated, the following conventions are adhered to throughout this work.

Citation Citations are marked by superscript enumerators which identify the respective entries in the "References" section. Direct references to literature are inline elements that are initiated by the token "Ref.", followed by an enumerator. These elements are usually set at the end of the concerning sentence. They may also be placed immediately after the concerning passage to avoid potential confusion with unrelated succeeding text segments. If a citation extends over more than a single sentence, the citation element follows the first pertained instance and all subsequent sentences referring to the same source are terminated with the superscript '$^{id.}$'.

Units Units are chosen with regard to the orders of magnitude of quantities and the standards implemented by the employed software. Except for the frequently used measure of volume, liter, designated by the symbol 'l', which is defined as $1\,\mathrm{l} = 10^{-3}\,\mathrm{m}^3$, all units comply with the SI (International System of Units) standards of notation and are annotated at the corresponding locations in the text. For unitless quantities, annotation may be omitted.

Typography Mathematical objects are distinguished by the typesetting clarified in Table 0.1.

Table 0.1: Mathematical objects by typesetting.

Element	Notation	Example
vector	**upright bold**	$\mathbf{x}$
vector length / scalar quantity	*italic*	x
arithmetic mean	overline	$\bar{\mathrm{x}}$

Symbols Symbols are annotated and defined at the corresponding locations in the text, with the exception of the general specifiers listed in Table 0.2 and the Boltzmann constant k_B.

Table 0.2: Frequently used symbols and linked quantities.

Symbol	Quantity
t	time
T	temperature
q	amount of the momentum transfer $\mathbf{q} = \mathbf{k}_\mathrm{f} - \mathbf{k}_\mathrm{i}$, where $\mathbf{k}_\mathrm{i}$ is the wave vector of the incident particle, and $\mathbf{k}_\mathrm{f}$ the wave vector of the scattered particle

Data precision The greater part of results is obtained through analyses on finite intervals. Numeric values extracted from the results are not exact to the given decimal place, but represent the location of the respective data bin or quantities derived from these values. Other numeric values that are subject to fluctuations, for instance the box edge length, are truncated to the lowest constant decimal place.

Introduction

It is a basic insight, readily verified by grease drops surfacing in a bowl of soup and the lack of alcohol drops floating in a glass of wine, that substances can crudely be categorized into water-soluble and water-insoluble classes.

In a polar dispersion medium like water, non-polar compounds seek to avoid the polar environment, which gave rise to the term *hydrophobicity*[1] (from ancient Greek ὕδωρ *hýdor*, "water"* and φόβος *phóbos* "fear"). A consequence that is macroscopically easily discerned is the partitioning into separate phases. Accordingly, the opposite behavior, good miscibility with water due to polarity or electric charge, is referred to as *hydrophilicity*[id.] (where the second syllable descends from the ancient Greek φίλος *phílos*, "beloved"). If both properties combine in a molecular species, because it consists of e.g. an apolar hydrocarbon tail linked to a polar sulfate group, interesting arrangements are made to accommodate the ambivalent preferences. Owing to their dual character, these substances are summarized under the heading of *amphiphiles*[id.] (where the first syllable derives from the ancient Greek ἀμφί *amphí*, "both").

In low concentrations, amphiphile additives adsorb at the water/air interface in a configuration maintaining immersion of the polar groups, while minimizing contacts between polar tail sections and the solvent.[3] Similarly, adsorption at other existing interfaces may occur, for instance at the walls of the flask containing the solution.[id.] This process entails a decrease in (liquid-vapor) surface tension that progresses until the

*Greek – English translations from Ref. 2.

interface is saturated.[id.] This occurrence instigated the generic title surfactant, which is a contraction of the term **surf**ace **act**ive **a**ge**nt**.[4] Amphiphile molecules may be ionic or uncharged and the category is represented by a wide variety of structures.[5] Two examples from the vast portfolio of known surfactants are shown in Figure 0.1.[id.]

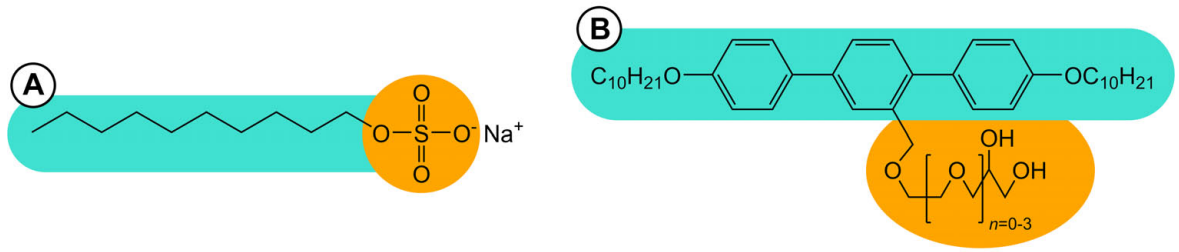

Figure 0.1: Structure formulae of two amphiphilic molecules: **A** the ionic surfactant sodium decyl sulfate and **B** a complex *p*-terphenyl derivate. Polar groups are colored **orange** and apolar groups **turquoise**.

Scientific insight into the phenomena responsible for many of the characteristics of surfactant solutions was scarce when McBain presented his idea of the association of soap molecules into "micelles" in 1913.[6] Years of pondering the strange behavior these mixtures displayed in conductivity experiments above certain concentrations[7,8] led to that conclusion, but the hypothesis did not ab ovo attract approval in the scientific society. In this context it is often pointed anecdotally to the harsh reaction McBain was confronted with during a lecture before the Royal Society of London on the subject,[9,10] to emphasize with which degree of ridicule this proposal was initially met. A search on relevant platforms clearly reveals that this condition did not last and that McBain's speculation turned out to be far from "nonsense". Entries of more than 2000 publications on the subject, if counting only those that are labeled with contiguous compositions of the words "micelle" and "structure" or declinations thereof, attest strong academic interest in the matter. The existence of micellar aggregates is by now unequivocally established and the narrow concentration range in which certain properties of surfactant solutions abruptly change is known as the *critical micelle concentration* (CMC).[11–13]

However, long lasting controversies accompanied the exploration of the topic that are not altogether resolved even now. Initial discussions naturally concerned themselves with the shape of these newly identified structures. Early X-ray data[14] seemed to advocate a lamellar symmetry, which was promoted by Harkins and McBain,[15,16] whereas Debye and Anacker proposed a rod or disk-like geometry.[17] Around the same time, Hartley[18] postulated spherical-ellipsoid objects with a central region consisting of apolar alkyl chains surrounded by an outer shell of polar head groups. This notion was shortly after supported by Reich from an entropic viewpoint[19] and eventually consolidated as general conviction

even before it was bolstered by results from more progressed experimental techniques in the 1980s.[20–22]

Another point of debate was the state of the micelle interior. Opinions diverged on whether the core was fluid-like[23–25] or comparable to a crystalline solid.[26–28] This gave rise to widely different models of assembly, ranging from unordered, convoluted structures[29] over more organized lattice representations,[30] to geometrically strict packing.[31]

Further disagreement prevailed on the topic of water penetration. While STIGTER defended the position of completely dry alkyl chains,[32] which is sometimes referred to as the "reef" model,[33] others portrayed a "fjord" model[id.] in which water permeates the whole micelle,[34] resulting in a core milieu which MULLER described as having "characteristics about midway between those of water and of hydrocarbon".[35] More moderate schemes acknowledged the presence of water to some extent between the polar head group region and a hydrophobic core.[36–38]

Simultaneously, different models were developed to thermodynamically classify micelle formation. On one side, the *mass action model* could gather its share of supporters.[39–43] This approach treats the aggregates as a chemical species that is in equilibrium with free surfactants.[44] On the other side, one found proponents of the *phase separation model* that regards micellar structures as a separated phase from the dispersion medium.[45–49] Refinement of these models led to the *multiple equilibrium model*[50] that removed the disadvantage of the mass action model relying on monodispersity and application of HILL's method of the *thermodynamics of small systems*[51] that corrected shortcomings in the prediction of thermodynamic relations by the phase separation model.

One could argue that the question after the cause of the aggregation of amphiphilic compounds in water was the most unanimously settled. At least in what it is not: it is not the consequence of favorable interactions between the hydrophobic chains as conjectured by DEBYE in the early days.[52] With regard to the apolar moieties it much rather is a passive effect originating from ejection of hydrophobic groups from the aqueous environment. The roots of this so-called "hydrophobic interaction" or "hydrophobic effect" were initially ascribed to a distinct ordering of water molecules in close proximity to a hydrophobic solute by FRANK and EVANS, that was illustrated as "iceberg" formation, on the basis of the temperature dependence of the solubility of hydrocarbon molecules in water.[53] In this light, micellization is a primarily entropy-driven process that minimizes the structurization imposed on water molecules by hydrophobic contacts. This rationale was seriously questioned later by MILLER and HILDEBRAND who attributed the low solubility of apolar subunits to the high cohesive energy in liquid water.[54,55] Over the years, more criticism and various theories surfaced[56–62] and the matter has since then often been addressed in more cautious terms, merely stating that interactions of water with water are more favorable than interactions between water and apolar units.[63] The issue is not satisfactorily resolved to date, leading to a lively ongoing discussion on how to interpret the phenomenon.[64–68]

Without regard to the different scientific stances on many subjects in the field, surfactants were employed in abundancy in the 20th century and have been long before. The most

common application of amphiphiles is certainly soap, that can be retraced to ancient Egypt and beyond.[69] The first targeted modeling of surfactants for industrial purposes is documented in the mid-1800s in the context of the burgeoning textile industry.[70] The sophisticated processing of raw cotton and wool into textile fabrics necessitated dedicated dispersing, softening, and sizing agents.[id.] Nowadays*, surfactant manufacturing is a prosperous industrial branch with a global production volume of 11 million tonnes annually and a market value of 35.7 billion euro in Europe alone.[71] The majority of this capacity is accounted for by cleaning products ranging from industrial and household detergents to personal care and toiletry applications.[id.] Another substantial sector attends to various agrochemical and industrial areas of application where surfactants are deployed as emulsifiers, foaming agents, wetting agents, penetration agents, and so forth.[id.]

A unique feature of these multi-domain systems that is frequently exploited is the possibility to disperse even entirely hydrophobic substances that are otherwise insoluble in water and would just settle as a separate phase.[72] In the literature, this third constituent is usually plainly tagged "oil". The same applies in reverse: a continuous oil phase enriched with an amphiphile can hold significant amounts of water.[id.] The solubilization power of surfactant mixtures is naturally limited and the relative composition and mutual interaction profiles determine the distribution of components.[73] An extensive description of such systems dates back to WINSOR, who identified four different regimes ("Winsor I, II, III, IV"):[74–76]

Type I An organic oil is in equilibrium with a solution of surfactant in water. Some oil is dispersed in the aqueous phase.

Type II Water is in equilibrium with a solution of surfactant in organic oil. Some water is dispersed in the oil phase.

Type III Separate phases of water and organic oil are in equilibrium with a solution of all three components.

Type IV Only one phase exists, consisting of water, oil, and surfactant.

In 1969, EKWALL reported that the solubilization capacity can be greatly enhanced by the presence of a further amphiphilic species, termed *co-surfactant*.[77] Additional adsorption of this compound at the domain boundaries can result in a drastic reduction of interfacial tension, that may even reach zero.[78] For ultra-low interfacial tension, the leading term in the free energy of the structures is the bending energy.[id.] The morphology then depends on the bending elastic moduli and spontaneous curvature, as well as the volume fractions of the components.[79] A high bending rigidity paired with low spontaneous curvature can promote organization into highly ordered mesostructures.[80] Yet the value of the bending constant can approach values lower than $k_{\mathrm{B}}T$, in which case macroscopically disordered bicontinuous entities or separated droplets emerge.[81] The consequence is

*at the 2006 level

the spontaneous formation of macroscopically isotropic and thermodynamically stable liquid-liquid dispersions.[82–84] Owing to the minuscule domain sizes, those systems were conceptualized as *microemulsions* by SCHULMAN et al. in 1959[85] succeeding the pioneering work of HOAR and SCHULMAN on the matter in the 1940s.[86] For lack of a rigorous definition, the term was initially used with some ambiguity and led to confusion.[87] The current IUPAC recommendation stipulates a microemulsion as a "Dispersion made of water, oil, and surfactant(s) that is an isotropic and thermodynamically stable system with dispersed domain diameter varying approximately from 1 to 100 nm, usually 10 to 50 nm."[88] These requirements decidedly distinguish microemulsions from regular emulsions. The latter are not thermodynamically stable but instead are generated from immiscible liquids by applying mechanical shear and merely represent a temporary state in the process of macroscopic phase separation.[89] The definition further hints that a co-surfactant is not absolutely necessary and it should be clarified that microemulsions can also be obtained in ternary systems.[90] However, this is not generally true for every substance from the extensive class of surfactants. The ionic amphiphile *sodium dodecyl sulfate*, for instance, does not produce a microemulsion unless it is supplemented by a co-surfactant.[91] In other cases, the tendency of a solution to form a balanced microemulsion can be significantly tuned with a co-surfactant such as a short-chain alcohol.[92]

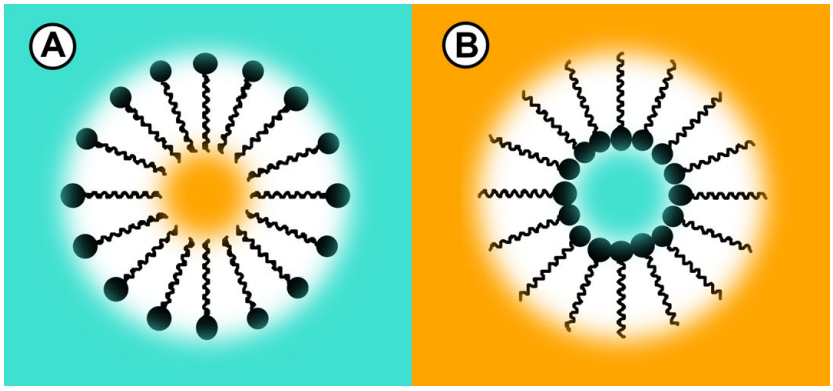

Figure 0.2: Schematic view of **A** an oil-in-water and **B** a water-in-oil micelle. Surfactant molecules are shown in **black**, where the aliphatic tail is sketched in a line representation of the carbon chain and the polar head groups are accentuated as discs. The water phase is illustrated in continuous **turquoise** and the oil-phase in **orange**.

As already mentioned, the structural characteristics of the microemulsion domains can vary. In the simplest case they are globular water-in-oil or oil-in-water inclusions as depicted in Figure 0.2, but possible textures extend to mesophases with e.g. lamellar, hexagonal, or cubic symmetry.[93]

Some time during the late 1970s, when many of the debates on amphiphile solutions were still in full swing,[94] the first reports on structurization in systems free of conventional surfactants materialized.[95–97] These "detergent free microemulsions" in

hexane/water/propan-2-ol showed similarities to ordinary microemulsions in that they were optically clear and stable. It was contemplated by the authors that the addition of alcohol lowered the water-oil interfacial tension and thus enabled the formation of dispersed droplets, but no complete theoretical description evolved. The theme was picked up again around 1990, yet the underlying processes were still poorly understood.[98–100]

Interest in this class of systems was renewed through a study by KLOSSEK et al. in 2012.[101] The subject of investigation was the ternary system water/ethanol/octan-1-ol (from here on after simply referred to as *octanol*), which is characterized by a miscibility gap in the ternary phase diagram due to the immiscibility of water and octanol as displayed in Figure 0.3. Dynamic and static light scattering measurements revealed the presence of micelle-like octanol aggregates well within the one-phase region. To clearly demarcate this occurrence from the "Ouzo effect" described earlier by VITALE and KATZ[102] in the same type of system, the authors coined the term "pre-Ouzo effect". The former is the consequence of a binodal decomposition that takes place upon rapid dilution of a monophasic mixture with water, just barely crossing the phase boundary. The result then is the formation of octanol droplets on the micrometer scale that are stable over the course of days. The similarities of the system to the Greek beverage ouzo, in that the liquor primarily consists of water, ethanol, and the water-insoluble compound *trans*-anethole and is also subject to phase separation upon dilution with water, is responsible for the catchy name.

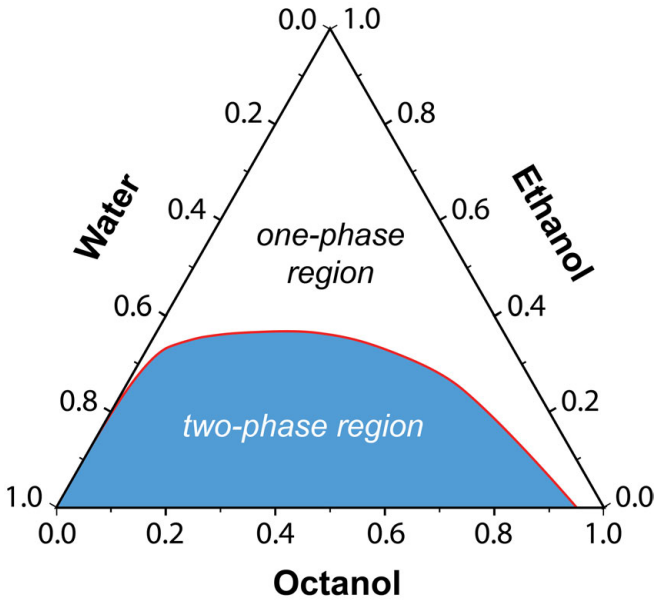

Figure 0.3: Ternary phase diagram of water/ethanol/octanol. The two-phase region is colored in **blue**, the decomposition line in **red**, and the monophasic region is blank. Values are given in weight fraction.*

*Shape and location of the one- and two-phase region reconstructed from **Figure 1. a)** in Ref. 101.

By contrast, the structures identified in the one-phase region are not the result of a metastable emulsification process and, with domain sizes in the nanometer range, manifest at substantially different length scales. Taking into account the earlier descriptions, the precondition for the emergence of this type of *surfactant-free microemulsion* (SFME) in ternary solutions was narrowed down to the combination of two hardly miscible components (water and octanol) with a third that is well soluble in both (ethanol). In the present case, the third species, ethanol, is a classical *hydrotrope*[*].

Nano-structuring was also observed when octanol was substituted by benzyl alcohol, ethyl lactate, or γ-valerolactone[103] and it is assumed that SFMEs always occur for certain compositions in the one-phase region of systems that exhibit an Ouzo region.[104] This supposition was indeed confirmed by LUCIA et al. for the ouzo-like system water/eugenol/ethanol, which showed promising capability in solubilizing the insecticide *imidacloprid* with no detectable changes in structurization.[105]

Other instances have been reported in commercially available mosquito repellents, eaux de toilette and eaux de parfum that do not rely on surfactants.[106,107] A succeeding study by TCHAKALOVA et al. concluded that the performance of these fragrance formulations is strongly influenced by the presence of a pre-Ouzo region:[108] when the liquid phase reaches this composition during the process of evaporation, increased fragrant activity is detected. Moreover, reports by KHMELNITSKY et al.[98,99] and ZOUMPANIOTI et al.[109–111] accentuate the potential of SFMEs in biotechnology by means of *n*-hexane / short-chain alcohol / water model systems. It was found that enzymes such as cholesterol oxidase[98,99] or lipases from *Rhizomucor miehei* and *Candida antarctica*[109–111] retained their catalytic activities in these microheterogeneous media. In the latter study, enzymatic stability was even increased over surfactant-based microemulsions.

Due to their sub-microscopic dimensions, giving a comprehensive account of the involved structures with solely experimental techniques is problematic. For that reason, further probing of the reference pre-Ouzo system water/ethanol/octanol was supplemented by atomistic molecular dynamics (MD) simulations. In conjunction with conductivity and contrast variation neutron scattering experiments, the microemulsion-like character of the pre-Ouzo composition was tied to the presence of micellar octanol aggregates, coated by an interfacial film of ethanol.[112–114] The bending constant of this mixed interface is expected to be lower than $0.1\,k_\mathrm{B}T$, which motivated the label "ultraflexible microemulsion" (UFME) in extension to the established classification of microemulsions into stiff and flexible types.[115] Without disregard for this conceptual delimitation, the general term SFME will be used throughout this work, since the common features of, and differences between surfactant aggregates and surfactant-free aggregates are a thematic focus.

A core theme of the present thesis is a detailed characterization of ternary mixtures with ouzo-type instabilities by means of the model system water/ethanol/octanol. It is the continuation of an earlier work that was prepared in 2013[116] and published in Ref. 114. So

[*]Cf. infobox at the end of this section.

far, investigations were restricted to compositions for which oil-in-water aggregates form. In order to establish further parallels between this type of SFME and microemulsions relying on surfactants, it is vital to extend research to other regions of the phase diagram. Apart from helping to achieve a comprehensive phenomenological description it is also desirable from an application-oriented standpoint to determine whether further morphologies, like bicontinuous structures or reverse water-in-oil micelles, emerge. Besides, little is known about the dynamic properties of the pre-Ouzo aggregates and the response of the system to additives. The structural properties of octanol micelles have been addressed in Ref. 114, but the polydispersity of aggregates moreover necessitates a differentiating examination and the shape is not yet quantitatively delineated. This is certainly no complete account of unresolved issues, which further substantiates the motivation to continue this line of investigation.

A sensible point of reference for such considerations are structures formed by surfactant molecules. However, as the preceding explanations highlight, surfactant micelles are themselves far from being completely understood. Extensive studies involving computer simulations were long believed to be of great value,[117] but have only incrementally been made possible during the last two decades by continuous progress in CPU (and more recently relevant GPU) development. Around 1990, MD simulations still struggled with surpassing the 1 ns mark in meager model systems.[118] Usually, preconstructed micelles were introduced in the simulation boxes that remained stable over the course of the brief simulations.[*id.*] Nevertheless, support from this branch of research was greatly appreciated at the time, not least due to the multiplicity of uncertainties still governing the field.[*id.*] The processing capacity of modern computer systems, even more so in combined arrays, enables monitoring of the evolution of aggregates from molecular solutions without additional bias. This offers the opportunity to not only conveniently create a basis for the comparison to pre-Ouzo aggregates, but to further provide explicit insight into the properties of surfactant micelles on a molecular level.

With respect to the mutual dependencies of the topics, this thesis is structured as follows: Chapter 1 elaborates the computational methods, Chapter 2 is devoted to micelles formed by surfactant molecules above the CMC, and Chapter 3 discusses results from MD simulations of various ratios of the three constituents of the pre-Ouzo model system with and without additives.

Hydrotropes

Similar to surfactants, hydrotropic agents have antagonistic properties and are mainly characterized by enhancing the solubility of hydrophobic compounds in water.[119] An important area of application is clinical drug development, where employment of many conventional surfactants needs to be avoided due to health concerns.[120] The term is often used to denote substances with significantly shorter hydrophobic tail

sections than classical surfactants that do not self-assemble to micelles.[121,122] However, these vague delimitations also comprise electrolytes that promote solubilization via a "salting-in" effect.[123] In 2016, KUNZ et al. suggested a tighter definition based on ideas of ABBOT et al.:[124–127] "a hydrotrope is a substance that show[s] property A and/or B and does not form a microemulsion or lyotropic liquid crystal.", with

A "a hydrotrope is a substance whose structuring in water is enforced by the presence of a third, water-immiscible compound." with regard to an aqueous dispersion medium and

B "a hydrotrope is [...] a substance, whose structuring in the organic solvent is enforced by the presence of water." with regard to an organic solvent.

chapter **one**

Methods

1.1 Molecular dynamics simulations

1.1.1 Software and parameters

All simulations were carried out using the GROMACS suite of programs in version 4.5.x and above[128] in single precision. The simulation boxes were created using the tools provided in the GROMACS package and the PACKMOL configuration generator.[129] In either case, conformations are constructed with no regard for the force field and physical conditions, using a crude estimate of atomic radii to avoid particle overlap. This may result in severely unfavorable conformations once coordinates are interpreted within the chosen framework conditions. Therefore, the simulation procedure was divided into three phases:

1) minimization of the total force in the initial conformations,

2) equilibration of the system volume, and

3) the production run yielding the MD trajectories on which analyses were performed.

The data generated in 1) and 2) were discarded except for the final coordinates that serve as input for the next step. In 1), a steepest descent integrator was used for 1000 iterations for the sole purpose of eliminating excessive forces that would prevent MD sampling of the system with a reasonable time step. The parameters employed in the production runs are listed in Table 1.1 in the GROMACS specific syntax. Values in parentheses designate settings used in case organic hydrogen atoms were represented by virtual interaction sites.[130] In this scheme, hydrogen atoms are not propagated explicitly, instead their

locations are reconstructed from the positions of three nearby heavy atoms in each step for the evaluation of forces. This implicit treatment removes hydrogen angle and bond vibrations and leaves dihedral motions as the highest-frequency degrees of freedom, thus raising the limit imposed on the time step to 5 fs.[id.]

Table 1.1: Prerequisites of the simulations. Settings in parentheses are used in case where hydrogen atoms are represented by virtual interaction sites.

Keyword	Setting	Description
	general	
integrator	md	a leap frog algorithm
dt	0.002 (0.005)	time step (ps)
	constraints	
constraints	all-bonds	rigid bonds
lincs-order	4 (6)	highest order in the expansion of the constraint coupling matrix in (P-)LINCS ((Parallel) LINear Constraint Solver)
lincs-iter	1 (2)	number of iterations to correct for rotational lengthening in (P-)LINCS
	electrostatic interaction	
coulombtype	pme	Smooth Particle Mesh Ewald electrostatics[131]
rcoulomb	*the most efficient value is determined by the software for each simulation individually*	real space cutoff for electrostatic interactions
	van der Waals interaction	
vdw-modifier	Potential-shift-Verlet	potential is shifted to zero between rvdw-switch and rvdw
rvdw	1.0	cutoff for van der Waals interactions (nm)
rvdw-switch	0.9	*see above* (nm)
dispcorr	energy and pressure	long range dispersion correc-

Keyword	Setting	Description
		tion for energy and pressure
	neighbor searching	
nstlist	10 (40)	neighbor list update interval (steps)
	temperature coupling	
ref_t	300	temperature (K)
tcoupl	v-rescale	velocity rescaling thermostat with a stochastic term
nsttcouple	10 (4)	frequency for coupling the temperature (steps)
tau_t	1.0	time constant for temperature coupling (ps)
	pressure coupling	
ref_p	1.0	pressure (bar)
Pcoupl	Parrinello-Rahman	Parrinello-Rahman barostat[132]
nstpcouple	10 (4)	frequency for coupling the pressure (steps)
tau_p	1.0	time constant for temperature coupling (ps)

All simulation boxes are cubic and self-connected by periodic boundary conditions. Unless otherwise stated, the TIP4P/2005 water model[133] was used and organic compounds were described by the OPLS all atom force field.[134] Except for ethanol and propanol, coefficients of the aliphatic torsional potential expansion were interchanged with a parameter set optimized for long hydrocarbons (L-OPLS).[135]

Settings during equilibration only differ from the production run by the choice of a smaller time step of $\Delta t = 1$ fs and pressure coupling by means of a Berendsen barostat.[136] System volume usually converged within less than 20 ps, but relaxation was continued for a total of 150 ps in each case to ensure a plateau in density. The extent of the production simulations depends on the considered systems and is catalogued in the subsequent section.

1.1.2 Simulation setup and execution

1.1.2.1 Ionic micelles

The systems contain a binary ionic surfactant-water solution. The Lennard-Jones parameters for Na^+ and Br^- ions were taken from HORINEK et al.[137] For further reference, structure formulae of the investigated surfactant molecules are depicted in Figure 1.1 alongside their common labels, abbreviations and atom numbering used throughout this work. Since only a single composition is examined for each surfactant class, the abbreviations are used interchangeably to refer to both the whole system and the species itself. The respective reference is apparent from the context.

System compilations and inherent properties are listed in Table 1.2. In addition, the experimentally determined critical micelle concentrations (CMC) are annotated for each surfactant species. These served as guidelines for preliminary trials. Surfactant concentration was then increased stepwise from that level until persistent aggregation in numerous simultaneous micelles was observed.

Table 1.2: Key data on the simulated surfactant mixtures. L designates the box edge length and c_s the surfactant concentration. The last column lists the experimentally determined critical micelle concentrations. The superscript [a] denotes measurements at 298 K, [b] at 283 K, and [c] at unspecified room temperature. Multiple appended superscripts follow the sequence of the cited literature. The # symbol marks simulations in which explicit organic hydrogen atoms were replaced by virtual site constructions.

Species	L	No.		c_s	CMC exp.
		water	surfactant		
	(nm)	(molecules)		(mol l^{-1})	(mol l^{-1})
OTA	7.3	10^4	242	1.0	0.25[a; 138], 0.225[a; 139]
DeTA	10.9	$4 \cdot 10^4$	240	0.31	$\sim$ 0.67[a; 140, 141]
DTA#	13.5	$8 \cdot 10^4$	160	0.11	0.014 – 0.0155[c, a, a, a; 142–145]
CAP#	8.6	$2 \cdot 10^4$	200	0.5	0.38 – 0.39[b, c; 146, 147]
DECA#	10.8	$4 \cdot 10^4$	180	0.24	0.05[c; 148], 0.086[a; 149]

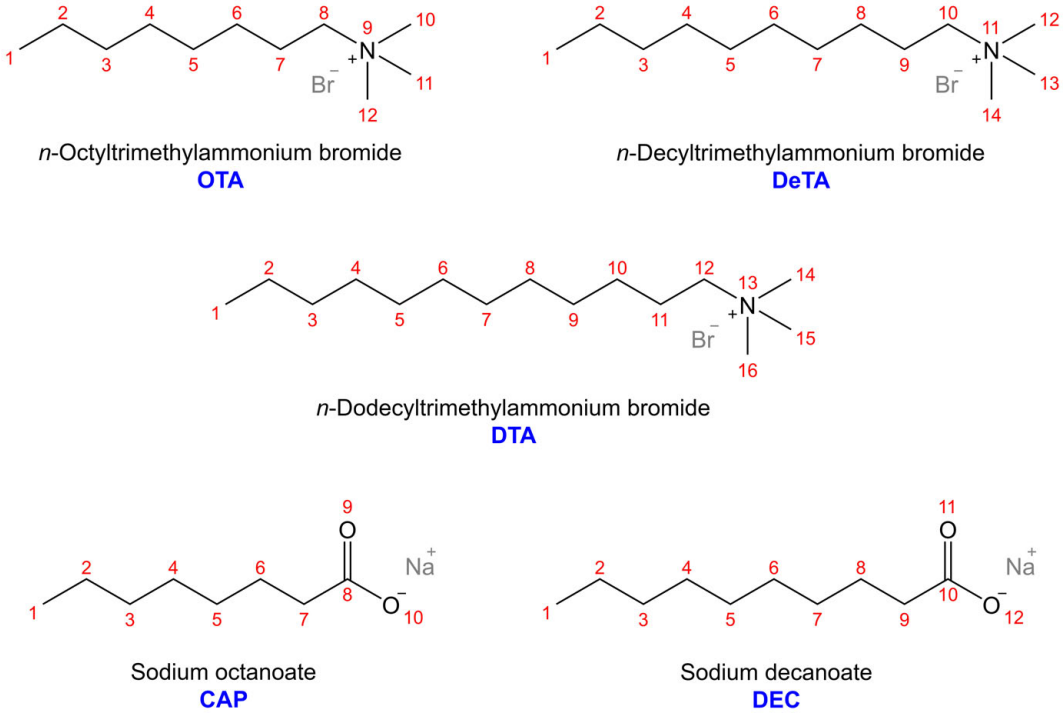

Figure 1.1: Structure formulae of the simulated surfactant salts with the utilized enumeration of heavy atoms and chosen highlighted abbreviations in **blue**.

The time span of simulations was chosen on a per-case basis, aiming for at least 500 ns of converged trajectory data. The procedure of convergence assessment (which will be covered in detail in Section 2.2) involved two production runs for each system, one starting from random distribution of the components and the other from a single agglomerate of surfactant molecules in water. The total sampling time for each simulation is given in Table 1.3.

Table 1.3: Time spans of simulations of surfactant systems. Path H starts from molecular solution and path S from a phase separated state.

Path	Species				
	OTA	DeTA	DTA	CAP	DEC
H (μs)	0.745	1.00	7.47	3.57	11.1
S (μs)	0.571	1.00	6.43	3.57	15.8

1.1.2.2 Ouzo systems

The system properties of the sampled water/ethanol/octanol mixtures are listed in Table 1.4. Ethanol and octanol hydrogen atoms were always modeled by virtual interaction sites.

Table 1.4: Key data on the simulated water/ethanol/octanol systems. The quantity *L* designates the box edge length. The abbreviations wat., eth., and oct. stand for water, ethanol, and octanol, respectively.

Label	*L*	No.			mole ratios	mass ratios
		water	ethanol	octanol		
	(nm)	(molecules)			[wat. : eth. : oct.]	
I	10.6	28632	3179	224	0.89 : 0.10 : 0.01	0.75 : 0.21 : 0.04
α (II)	11.7	25380	6366	224	0.79 : 0.20 : 0.01	0.58 : 0.38 : 0.04
III	11.2	22176	9600	224	0.69 : 0.30 : 0.01	0.46 : 0.51 : 0.03
β	11.0	8303	5608	2088	0.52 : 0.35 : 0.13	0.22 : 0.38 : 0.40
γ	10.9	5400	3600	3000	0.45 : 0.30 : 0.25	0.15 : 0.25 : 0.60

The approximately 1 mol l^{-1} pre-Ouzo salt solutions were generated by addition of 836 ion pairs to composition α. The Lennard-Jones parameters for Li^+, Na^+, Cl^-, and I^- were taken from Dang.[150–152] Since these parameters are designed for Lorentz-Berthelot combination rules, those are evaluated for ion-ion interactions, whereas the OPLS/AA inherent geometric mean is used for ion – water/ethanol/octanol interactions.

For the same reason as stated in the previous section, two separate simulations were conducted for compositions I – III, one starting from molecular solution and the other from a single droplet of octanol in a homogeneous mixture of water and ethanol. Given the time scale of convergence discussed in Section 3.2.1, this procedure was neither repeated for β and γ, nor for the ouzo systems containing additives. The total simulation times of all water/ethanol/octanol systems are given in Table 1.5.

Table 1.5: Time spans of simulations of ouzo systems. Path H starts from molecular solution and path S from a droplet of octanol in a homogeneous mixture of water and ethanol.

Path	System							
	I	α (II)	III	β	γ	α + NaI/LiCl	α + propane	α + squalene
H (μs)	0.70	3.8	0.40	0.20	0.20	1.8	1.9	1.0
S (μs)	0.68	2.5	0.30	-	-	-	-	-

1.1.2.3 Miscellaneous

Water / propan-1-ol (propanol) / octanol The simulation box was filled with 28549 water molecules, 3197 propanol molecules, and 224 octanol molecules at random positions. This configuration corresponds to molar ratios of 0.89 : 0.10 : 0.01 or mass ratios of 0.70 : 0.26 : 0.04 (water : propanol : octanol) and resulted in an equilibrated box edge length of $L = 10.9\,\text{nm}$. Hydrogen atoms were propagated explicitly. The total simulation time of this system amounts to 1 μs.

Water / 2-methyl-propan-2-ol (*t*-butanol) A molecular solution of 120 *t*-butanol molecules and 2880 water molecules was generated. This ratio denotes a molar fraction of 4.0 % or weight fraction of 15 % of the alcohol. A force field specially designed for atomistic simulations of aqueous tertiary butanol solutions by LEE and VAN DER VEGT[153] was employed for the organic compound in conjunction with the SPC/E water model.[154] Box edge lengths relaxed to 4.7 nm and the system was simulated for 200 ns.

Water/octanol slab system Two separate boxes of square cuboid shape were generated. One was filled with 6469 water molecules and the other with 1351 octanol molecules. The two boxes were joined at the smallest faces, assuring a minimum distance between adjacent octanol and water atoms of 1 nm. The resulting gap quickly vanished during equilibration with semi-isotropic coupling to a Berendsen barostat during a 150 ps simulation. In this scheme, only the shortest box vectors are scaled, while the longest axes, which are parallel to the macroscopic symmetry axis of the system, are held constant. This way, the longitudinal extents of octanol and water phases are maintained. The average box dimensions during the production run were 6.4 nm × 6.4 nm × 13.7 nm. The system was simulated for 260 ns with explicit hydrogen treatment.

Frozen octanol and octane micelle The position restraints of octanol and octane molecules were realized by applying harmonic potentials of the form

$$V(r_i) = \frac{1}{2} k \, |r_i - R_i|^2 \tag{1.1}$$

to each octanol or octane atom, where r_i is the position of particle i, R_i its reference position, and k a force constant. The reference positions are merely the initial position vectors resulting from arbitrary positioning of an aggregate in the simulation box. The configuration of the octanol aggregate was chosen by sorting all aggregates containing 22 ± 3 molecules in the composition α plus salt trajectories by means of their radii of gyration and identifying the structure closest to the average. This procedure yielded an

octanol micelle containing 20 molecules. The octane aggregate was specifically generated to be of similar dimensions and shape.

The simulation boxes were subsequently randomly filled with

a) 142 ion pairs, 954 ethanol, and 3816 water molecules or

b) 129 ion pairs, and 7155 water molecules.

In both cases, electrolyte concentration is close to 1 mol l^{-1} with equilibrated box edge lengths of 6.0 nm and 6.1 nm, respectively. Octanol and octane hydrogen atoms were represented by virtual interaction sites and the total simulation time was 1 μs in each case.

1.2 Analysis

The major part of analyses relies on the identification and isolation of individual aggregates. This functionality is adopted from the GROMACS tool `g_clustsize` provided in version 4.5.4. The method scans for the overlap of spheres with specified radius centered on every atom of a selected set with any other sphere in the same set that belongs to a different molecule. In case of success, molecules are allocated to the same cluster. For all compounds, the reference group consisted of the heavy atoms and the hydroxyl group if present. An exception to this rule applies to *t*-butanol, where only the quaternary carbon was selected.

The geometric classification used by the algorithm requires an adequate cutoff reflecting characteristic distances between the solute molecules. Meaningful values for this parameter are obtained as the first distinct minima in the radial distribution functions (RDFs) of the respective group in systems with sufficient solute-solute contacts in a similar environment. For octanol, this value has been determined to 0.478 nm by means of a simulation of a single stable octanol droplet in water in a previous work.[116] It has further been demonstrated in this context that the results are robust towards changes of the cutoff within reasonable limits. A shift to 0.78 nm (the subsequent minimum in the octanol RDF), for instance, naturally led to detection of larger aggregates but had no qualitative impact on the outcome. The cutoff radii for the remaining solutes were established by means of simulations of significantly more saturated mixtures than represented by the analyzed systems or phase separated compositions. Details on the process are found in the supplementary section 1.A. The determined values are listed in Table 1.6.

Table 1.6: Distance cutoff values r_{cc} set in the clustering algorithm for the investigated solutes.

Path	Compound						
	OTA	DeTA	DTA	CAP	DEC	*t*-butanol	squalene
r_{cc} (nm)	0.476	0.478	0.480	0.486	0.487	0.799	0.464

A range of programs was developed to compute the data presented in this work, using the data arrays returned by the central `g_clustsize` function where required. The cumulative source code is too extensive to be displayed here and in most cases strategies are straightforward from an informatics perspective. Basic descriptions of the most important procedures, if not part of the discussion or self-evident, as well as snippets of more complex routines are given in the following paragraphs. Peculiarities of the respective results are outlined during the discussion.

Cluster size histogram

First appearance: Section 2.2

The absolute frequency of aggregation numbers is a direct output of the `g_clustsize` tool.

Eccentricity of aggregates

First appearance: Section 2.3

Aggregates are identified by means of the `g_clustsize` routine. The principal moments of inertia of the assortment of atoms constituting the aggregate are calculated by diagonalizing the inertia tensor using the `jacobi(...)` routine from Ref. 155.

Smallest bounding sphere of aggregates

First appearance: Section 2.3

Aggregates are identified by means of the `g_clustsize` routine. The smallest bounding sphere encompassing all atoms constituting the aggregate is determined by means of GAERTNER's algorithm.[156]

Convex hull of aggregates

First appearance: Section 2.3

The SciPy 1.0 toolbox for python[157] includes a dedicated method for the computation of the convex hull of *n*-dimensional point clouds. The primary output includes simplical facets, hull area, and hull volume.

For the determination of the convex hull of micellar structures, the aggregates are first identified by means of the `g_clustsize` routine. Subsequently, the convex hull of the 3D point cloud represented by all atoms constituting the aggregate is computed.

Distribution of specific atom groups around the center of geometry of aggregates

First appearance: Section 2.4

Aggregates are identified by means of the `g_clustsize` routine. The center of geometry (COG) of all atoms of the subset is computed and the number of atoms of the selected components in progressively larger concentrical spherical shells around this coordinate is evaluated. The count in each shell is normalized to the shell volume. After the trajectory has been processed, the individual particle densities are normalized to their respective bulk values. No bulk is present for the aggregating species, therefore the curve is normalized to the peak value that naturally occurs close to the COG.

Radius of the hydrophobic core

First appearance: Section 2.4

Aggregates are identified by means of the `g_clustsize` routine. The largest spherical volume inside this aggregate that does not overlap with any atom belonging to a water molecule is iteratively determined.

Relative hydration

First appearance: Section 2.4

Pair distribution functions between each surfactant chain unit and water are calculated in a system containing a single surfactant molecule in water using the GROMACS tool `g_rdf`. The absolute number of water molecules up to the first distinct minimum in the respective distribution is counted. The same procedure is repeated for the micellar solutions and the count of water molecules in the first solvation shell of each group is normalized to the value obtained for the system containing a single surfactant molecule.

In a separate analysis, only the surfactant molecules inside a specific aggregate identified by means of the `g_clustsize` routine are considered. The respective pair distribution functions are then computed for this subset by a self-written algorithm.

Probability of *trans* dihedral alignment

First appearance: Section 2.4

Dihedral angles are computed by the GROMACS tool `g_angle`. The position *trans* is defined by $120^\circ < \phi < 240^\circ$, where ϕ is the angle between the (i,j,k)- and the (j,k,l)-plane of a consecutively bonded (i,j,k,l)-quadruplet of atoms. Analysis encompasses the aliphatic tail sections excluding the carbon atom connected to the functional group.

In case of aggregate-specific analysis, clusters are identified by means of the `g_clustsize` routine and the relevant atom indices are passed to `g_angle`.

Solvent accessible surface area

First appearance: Section 2.4

Aggregates are identified by means of the `g_clustsize` routine. The subset is passed to the GROMACS tool `g_sas`, which directly calculates the desired quantity.

Proximal distribution of specific atom groups with regard to the surface of aggregates

First appearance: Section 2.4

Aggregates are identified by means of the `g_clustsize` routine. The contact distance between two atom species is set to the point where the mutual Lennard-Jones potential, derived using the according force field parameters and combination rules, is equal to $k_\mathrm{B}T$, with the Boltzmann constant k_B and simulation temperature T. An atom coming this close to an atom of the reference group is considered to be “on the surface”. For each particle, the shortest distance from this implicitly defined surface is evaluated. The number of atoms belonging to a chemical species found within a certain interval is normalized to the total number of atoms matching any of the selected groups that are detected within this distance range (if the count is not zero). The resulting quantity for each segment is the conditional probability $\mathrm{P}_A(B_i)$, where event A designates the detection of any particle of the analyzed groups within this region and event B_i the detection of an atom of category i.

This approach offers the advantage of giving a clear representation of the system composition at each point, even in regions where particle density is naturally low. For

great distances, equal count of atoms per molecule, and homogeneous distribution of the selected components, it reflects the bulk ratio of the species.

Water-water hydrogen bonds

First appearance: Section 2.4

All hydrogen bond analyses use the common combination of a 0.35 nm donor-acceptor distance and 30° hydrogen-donor-acceptor angle cutoff. In case examinations relate to individual aggregation numbers, clusters are preliminarily identified by means of the `g_clustsize` routine. Proximal distributions are computed according to the scheme described in the previous paragraph.

Fraction of black balls remaining in an urn, from which a random ball is drawn and that is refilled with a white ball; evaluated after *N* repetitions for an originally fully black urn

First appearance: Section 2.5

Listing 1 contains the relevant section of code used to compute $s_B(N)/S$. This procedure is based on a probabilistic model of monomer exchange events in micelles that is described in Section 2.5. In combination with a second analysis, which monitors the decay behavior of labeled monomers in the micelles, the dissociation rate constant can be calculated.

Listing 1: Outline of the **C** code used to compute the fraction of black balls remaining in an urn originally filled with black balls exclusively, that is refilled with a white ball upon each draw; evaluated after *N* repetitions.

```
1
2 /* The function pmass(...) calculates the probability mass
     function for set size 'S' and a vector 'vector' of dimension '
     size'. */
3 double pmass(int *vector, int S, int size)
4 {
5   int i,subsum;
6
7   subsum = 0;
8
9   if (size == 1)
10  {
11    return 1.0;
12  }
13
14  if (size > 1)
15  {
16    if (vector[size-1] == 1)
```

```
17      {
18        for (i = 0; i < size-1; ++i)
19        {
20          subsum += vector[i];
21        }
22        return ((S - subsum) / (double)S * pmass(vector,S,size-1));
23      }
24
25      if (vector[size-1] == 0)
26      {
27        for (i = 0; i < size-1; ++i)
28        {
29          subsum += vector[i];
30        }
31
32        return (subsum / (double)S * pmass(vector,S,size-1));
33      }
34    }
35  }
36
37  /* The function permute(...) calculates all non-equivalent
       permutations of a binary vector 'vector' of dimension 'size'
       for a given number of "1"-entries. For each permutation, the
       expected value 'sum' is incremented by the product of the
       return value of the pmass(...) routine and the random variable
        X_n 'xn'. */
38  void permute(int *vector, int curpos, int nrones, int size, int S
      , double *sum)
39  {
40    int i,j,xn;
41    int *subvec;
42
43    if (nrones == 0)
44    {
45      xn = 0;
46
47      for (i = 0; i < size; ++i)
48      {
49        xn += vector[i];
50      }
51
52      *sum += pmass(vector,S,size) * xn;
53    }
54    if (nrones > 0)
55    {
56      for (i = curpos; i < size; ++i)
57      {
58        /* Memory allocation routine by framework */
59        snew(subvec,size);
60
61        for (j = 0; j < size; ++j)
```

```
62        {
63          subvec[j] = vector[j];
64        }
65        subvec[i]=1;
66        permute(subvec,i+1,nrones-1,size,S,sum);
67
68        /* Memory deallocation routine by framework */
69        sfree(subvec);
70      }
71    }
72  }
73
74  int main(/* Input controlled by framework: (1) output file name,
        (2) number of black balls at start S, (3) total number of
        draws N */)
75  {
76    int i,j,size;
77    int *vector;
78    double sum;
79
80    /* Data type FILE defined by framework */
81    FILE *out;
82
83    /* File I/O managed by framework */
84    out = fopen(opt2fn("-o",NFILE,fnm),"w");
85
86    /* Print initial condition: 0 draws means 100 % of the black
         balls are remaining */
87    fprintf(out, "0 1.0\n");
88
89    for (int i = 1; i <= N; ++i)
90    {
91      sum=0;
92      size = i;
93      snew(vector,size);
94
95      for (j = 0; j < size; ++j)
96      {
97        vector[j]=0;
98      }
99
100     vector[0]=1;
101
102     for (j = 0; j < i; ++j)
103     {
104       permute(vector,1,j,size,S,&sum);
105     }
106
107     /* Print the fraction of black balls still in the ensemble
          after each draw*/
108     fprintf(out, "%d %f\n",i, ((double)S-sum)/(double)S);
```

```
109     }
110
111     return 0;
112 }
```

Reconstruction of a non-continuous object with dimension exceeding that of half the simulation box

First appearance: Section 3.2.5

Aggregates are identified by means of the `g_clustsize` routine. In the scheme of periodic continuity, penetration of the simulation box boundary results in fragmentation of the object with regard to a single image of the system. In a first step, all fragments of the structure are identified by means of the subroutine in Listing 2.

Listing 2: A function in **C** that seeks a non-periodic connection between two particles “anfang” and “ende” by means of a catenation of atoms in the same aggregate that are closer to each other than the specified cutoff distance and returns the boolean value **TRUE** if such a path exists.

```
1  /* Data types:
2    gmx_bool is a boolean definition from the GROMACS framework
3    real is either float or double, depending on whether GROMACS
       was compiled in single or double precision
4    rvec is a three dimensional vector construction of data type
       real
5    atom_id is an array of data type int */
6
7  /* Arguments:
8    cut2 = square of the cutoff distance
9    nindex[x] = count of particles in set x; set 1 contains the
       subset of atoms in the aggregating group
10   clust_index[i] = enumerator of the aggregate that contains
       particle i
11   thisclustindex = enumerator of the aggregate under
       consideration
12   x[i] = position vector of particle i
13   index[x][i] = enumerator of particle i in set x
14   anfang / ende = atoms that were determined to be connected
       through the periodic boundary
15   processed[i] = a path involving this particle has been tried
16   bErase = erase all paths (only true for the external call) */
17 gmx_bool connected(real cut2,int *nindex, int *clust_index,
18             int thisclustindex, rvec *x, atom_id **index,
19             int anfang, int ende, gmx_bool *processed,
20             gmx_bool bErase)
21 {
22   rvec    posanfang, posi, nopbcdx;
```

```
23    int      i,j;
24    real     nopbcdx2;
25
26    if (bErase)
27    {
28      for (i = 0; i < nindex[1]; ++i)
29      {
30        processed[i]=FALSE;
31      }
32    }
33
34    /* Function from framework that creates a duplicate of the rvec
          in the first argument in the second argument */
35    copy_rvec(x[index[1][anfang]],posanfang);
36
37    for (i = 0; i < nindex[1]; ++i)
38    {
39      if (clust_index[i] == thisclustindex)
40      {
41        copy_rvec(x[index[1][i]],posi);
42
43        /* Function from framework that stores the difference
             between the vectors in argument two and one in the
             variable in argument three */
44        rvec_sub(posanfang,posi,nopbcdx);
45
46        /* Function from framework that returns the inner product
             of two supplied vectors */
47        nopbcdx2 = iprod(nopbcdx,nopbcdx);
48        if (nopbcdx2 < cut2)
49        {
50          if (i==ende)
51          {
52            return TRUE;
53          }
54          if (!processed[i])
55          {
56            processed[i]=TRUE;
57            if (connected(cut2, nindex, clust_index, thisclustindex
                  , x, index, i, ende, processed, FALSE))
58            {
59              return TRUE;
60            }
61          }
62        }
63      }
64    }
65    return FALSE;
66  }
```

The `connected(...)` method is successively called for all atom pairs. Upon each execution it searches for a path from one particle to the other, with each step comprising two particles from the same aggregate that are within the mutual cutoff range. If such a path exists, the two sites are allocated to the same fragment*. Subsequently, the fragments are reassembled to a self-contained structure via the `shift(...)` procedure shown in Listing 3.

Listing 3: A function in **C** that computes the vector increment necessary in order to resolve the periodicity of a structure: translation of an atom "particle" by this vector results in its correct non-periodic location with regard to a reference atom.

```
1  /* Data types:
2    gmx_bool is a boolean definition from the GROMACS framework
3    real is either float or double, depending on whether GROMACS
       was compiled in single or double precision
4    rvec is a three dimensional vector construction of data type
       real
5    atom_id is an array of data type int */
6
7  /* Arguments:
8    cut = the cutoff distance
9    nindex[x] = count of particles in set x; set 1 contains the
       subset of atoms in the aggregating group
10   x[i] = position vector of particle i
11   index[x][i] = enumerator of particle i in set x
12   ref = reference atom for coordinate reconstruction
13   particle = atom position to be shifted
14   pbc = GROMACS structure containing information about the
       periodic boundary conditions
15   x_size = box edge length
16   pbc_index[i] = enumerator of the fragment containing particle i
17   fragprocessed[j] = coordinates of fragment j have already been
       processed
18   bErase = reset the process log (only true for external call)
19   corrvec = correction vector that needs to be added to the
       actual position vector of particle "particle" */
20 gmx_bool shift(real cut,int *nindex, rvec *x, atom_id **index,
21           int ref, int particle, t_pbc pbc, real x_size,
22             int *pbc_index, gmx_bool *fragprocessed,
23             gmx_bool bErase, rvec corrvec)
24 {
25   gmx_bool  connection;
26   rvec      posi,posj,dx,convec,nopbcdx;
27   int      i,j;
28   real     dx2,nopbcdx2,cut2;
29
```

*It should be noted that this routine was originally developed for the identification of the infinite aggregate, where the actual path is of no concern. Performance would benefit from an optimized implementation that further returns the indices of all atoms that constitute a successful path.

```
30  cut2=cut*cut;
31
32  if (bErase)
33  {
34    clear_rvec(corrvec);
35    for (i = 0; i < nindex[0]; ++i)
36    {
37      fragprocessed[i]=FALSE;
38    }
39  }
40
41  fragprocessed[pbc_index[particle]]=TRUE;
42
43  connection=FALSE;
44  for (i = 0; i < nindex[0]; ++i)
45  {
46    if (pbc_index[i]==pbc_index[particle])
47    {
48
49      /* Function from framework that creates a duplicate of the
           rvec in the first argument in the second argument */
50      copy_rvec(x[index[0][i]],posi);
51
52      for (j = 0; j < nindex[0]; ++j)
53      {
54
55        /* The pbc_index[...] entry for particles not part of the
             aggregate is -1.*/
56        if(!fragprocessed[pbc_index[j]] && pbc_index[j]!=-1)
57        {
58          copy_rvec(x[index[0][j]],posj);
59
60          /* Function from framework that stores the difference
               between the vectors in argument two and one in the
               variable in argument three */
61          rvec_sub(posi,posj,nopbcdx);
62
63          /* Function from framework that stores the periodic
               difference between the vectors in argument two and
               one in the variable in argument three */
64          pbc_dx(&pbc,posi,posj,dx);
65
66          /* Function from framework that returns the inner
               product of two supplied vectors */
67          dx2 = iprod(dx,dx);
68
69          nopbcdx2 = iprod(nopbcdx,nopbcdx);
70          if (nopbcdx2 > (x_size-cut)*(x_size-cut) && dx2 < cut2)
71          {
72            if (pbc_index[j]==pbc_index[ref])
73            {
```

```
74                rvec_sub(posi,posj,convec);
75                connection=TRUE;
76                break;
77              }
78              else
79              {
80                if (shift(cut, nindex, x, index, ref, j, pbc,
                     x_size, pbc_index, fragprocessed, FALSE, corrvec
                     ))
81                {
82                  connection=TRUE;
83                  rvec_sub(posi,posj,convec);
84                  break;
85                }
86              }
87            }
88          }
89        }
90
91      }
92      if (connection)
93      {
94        break;
95      }
96    }
97
98    if (connection)
99    {
100     for (i = 0; i < 3; ++i)
101     {
102       if (fabs(convec[i]) > x_size/2)
103       {
104         if (convec[i] < 0)
105         {
106           corrvec[i]+=x_size;
107         }
108         else
109         {
110           corrvec[i]-=x_size;
111         }
112       }
113     }
114     return TRUE;
115   }
116   else
117     return FALSE;
118 }
```

Allocation of octanol clusters to squalene molecules

First appearance: Section 3.2.6.1

Aggregates are identified by means of the `g_clustsize` routine. A second distance cutoff is applied to identify contacts between any atom that is part of the detected aggregates and any atom belonging to a squalene molecule. This value was set to 0.66 nm, which corresponds to the position of the first distinct minimum in the radial distribution function of octanol and squalene atoms obtained for a binary octanol/squalene system (cf. supplementary section 1.A).

Solvation free energy

First appearance: Section 3.2.6.2

Aggregates are identified by means of the `g_clustsize` routine. The trajectory is reduced to data frames in which an aggregate of specified size is present. Simultaneously, a list of the respective timestamps and coordinates of the geometric centers of the clusters is maintained. The two data streams serve as input for a version of the ERmod 0.3.5 program[158] specifically modified by the developers for this application.

This software calculates the approximate free energy of solvation based on the energy representation method.[159–161]

The infinite aggregate

First appearance: Section 3.3

Aggregates are identified by means of the `g_clustsize` routine. Next, an algorithm probes each aggregate for two atoms that are connected through the periodic boundary by means of the chosen cutoff distance. These particles need to be separated by at most the cutoff distance in the periodic scheme and by a minimum of [*edge length*]−[*cutoff*] within one image of the box, which is evident from simple geometric considerations. The subroutine `connected(...)` (cf. Listing 2) is then called to search for a path within one image of the box from one of these atoms to the other along particles from the same aggregate that are within mutual cutoff range. If such a path exists, the object is continuous and represents an infinite aggregate.

Small and wide angle X-ray scattering (SWAXS)

First appearance: Section 3.4

Scattering spectra were calculated from the MD trajectories using the dedicated software nMOLDYN 3.[162] The built-in database of coherent and incoherent scattering lengths allows for direct derivation of small and wide angle neutron scattering (SWANS) data. Conversely, no weights reflecting the local charge distribution around the nuclei, which are needed to compute the X-ray contrast, are implemented. For this reason, the following multilevel procedure was pursued to obtain the SWAXS intensities:

1) computation of the partial coherent static structure factors $s_i(q)$ with nMOLDYN,

2) calculation of partial (theoretical) intensities according to the relation

$$\tilde{i}_i(q) = \sqrt{N_a N_b} \cdot s_i(q) \cdot f_a(q) f_b(q), \tag{1.2}$$

where N_j is the count and $f_j(q)$ the atomic form factor of species j.[163,164] The latter are approximated by a sum of Gaussians of the form

$$f_j(q) = \sum_{n=1}^{4} a_{j,n} \mathrm{e}^{\left(-b_{j,n}\left(\frac{q}{4\pi}\right)^2\right)+c}, \tag{1.3}$$

with tabulated values $a_{j,n}$, $b_{j,n}$, and c.[165]

3) The total intensity is given by the sum over the partial intensities,

$$\tilde{I}(q) = \frac{1}{\sum_i N_i} \sum_i i_i(q). \tag{1.4}$$

The first factor in Equation (1.2) reverses the normalization introduced by nMOLDYN during the calculation of the partial structure factors,[166] so that the partial intensities in Equation (1.4) obey the same scale. The real intensity $I(q)$ depends on several factors not taken into account by this approach, including specific properties of the measurement apparatus and the transmittivity of the probe.[167] Therefore, calculated intensities are declared as arbitrary units that serve only for quantitative matching of structural properties to the experiment, which renders further normalization unnecessary.

1.3 Data visualization

Data resolution Prevalently, diagrams of analysis outcomes are displayed in continuous line representation. To give a clear account of the actual resolution, each data point is accentuated by a circle of the same color as the respective graph if the width of intervals is not simply evident. Markers may be omitted for individual graphs in a compilation of equally spaced data sets for optical reasons.

Box plots On occasion, diagrams containing histograms are complemented by box plot representations of the data to provide insight into statistical characteristics. Since the construction of this type of illustration is not unambiguously defined, a sample of the practice and visualization rules used in this work is depicted in Figure 1.2.

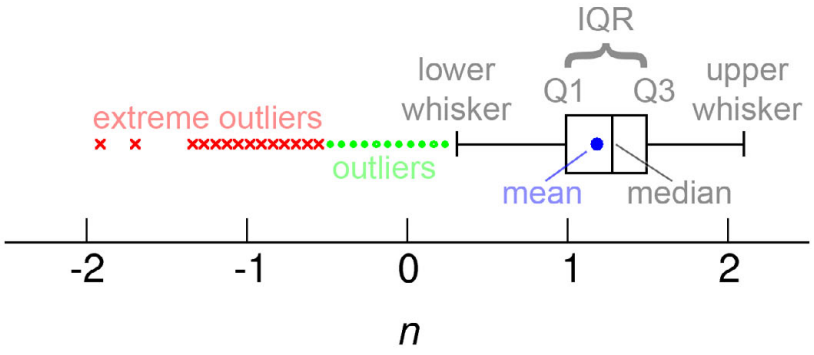

Figure 1.2: Example of a box plot for an arbitrary quantity n with descriptions in a lighter shade of the respective color.

The box meets the generally recognized standard of being subdivided at the location of the median and encompassing the interquartile range (IQR), which is defined as the difference between the 75th and 25th percentile, IQR = Q3 − Q1, and therefore contains the central 50 % of the distribution.[168,169] The datums of these items were estimated to lie between the histogram bin where the required value (e.g. 50 % of the data for the median) is exceeded for the first time and the preceding bin, if no exact match was found. The positions of the upper and lower whiskers and classification of outliers was chosen according to TUKEY's suggestion:[170] whiskers are positioned at the outermost data points that fall within 1.5-fold interquartile range measured from the median. Contributions between 1.5-fold and 3-fold interquartile range are labeled as outliers and those outside 3-fold interquartile range as extreme outliers. At all times, the (arithmetic) mean, too, is provided in the fashion depicted in the sample.

1.A Radial distribution functions

Distance cutoff for cluster determination Figure 1.3 shows the radial distribution functions that were consulted for the determination of the substance specific cutoff value to be used by the cluster search algorithm (cf. Section 1.2).

The water/octanol system was randomly filled with 56 octanol and 7944 water molecules. The box edge length equilibrated to 6.3 nm and hydrogen atoms were propagated explicitly in this simulation. The system was sampled for a total of 200 ns.

The water/squalene system was randomly filled with four squalene and 57113 water molecules. The box edge length converged to 12.0 nm during equilibration and hydrogen atoms were propagated explicitly in this simulation. The system was sampled for a total of 120 ns.

The water/*t*-butanol system was randomly filled with 300 *t*-butanol and 2700 water molecules. The box edge length equilibrated to 5.0 nm. The dedicated force field by LEE and VAN DER VEGT[153] was employed for the organic compound in conjunction with the SPC/E water model.[154] The system was sampled for a total of 20 ns.

The properties of systems involving surfactant molecules are listed in Table 1.7. The initial conformations were randomly generated.

Contact between octanol clusters and squalene molecules Figure 1.4 shows the radial distribution function of octanol and squalene molecules in a system containing one squalene molecule and 145 octanol molecules. The system was sampled for a total of 500 ns. The average box edge length amounted to 3.4 nm and hydrogen atoms were propagated explicitly in this simulation.

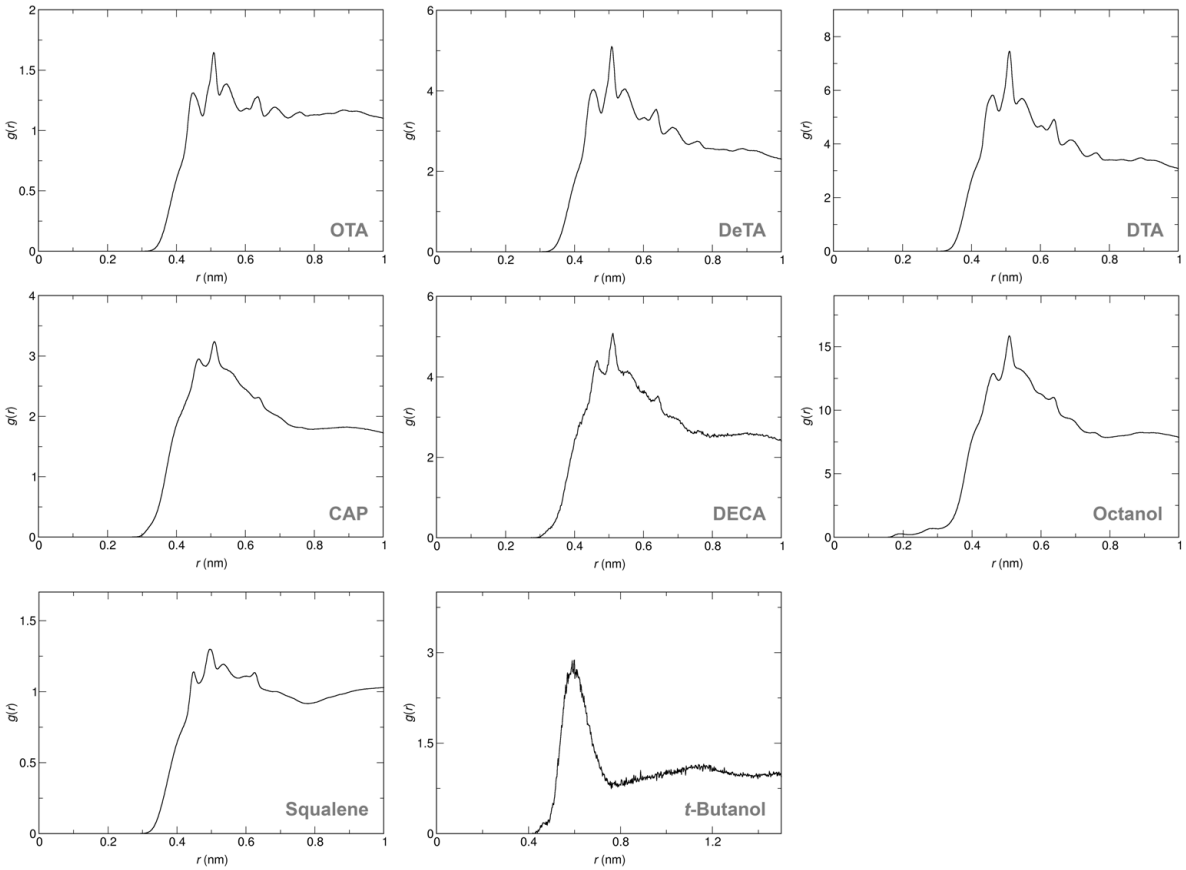

Figure 1.3: Radial distribution functions $g(r)$ of surfactant heavy atoms in concentrated water / OTA, DeTA, DTA, CAP, and DEC mixtures, octanol heavy atoms plus hydroxyl hydrogen in a phase separated water/octanol mixture, squalene heavy atoms in a phase separated squalene/water mixture, and *t*-butanol quaternary carbon atoms in a phase separated water/*t*-butanol mixture. The respective systems are marked in the diagram.

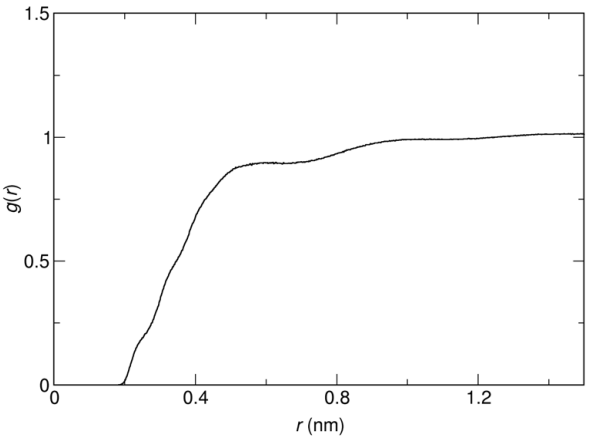

Figure 1.4: Radial distribution function of octanol and squalene atoms in a binary mixture of octanol and squalene.

Table 1.7: Properties of the binary water/surfactant systems processed to obtain characteristic radial distribution functions of the respective heavy atoms. *L* designates the box edge length and the # symbol marks simulations in which explicit organic hydrogen atoms were replaced by virtual site constructions.

Species	***L***	**No.**		**Total Simulation time**
		water	**surfactant**	
	(nm)	(molecules)		(ns)
OTA	7.3	10^4	720	70
DeTA	7.1	$1 \cdot 10^4$	120	180
DTA#	8.8	$2 \cdot 10^4$	160	100
CAP#	5.8	$5 \cdot 10^3$	200	100
DECA#	7.1	$1 \cdot 10^4$	200	100

chapter **two**

Ionic micelles

2.1 Overview

This chapter deals with micelles formed by ionic surfactant molecules above the CMC. To this end, aqueous solutions of the bromide salts of octyltrimethylamine ("OTA"), decyltrimethylamine ("DeTA"), and dodecyltrimethylamine ("DTA"), as well as the sodium salts of octanoic acid ("CAP"), and decanoic acid ("DEC") are examined. Thereby, spontaneous formation of aggregates distributed around a preferred aggregation number is sampled in MD simulations.

The often lengthy process of system convergence contributing to the high demands on computer hardware is described in Section 2.2. Further, the preferred number of aggregation is determined and the degree of polydispersity is evaluated.

Structural considerations are divided between Sections 2.3 and 2.4. In the first, the micelle geometry is delimitated and the degree of shape fluctuations is estimated. Against this background, Section 2.4 then focuses on the characteristic assembly and controversial subject of water penetration.

In conclusion, Section 2.5 imparts an insight into the dynamic properties of the aggregates. Typical fluctuation behavior is briefly outlined and the rate constants of monomeric exchange are evaluated based on a statistical analogy.

2.2 System relaxation

The suitability of atomistic MD simulations highly depends on the time scale of processes in a particular system. While computer hardware limits system size but not achievable simulation time, practicability does. For the systems at hand (cf. Section 1.1.2.1), a performance of 47 to 156 ns per day was attainable on state-of-the-art hardware with reasonable parallel scaling. In the scope of this work, this efficiency range confines the accessible realm of total simulation time to several microseconds.

The expected process in these binary systems is the assembly of the ionic surfactant molecules to micellar objects. This equilibration is quantitatively monitored for all investigated amphiphiles based on the temporal evolution of cluster size distributions in Figure 2.1.

To ensure that the structures represent a global minimum in free energy, two pathways are evaluated in each case: a system starting from random distribution of the components and another starting from a phase separated state. As the curves show, the time spans of convergence differ widely. In case of the smallest cationic surfactant, equal distributions attune within less than 100 ns, whereas a DECA droplet does not break down into the small aggregates emerging from homogeneous dispersion until the simulation is terminated after more than 15 μs sampling time. Assimilation of the DTA systems progresses significantly faster, but is evidently still in the course of leveling out towards the end of the trajectories. The decanoate micelles will be included in the analysis, but since no tendency in either system is evident, the results have to be regarded as prototypal. In all incidents, the mixing process is the more tedious to converge and results in comparatively short converged passages. For this reason, analyses are performed on the converged segments of the simulations starting from random distribution.

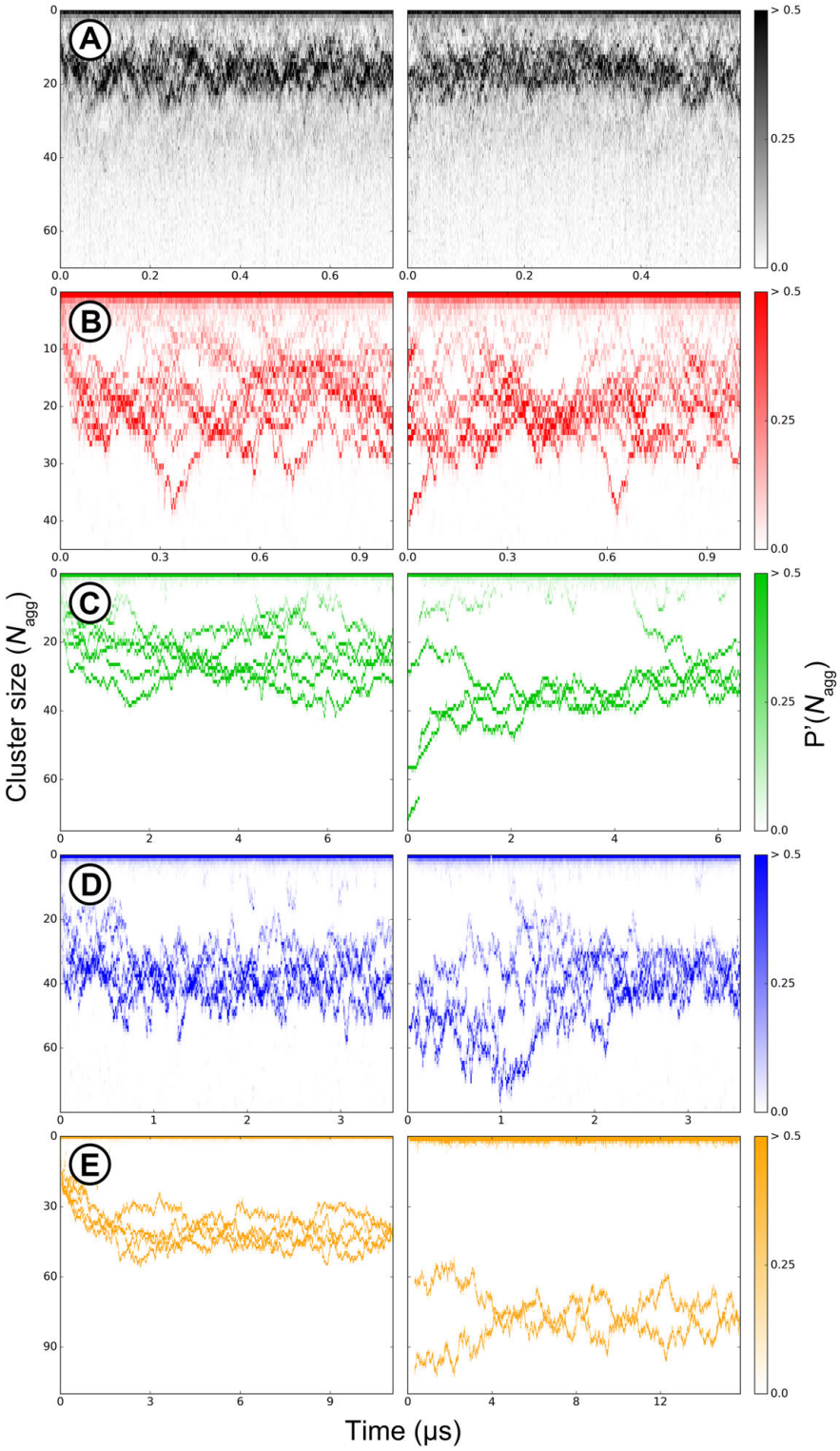

Figure 2.1: Cluster size evolution of **A** OTA, **B** DeTA, **C** DTA, **D** CAP, and **E** DEC micelles in systems starting from homogeneous solution (left column) or a phase separated state (right column) in colormap representation. The color grading denotes the probability for a surfactant molecule to be part of an aggregate of size N_{agg} $P'(N_{agg})$, with respect to the provided color bars.

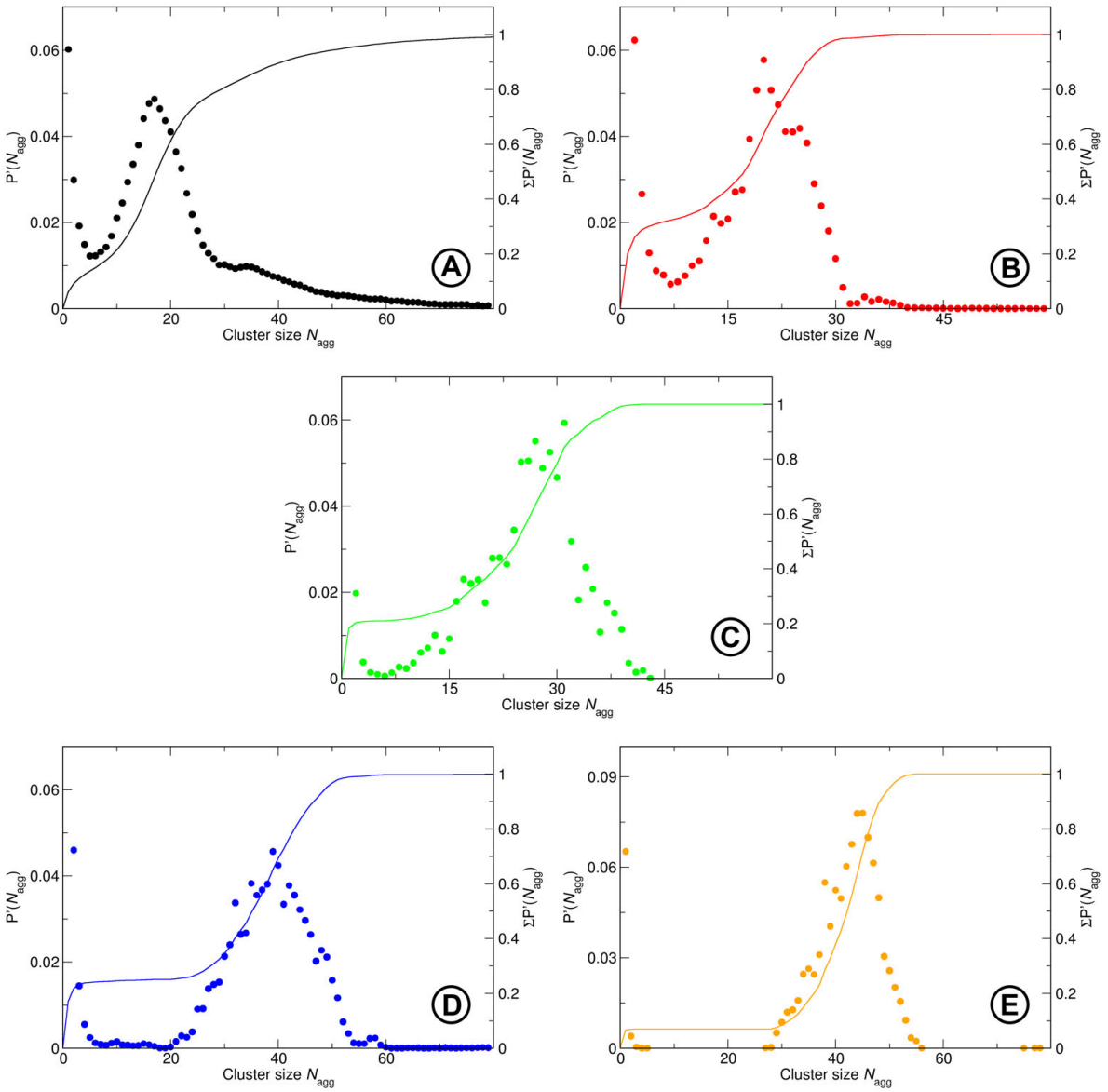

Figure 2.2: Size distributions of **A** OTA, **B** DeTA, **C** DTA, **D** CAP, and **E** DEC micelles. Circles represent the probability for a surfactant molecule to be part of an aggregate of size N_{agg} $P'(N_{agg})$ and lines the running total $\sum P'(N_{agg})$.

The plots further expose strong size fluctuations of the aggregates, that will be discussed in more detail in Section 2.5. For the present consideration it is sufficient to note that all degrees of fluctuations are captured on several occasions and that their period is substantially shorter than overall propagation time. A border case of this statement is the DTA system, where the cycle of fluctuations is in the range of half the simulation time. To quantify distinctive micellization behavior, characteristic histograms of aggregation

numbers are obtained for each system by averaging over the structurally converged sections of the two respective trajectories* in Figure 2.2. Solitary, pronounced maxima in the distributions indicate preferred aggregation numbers close to 16 (OTA), 20 (DeTA), 28 (DTA), 37 (CAP), and 44 (DECA).

However, probabilities decay slowly towards smaller and larger aggregates, covering deviations of up to $\sim 20\,\%$ within the full width at half maximum in case of CAP. Analyses performed on specific aggregation numbers will therefore focus on the most probable micelle N_{agg}^{0} with a tolerance of 15 %, so contributions from slightly larger and smaller micelles enter the statistics. In particular cases, a narrower tolerance may be used and will explicitly be declared.

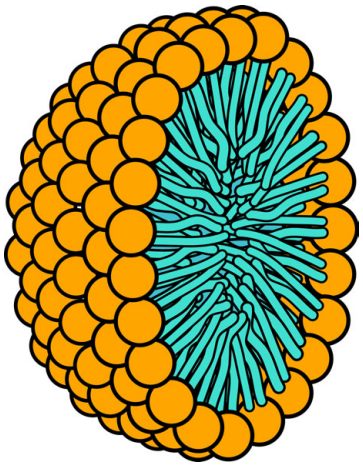

Figure 2.4: Cross-section through an ideal spherical micelle with all hydrophilic head groups (**orange**) forming a sharp, gapless interface and polar tails (**turquoise**) confined to a water-free core region†.

To provide a qualitative impression of the structures to be discussed, snapshots of the average (with regard to their radius of gyration) micelles of N_{agg}^{0} are shown in Figure 2.3. These renderings are noticeably different from idealized representations often encountered, such as Figure 2.4. Although of approximately spherical shape, no smooth surface is formed by tightly packed polar head groups. To the contrary, the interfacial region appears rugged with a considerable portion of the hydrophobic carbon tails exposed to the surrounding medium. This raises the question to what extent the frequently advocated image of a closely confined interfacial region and a strictly hydrophobic core[31,32,171,172] is actually accurate.

*precluding the demixed configuration of DECA as reasoned in the previous paragraph

†Original illustration by MARIANA RUIZ VILLARREAL, taken from URL: https://en.wikipedia.org/wiki/File:Phospholipids_aqueous_solution_structures.svg. Work released into public domain.

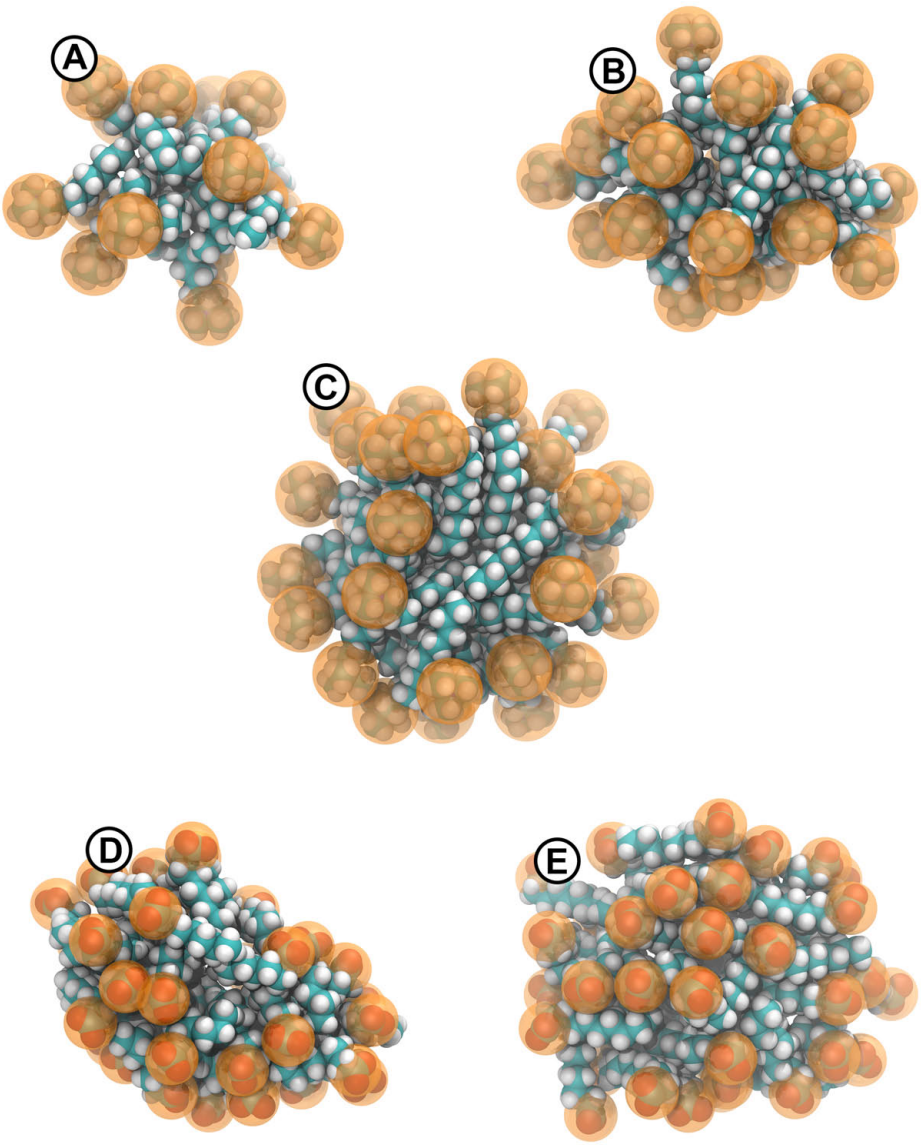

Figure 2.3: Rendering of an average (by means of its radius of gyration) **A** OTA, **B** DeTA, **C** DTA, **E** CAP, and **D** DEC micelle in van der Waals representation. Polar headgroups are encompassed by translucent **orange** spheres.

2.3 Sphericity

Prior to a closer examination of the aggregates, it is useful to assess the degree of symmetry of the formed objects. The shape is expected to be spherical and this assumption is initially confirmed by the snapshots presented in the previous section, but a quantification of this aspect will prove valuable for later considerations. A frequently brought up measure of the sphericity of particles dates back to 1932. It was defined by geologist HAKON WADELL as the ratio of the surface of a sphere having the same volume as the particle to the actual surface of the particle:[173]

$$\Psi = \frac{(\pi)^{\frac{1}{3}} \left(6V_\mathrm{p}\right)^{\frac{2}{3}}}{A_\mathrm{p}}, \tag{2.1}$$

where V_p is the volume and A_p the surface. To illustrate the scaling of this quantity, values of Ψ for some common geometrical shapes are listed in Table 2.1. In case of platonic solids, Ψ approaches unity with growing number of vertices, as would be expected.

Transferring this model to the aggregates formed by surfactant molecules requires an appropriate geometrical envelope for the respective coordinates in the MD trajectory. A prominent example of such a construct is the *convex hull*, which represents the smallest convex shape that contains all points in a set. This envelope is displayed in Figure 2.5 for two point clouds in 2D.

Table 2.1: Sphericity Ψ of various geometrical shapes.

Object	Ψ
tetrahedron	$\left(\frac{\pi}{6\sqrt{3}}\right)^{\frac{1}{3}} \approx 0.671$
octahedron	$\left(\frac{\pi}{3\sqrt{3}}\right)^{\frac{1}{3}} \approx 0.846$
icosahedron	$\left(\frac{\left(3+\sqrt{5}\right)^2\pi}{60\sqrt{3}}\right)^{\frac{1}{3}} \approx 0.939$
ellipsoid with $a = b = r$ and $c = 2r^*$	≈ 0.930
ellipsoid with $a = {}^{r}/_{2}$, $b = r$, and $c = 2r^*$	≈ 0.791

With respect to the shapes suggested by the finite size representation of points proportional to their mutual distances, the convex hull reproduces the degree of spherical symmetry of set **A** well, but by definition skips the concave regions that may be discerned in the outline of set **B**. Surface and volume determined based on this envelope would drastically overestimate the sphericity of not strictly convex micellar structures. Methods exist that overcome this limitation, like *α-shapes*[174] and extensions of the convex hull concept to yield what is sometimes called the *concave hull*.[175,176] Both shall not be discussed in detail here. In grossly simplified terms, surface generation is controlled by a critical geometric parameter based on which a point is either allocated to the surface or to the

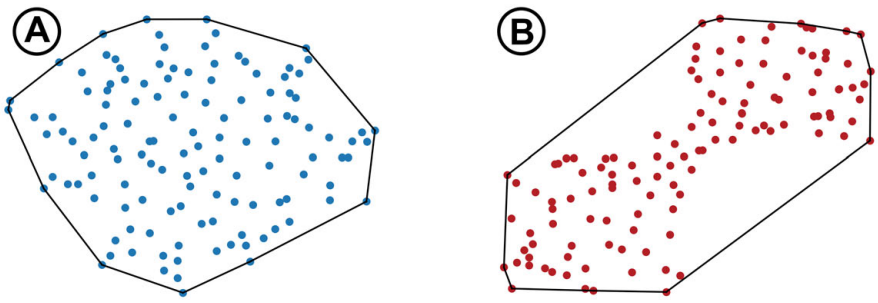

Figure 2.5: Convex hulls of two point clouds in two dimensions traced by solid **black** lines.

*Where, a, b, and c are the principal semi-axes of the ellipsoid.

enclosed volume. Exemplary outcomes of such an approach are sketched in Figure 2.6 for a two-dimensional set of points.

The resolution of facets depends strongly on the choice of this parameter, so these procedures yield no universal representation. In the present case, it seems reasonable to relate this reference value to a description of the extent of the involved particles. Such mappings are given for instance by the van der Waals volume or the inverse of the *solvent accessible volume**. Implementation of these definitions would then result in the van der Waals surface or the *solvent accessible surface* and lead to representations comparable to those shown in Figure 2.7.

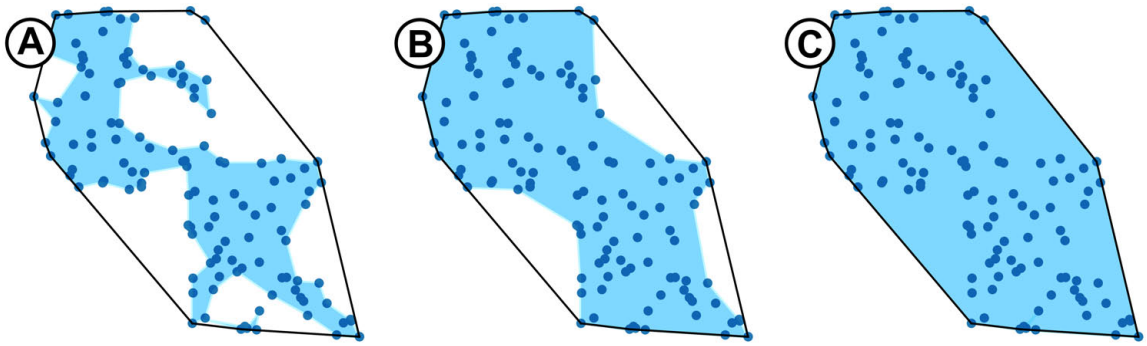

Figure 2.6: Two-dimensional set of points with marked convex hull represented by solid **black** lines and areas enclosed by concave hulls resulting from different threshold parameters colored in **light blue**. Here, a simple distance cutoff is used to decide whether points are part of the volume or designate vertices. The ratio of cutoff values is 1 : 2 : 4 in the order of images **A–C**.†

While these are consistent surface construction schemes, they fail to give a meaningful measure of the "effective" sphericity: both DeTA and CAP micelles give rise to signatures tied to spherical shape in scattering experiments.[141,178] However, it is clear from the renderings that the surface to volume ratio is substantially different for the two objects and would result in severely different values of Ψ. Moreover, the calculated sphericity for neither of the micelles would necessarily give a relevant account of the shape detected by measuring instruments or that responsible for the behavior of the aggregates in solution. In general (and slightly vague) terms, this sought-after representation may be denoted as the "perceived" or "effective" shape. In order to capture this mesoscale outline, the control parameter would need to be reversed towards larger characteristic distances to yield a more convex reconstruction. The reason why it is problematic to achieve consistency with this procedure is also evident from the snapshots: figuratively speaking, the DeTA aggregate

*This volume is implicitly defined by the solvent accessible surface, which will be introduced in Section 2.4.

†Illustrations were generated by making minor adjustments to the open-source JavaScript implementation *d3.geom.concaveHull*.[177]

has a sea urchin-like shape with spines extending radially outward from a compact core. By comparison, the profile of the CAP micelle is relatively even, featuring only moderate protrusions. It is overt that a threshold parameter only just outlining the rough surface of the DeTA micelle within a convex boundary may well ignore true concavities in a CAP micelle surface. The criterion would need to be adjusted individually to the particular packing characteristics of each surfactant to cover distinct variations in interfacial texture.

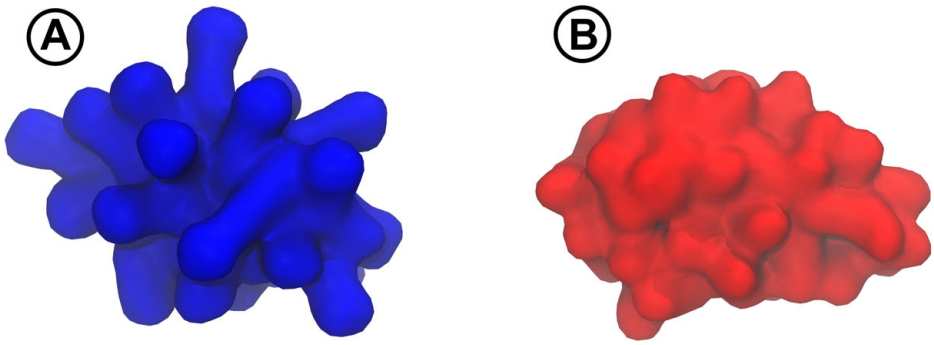

Figure 2.7: Surface representations with equal reconstruction parameters of **A** a DeTA and **B** a CAP micelle.

However, this is hardly possible without prior knowledge regarding which surface features (in e.g. van der Waals representation) are to be considered typical and which represent deformations. This assessment would require rigorous geometrical models of the respective molecular arrangements.

Still, a comprehensive classification of the shape and its fluctuations can be achieved by quantifying deviations from ideal sphericity. It is, however, important to keep in mind, that such information can only be sensibly interpreted by presupposing a certain geometry.

Eccentricity Deviations from spherical shape can be quantified by means of the often used measure of eccentricity:

$$\eta = 1 - \frac{I_{\text{min}}}{I_{\text{avg}}}, \tag{2.2}$$

with I_{min} being the smallest and I_{avg} the average moment of inertia calculated relative to the three principal coordinate axes. Figure 2.8 depicts histograms and corresponding box plots of η for all micelles of N^0_{agg} with a three molecule tolerance. To put this quantity into perspective, it is helpful to translate the principal moments of inertia to the common shape of a homogeneous ellipsoid with the relations:[179]

$$a = \sqrt{\frac{5}{2}\frac{I_{yy}+I_{zz}-I_{xx}}{m}}, \tag{2.3}$$

$$b = \sqrt{\frac{5}{2}\frac{I_{zz}+I_{xx}-I_{yy}}{m}}, \text{ and} \tag{2.4}$$

$$c = \sqrt{\frac{5}{2}\frac{I_{xx}+I_{yy}-I_{zz}}{m}}. \tag{2.5}$$

Here, a, b, and c are the principal semi-axes of the ellipsoid, m the mass of the micelle, and I_{jj} the principal moments of inertia ordered by magnitude such that $I_{xx} \leq I_{yy} \leq I_{zz}$. Important statistical properties of the distributions, as well as the calculated respective semi-axes are listed in Table 2.2. The calculated distributions of the principal moments of inertia are found in the supplementary section 2.A.

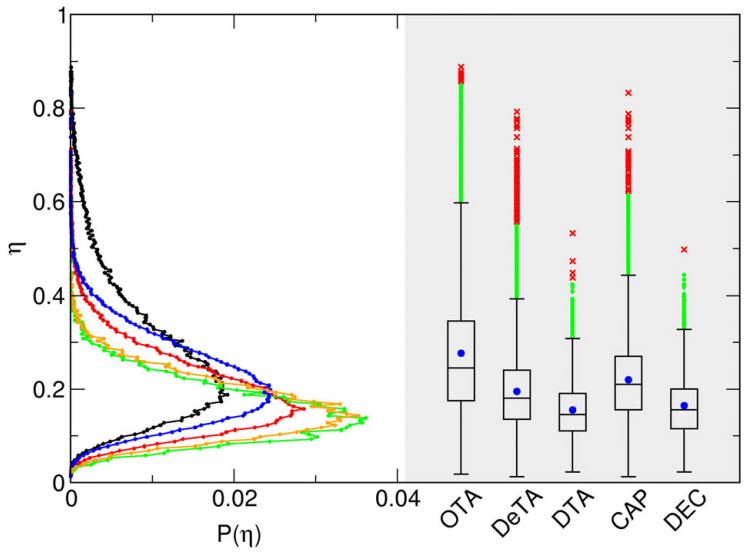

Figure 2.8: Histograms of the eccentricity η of OTA (**black**), DeTA (**red**), DTA (**green**), CAP (**blue**), and DEC (**orange**) micelles.

The range of eccentricities is in good agreement with results for comparable micellar structures.[180] Most micelles can be mapped to slightly ellipsoid objects. The greatest difference between the principal semi-axes is detected for OTA aggregates, that accordingly exhibit the highest eccentricity. For both anionic and cationic surfactants, a trend towards higher sphericities is observed with increasing alkyl chain length. The same is true for the fluctuations that are strongest for OTA/CAP and lowest for DTA/DEC. To further give an impression of the scaling of η, the eccentricity of a homogeneous ellipsoid with principal semi-axes proportions $1 : 1/2 : 2$ is $\eta = 0.65$, that of a prolate ellipsoid with $1 : 1 : 2$ is $\eta = 0.5$.

Table 2.2: Mean values of eccentricity $\bar{\eta}$ and interquartile ranges IQR of the distributions by species. In addition, the principal semi-axes *a*, *b*, and *c* of homogeneous ellipsoids with principal moments of inertia identical to those of the micelles are given, as well as the proportions of these.

Species	$\bar{\eta}$	IQR	*a*	*b*	*c*	$a : b : c$
			(nm)			
OTA	0.28	0.17	1.72	1.27	1.06	1.35 : 1 : 0.83
DeTA	0.19	0.11	1.71	1.40	1.20	1.22 : 1 : 0.86
DTA	0.16	0.08	1.86	1.59	1.40	1.17 : 1 : 0.88
CAP	0.22	0.12	1.81	1.44	1.21	1.26 : 1 : 0.84
DEC	0.16	0.09	1.87	1.57	1.38	1.19 : 1 : 0.88

Juxtapositions by aggregation number are shown in Figure 2.9 for DeTA, DTA, CAP, and DEC. For this purpose additional analyses were performed for smaller and larger aggregates that occur with similar probabilities. For the cationic species, eccentricities follow the order $\bar{\eta}_- > \bar{\eta}_0 > \bar{\eta}_+$, with subscript '$_-$' denoting the lower, '$_0$' the intermediate, and '$_+$' the higher aggregation number. For the anionic micelles, the opposite trend is observed, albeit only weakly in case of DEC. Just as the disparity in surface complexion mentioned earlier, this points to fundamental differences in molecular organization, that will be elucidated further throughout this chapter.

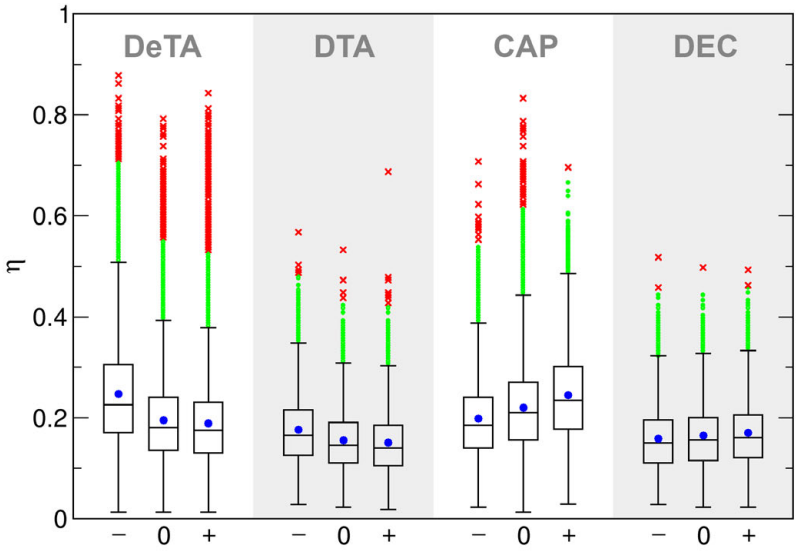

Figure 2.9: Box plots of the eccentricies η of N_{agg}^0 ('0'), slightly smaller ('-'), and slightly larger ('+') micelles for DeTA, DTA, CAP, and DEC. The concerned species is marked in the respective compartment of the diagram.

The ideal aggregate As reasoned above, the convex hull is an impractical envelope definition if it cannot be ascertained that the set of points never describes a (*effectively*) concave surface. However, in individual cases the accuracy of that approach can very well be estimated. To this end, a search for the most compact micelle is performed by means of the aggregate that minimizes the smallest sphere encompassing all involved molecules (*smallest bounding sphere*, SBS). Examining the identified structures in Figure 2.10, the assumption that these objects can sensibly be treated in a scheme of positive curvature is certainly justified. Along these lines, the maximum sphericity Ψ_{max} of each micelle species, that is dictated by the surfactant specific ordering, can be determined according to Equation (2.1) and is summarized in Table 2.3.

Table 2.3: Sphericities Ψ of the N_{agg}^{0} micelle producing the smallest bounding sphere by species.

Species	Ψ_{max}
OTA	0.95
DeTA	0.96
DTA	0.94
CAP	0.94
DEC	0.95

The outcomes uniformly show that the investigated surfactant molecules can indeed assemble to objects of high spherical symmetry. It is important to note that the upper limit of Ψ in this approach is necessarily smaller than unity due to the polyhedral shape reconstruction with a finite number of vertices. For this reason, and the manual confirmation of convexity, the presented values are to be taken as a general guideline rather than quantitative results. It should also be emphasized that this reflects a conservative estimate, the convergence of which depends on the extent of the simulation. The most compact micelle that can emerge in the ensemble represents a distinct (unknown) configuration that can only be adequately approximated by sufficient sampling.

Estimation of concavity While eccentricity quantifies deviations from sphericity, it does not provide insight on the type of deformations, for this information cannot be recovered from the inertia tensor. However, transitions to concave shape or the formation of cavities can be accessed from the convex hull volume. As stated earlier, the volume is overestimated in these cases. For this reason, changes in sign of local curvature show up as density fluctuations in the convex hull volume. Figure 2.11 shows histograms and box plots of the particle density inside the convex hull relative to the density determined for the ideal micelle, n_{ch}^{*} (cf. penultimate paragraph).

Notably, the graphs do not terminate exactly at $n_{\text{ch}}^{*} = 1$, since there are rare cases where, due to particular atom configurations, a tighter envelope is calculated than for the most

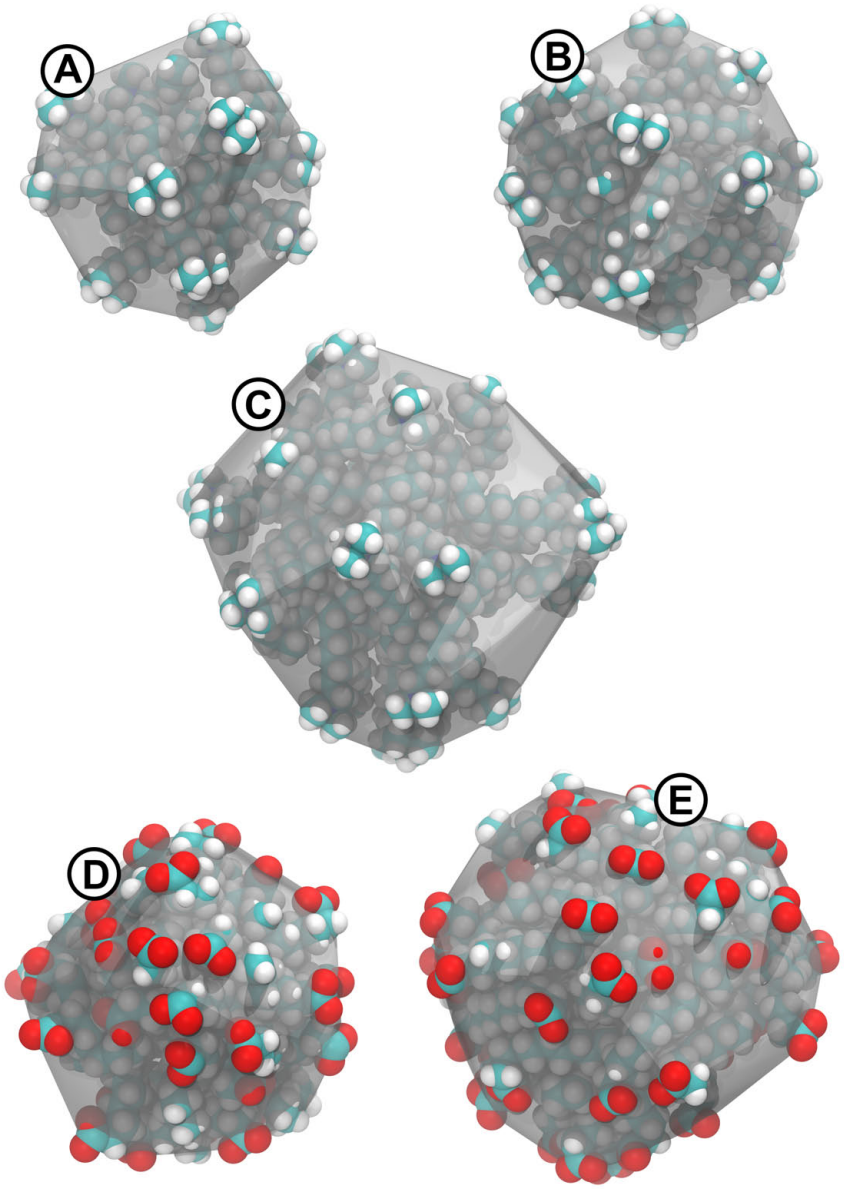

Figure 2.10: Renderings of the most compact **A** OTA, **B** DeTA, **C** DTA, **D** CAP, and **E** DEC micelle. A representation of the convex hull surface is shown around the clusters in translucent **grey**. Although all coordinates lie inside the convex hull, the van der Waals representation chosen for better visibility does not.

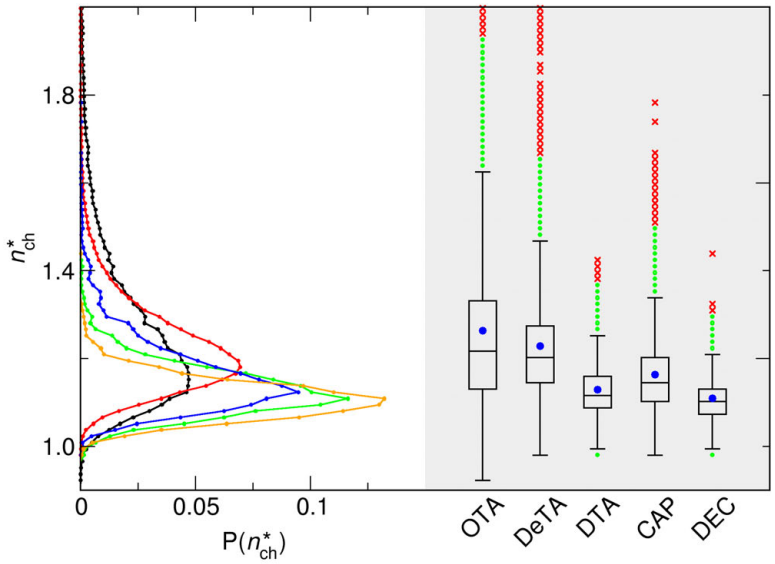

Figure 2.11: Histograms of the deviation of the particle density inside the convex hull of OTA (**black**), DeTA (**red**), DTA (**green**), CAP (**blue**), and DEC (**orange**) aggregates from that of the respective ideal micelle n^*_{ch}.

Species	$\bar{n}^*_{ch}$	IQR
OTA	1.26	0.20
DeTA	1.23	0.13
DTA	1.13	0.07
CAP	1.16	0.10
DEC	1.11	0.05

Table 2.4: Mean values of n^*_{ch} and interquartile ranges IQR of the distributions by species.

spherical micelle. Yet this merely introduces a minor offset that is not relevant in the comparison of graphs, especially since the error is of equal magnitude in all incidents. The data collected in Table 2.4 shows that the least concave structures are detected for the long-chained surfactants DTA and DEC, closely followed by CAP, while DeTA and OTA micelles on average deviate more from convex shape. Again, fluctuations obey the same trend. A comparison of the averages of η and n^*_{ch} in Figure 2.12 gives a clear picture of the differences in grading resulting from the two criteria. Choosing the DeTA and DTA positions as anchor points for CAP and DEC, respectively, the anionic surfactant molecules form objects of higher eccentricity as well as higher convexity, which points to an overall more elliptical shape. This reflects the dependency of micelle geometry on the dimensions of head groups as well as the polar tail.[181]

In order to assess the scale of correlation between eccentricity and concavity, a scatter plot of η versus n^*_{ch} for DeTA is shown in Figure 2.13. The omnidirectional distribution indeed confirms that the two criteria capture mostly independent forms of distortion.

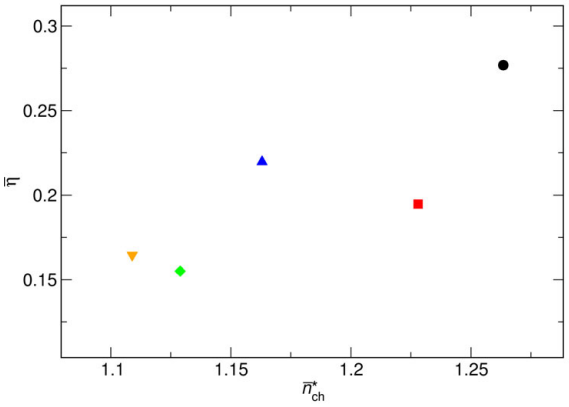

Figure 2.12: Mean eccentricity $\bar{\eta}$ of OTA (**black**), DeTA (**red**), DTA (**green**), CAP (**blue**), and DEC (**orange**) micelles versus average particle density inside their convex hull relative to that of the respective ideal micelles $\bar{n}^*_{ch}$.

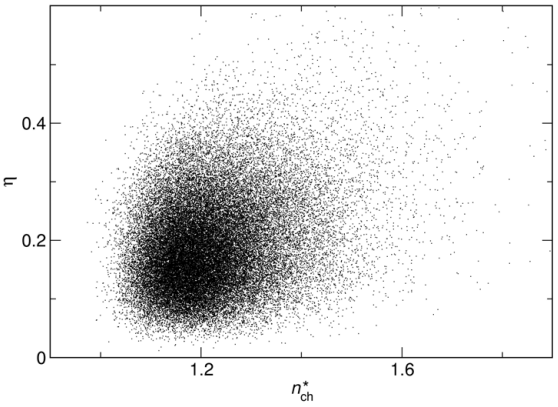

Figure 2.13: Scatter plot of eccentricities η of DeTA micelles of size N^0_{agg} and particle densities inside the convex hull, normalized to that in the ideal micelle n^*_{ch}.

2.4 Structure of the micelles

A first measure of the micellar structure is obtained by the radial distributions of system components around the geometric centers of the aggregates shown in Figure 2.14. Assuming on average spherical shape, the local densities of alkyl chains, polar headgroups, the monatomic counterions, and water are obtained as one-dimensional functions of the distance. A clear hierarchy is discernible, with the apolar hydrocarbon tails forming the central region followed by a bell-shaped maximum of the polar head groups and in short distance a layer of counterions. The density of alkyl chains decays swiftly with increasing distance, but extends far into the interfacial region. Conversely, water penetrates as close to the core as the interfacial peak. This draws the picture of a diffuse, "soft" interface as opposed to the prospect of a strictly hydrophobic micelle interior separated from the solvent by a gapless layer of polar head groups.

Nevertheless, a dry region still exists inside the aggregates that can be quantified by determining the smallest sphere in its interior that does not overlap with any water molecule. Histograms of the hydrophobic core radii r_d are depicted in Figure 2.15 for the investigated micelles. In all cases, the core size has a distinct maximum and fluctuates with an amplitude of 0.07 nm around the central value. Table 2.5 lists the average hydrophobic core radius, width of the respective distribution, and an estimate of the micelle radius obtained using the most probable head group position as a general measure for the location of the interfacial plane.

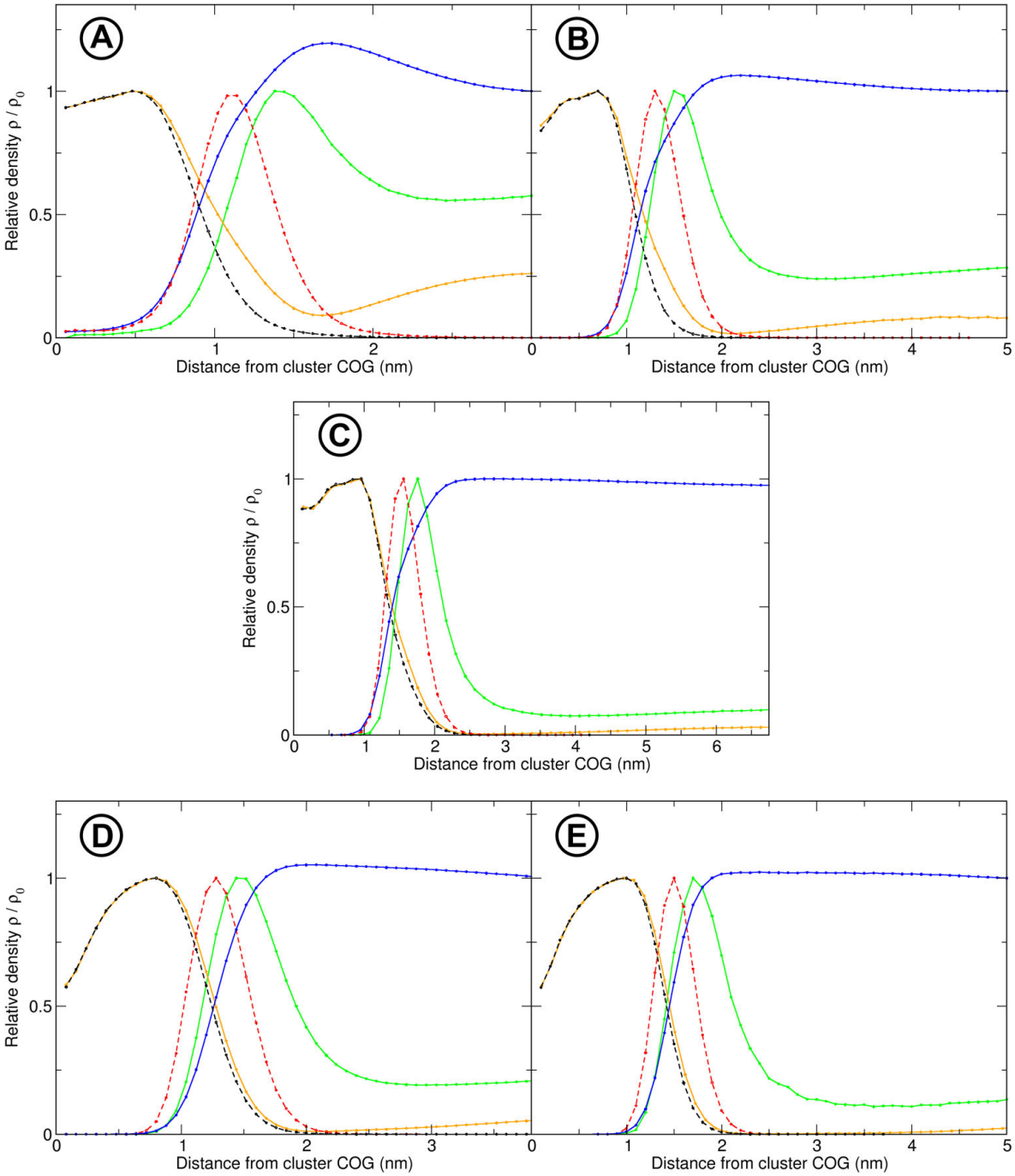

Figure 2.14: Radial distribution of the system components around the geometric center of **A** OTA, **B** DeTA, **C** DTA, **D** CAP, and **E** DEC micelles. The surfactant density is colored **orange**, counterion density **green**, and water density **blue**. In addition, the density of surfactant molecules constituting the aggregate is decomposed into contributions from the alkyl tail and head groups, which are traced by dashed lines of **black** and **red** color, respectively.

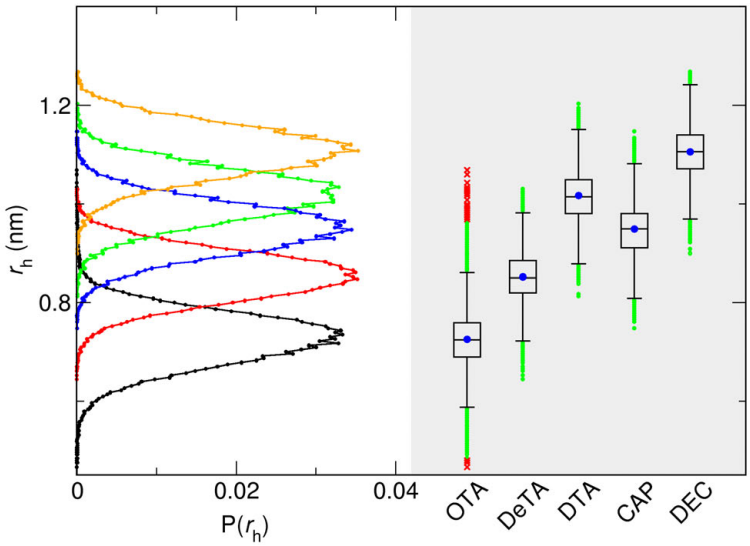

Figure 2.15: Histograms of hydrophobic core radius r_d and corresponding box plots for OTA (**black**), DeTA (**red**), DTA (**green**), CAP (**blue**), and DEC (**orange**) micelles.

Table 2.5: Mean values of the hydrophobic core radius $\bar{r}_d$ and interquartile ranges of the distributions IQR by species. In addition, the two rightmost columns list the radii of the micelles determined by means of the radial position of the maximum of polar head group density r_{hg} and the difference between this measure and the mean radius of the water-free core.

Species	$\bar{r}_d$	IQR	r_{hg}	$r_{hg} - \bar{r}_d$
	(nm)			
OTA	0.72	0.07	1.1	0.4
DeTA	0.85	0.07	1.3	0.5
DTA	1.00	0.07	1.6	0.6
CAP	0.95	0.07	1.3	0.4
DEC	1.10	0.07	1.5	0.4

It is noteworthy that the water-free volume in CAP micelles is nearly 40 % larger than that in DeTA micelles, although both are of virtually identical diameter. Very similar proportionality is observed in a comparison of DTA and DEC aggregates. Irrespective of these differences, the hydrophobic domain is in each case significantly smaller than the aggregate radius. Thus, the notion of the entirety of alkyl chains being isolated from water greatly overestimates the dimension of the actual water-free core. Not only the polar sections of surfactant molecules are in contact with water, but hydration extends at least to some elements of the alkyl chain. Figure 2.16 quantifies this penetration by

water into DeTA, DTA and CAP micelles by means of the relative residual hydration that is determined as the number of water molecules in the first solvation shell of each group normalized to the value obtained for a single surfactant molecule in water.

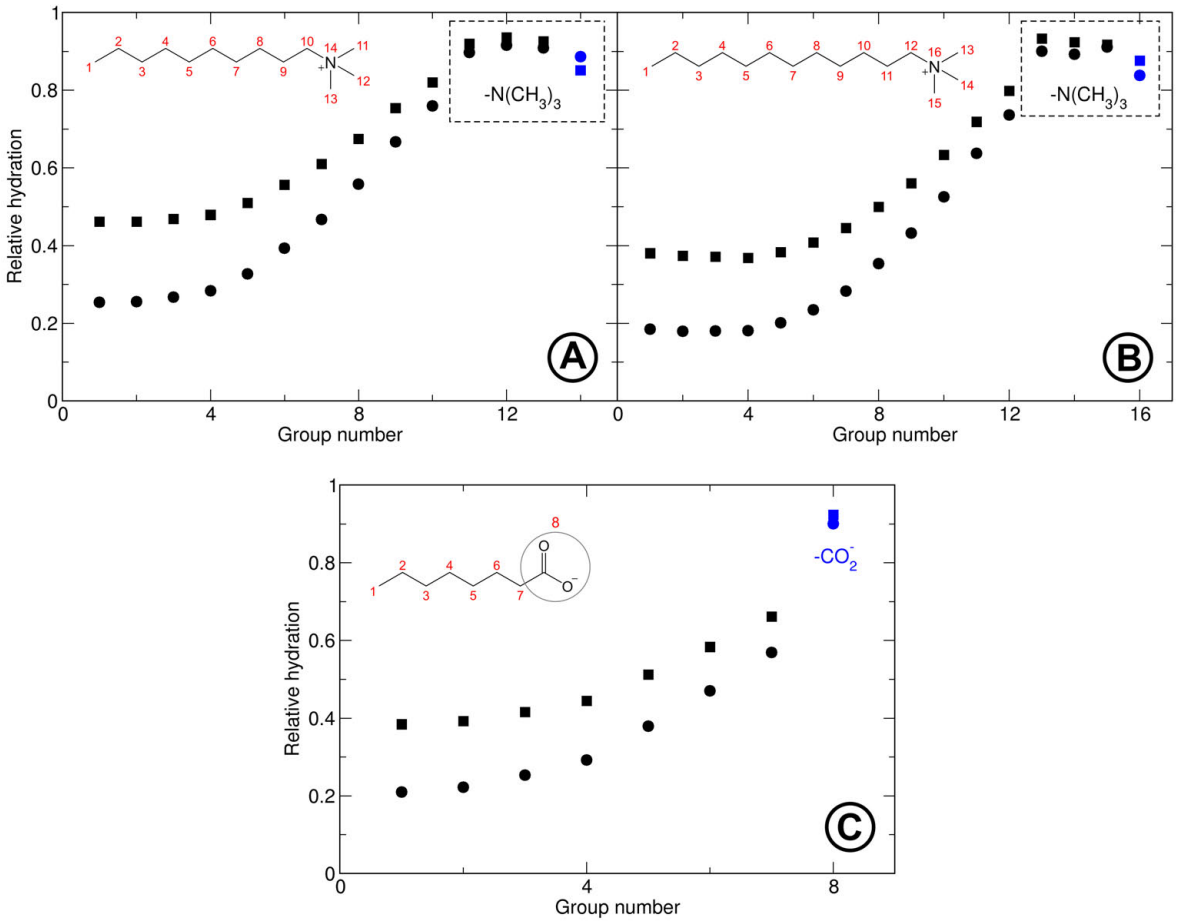

Figure 2.16: Relative hydration of atom groups in **A** DeTA, **B** DTA, and **C** CAP. The respective enumeration follows that specified in the included structural formulae. Squares designate analysis of micelles of N_{agg}^{0}, circles systemwide evaluation.

A distinct classification of methylene and ethylene residues is discernible for both cationic and anionic micelles, with the C1 constituents being the least hydrated and the number of water contacts gradually increasing along the chain towards the polar head groups. The lowest hydration of these units is observed for DTA, but even here relative hydration does not subside to less than 18 % for the tail sections and strongly increases towards the amine group. The slope is substantially steeper for the cationic residues, leading to a hydration level of 76 % for the C10 and C12 moieties in DeTA and DTA, whereas the CAP C7 residue reaches merely 47 %. This difference can be ascribed to the surfactant specific ordering qualitatively described in the previous section and also observed in the

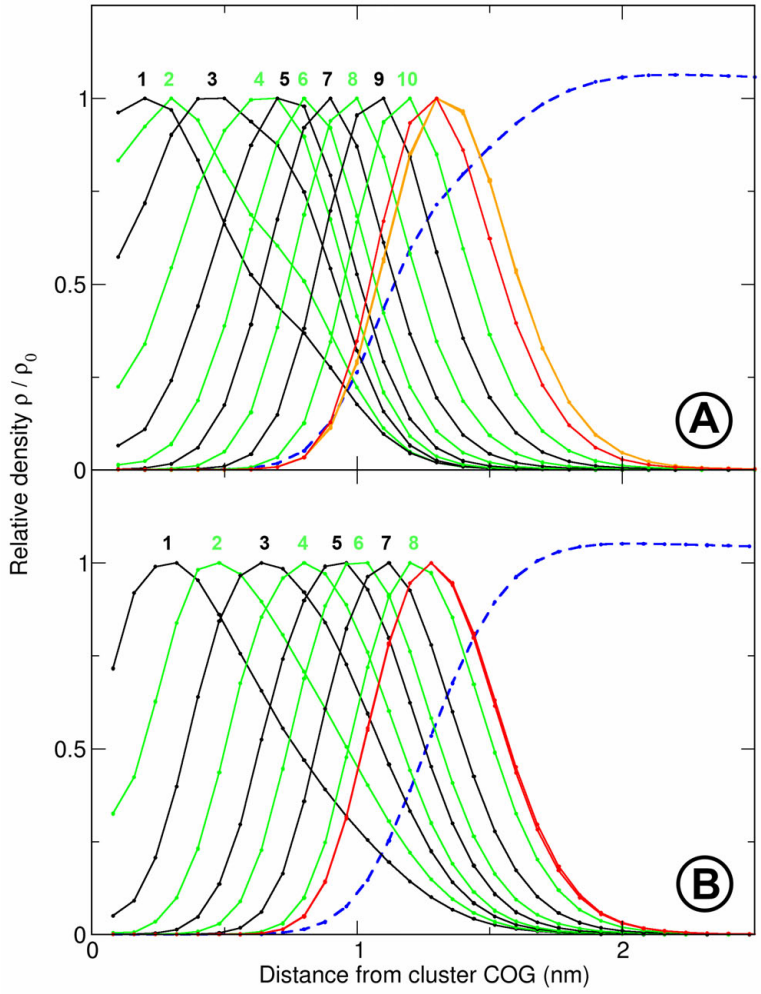

Figure 2.17: Distribution of surfactant heavy atoms around the aggregate COG in **A** DeTA and **B** CAP. Carbon atoms are alternatingly colored **black** and **green** and are enumerated above the graphs, nitrogen and oxygen are **red** and the $-N(CH_3)_3$ methyl groups are **orange**. In addition, water density is depicted as a dashed **blue** line.

snapshots in Section 2.3: the amine head groups are uniformly oriented towards the solvent, thereby creating a radial array of roughly cylindrical hydrocarbon annexes with interstices exposing the outermost portions of alkyl tails to the solvent. By comparison, the surface of CAP aggregates is relatively smooth. Here, too, apolar tails partially lie bare, but in a first assessment this is rather due to peripherally attached molecules than the formation of pores in the surface. This geometric distinction also explains the difference in hydrophobic core size between the similarly dimensioned cationic and anionic aggregates and can further be quantified by a plot of the radial distributions of alkyl units in Figure 2.17.

In both cases, the peaks describe a categorical sequence with the C1 carbon atoms accumulated in the core and the consecutive units along the alkyl chain iteratively staggered to larger radii. It should be stressed, however, that methyl groups have a finite probability to be located anywhere inside the micelle, even close to the interfacial region, which is in agreement with neutron scattering and NMR results.[182,183] The decay of C1 and C2

densities is much slower in case of the anionic surfactant and both curves extend far across the oxygen peak. At $r = 0.5$ nm, the relative C1 density of CAP is still greater than 80 %, whereas for DeTA it has already dropped to $\sim$ 65 %. In parts this can be attributed to the higher ellipticity of CAP aggregates. However, the deviations (cf. Section 2.3) from spherical shape are not altogether strong enough to fully explain the extent of methyl groups present at large distances from the COG in this radial symmetric approach. Severe ellipsoidal or concave deformations would conversely result in considerable head group density close to the geometric center, which is not observed in either diagram. More likely, the behavior can be taken as further confirmation of a less rigid radial hierarchy in the CAP micelles and a higher fraction of peripherally integrated molecules.

In addition, dissimilarities in curve shape are noticeable between CAP and DeTA for the carbon atoms constituting the alkyl tail. Initially, the densities of DeTA alkyl residues subside equally smoothly but, by contrast, feature an inflection point, which in case of C1 is located close to $r = 0.5$ nm. This suggests a subdivision of geometrical configuration that can be interpreted with the aid of the snapshot series presented in Figure 2.18.

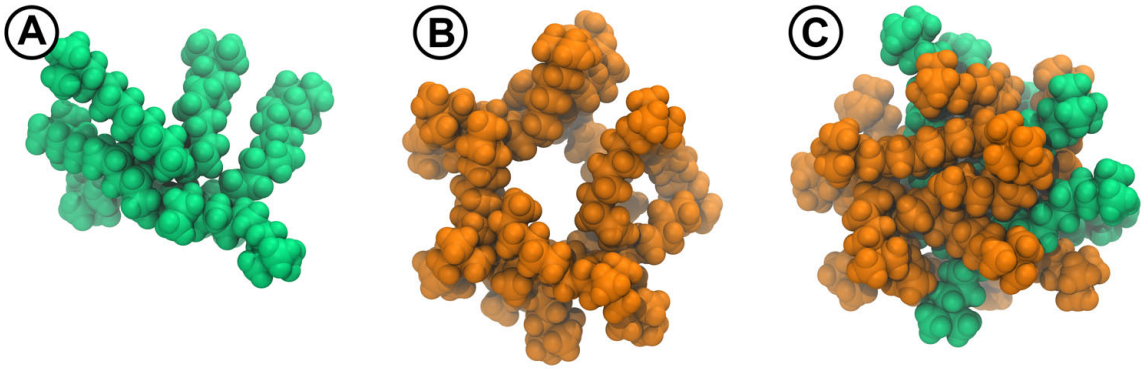

Figure 2.18: Snapshots of molecules constituting a DeTA micelle with **A** any atom or **B** no atom situated inside a sphere of radius 0.5 nm around the COG. **C** shows the whole aggregate assembled from **A** and **B**, retaining the coloring of the separated illustrations.

Molecules in the micelle are split into two classes: one that comes closer than 0.5 nm to the COG and one that is farther away. The molecules extending to the core section are in good approximation radially aligned, with amine groups pointing away from the center. The alkyl tails of the complementary fraction are laterally attached to this framework, together forming a self-contained nucleus. Only the polar groups directly bend toward the solvent, necessarily lifting a portion of the alkyl chain from that core. The situation is very similar for the investigated DTA aggregates and a decomposition can be done on the same grounds. The corresponding analysis is found in the supplementary section 2.B. These findings agree with a study by AOUN et al., who also found incidents of elongated configurations extending to the aggregate center in conjunction with tangentially incorporated molecules in C_X—trimethylammonium bromide micelles.[184]

The radial ordering can be quantified by introducing a simple order parameter φ, which is defined as the angle between the direct connection of C1 and C9 and the vector from the COG to the nitrogen atom. Figure 2.19A shows the distributions of φ for DeTA molecules coming closer than 0.5 nm to the geometric center and those beyond this radius. Evidently, the inner group is aligned more parallel to this radius than the complementary group, with average angles $\bar{\varphi} = 20°$ and 37°, respectively. Given the intermediate bending of tangentially incorporated molecules necessary to achieve outwards directionality of the head groups, the second angle is naturally underestimated, since the connection vector from C1 to C9 skips this intermediate region. Indeed, considering only the connection from C1 to C4 yields an average angle of $\bar{\varphi} = 47°$ for the outlying subset.

Although no indicator of a subdivision is found in the density distributions of alkyl units for CAP, the same analysis* yields a very similar result, as depicted in Figure 2.19B. An average angle of $\bar{\varphi} = 20°$ for the inner group suggests that inside the core region, where no head groups are present, packing characteristics are indeed comparable. The C1-C7 connection vectors of molecules outside this central zone are on average inclined at an angle of 47° to the COG-C8 radius. Moreover, the distribution is considerably broader than in case of DeTA, with an IQR of 32° opposed to 18°, which is in line with the presumed less geometrically restricted incorporation of monomers in this outer shell. For the sake of completeness, renderings of the decomposition of a CAP micelle are also found in the supplementary section 2.B.

This self-organization is an equilibrium controlled result of the interplay between hydrophobic interactions and repulsions of the charged head groups, complicated by steric constraints: on the one hand, high surficial density of polar headgroups is necessary to optimally shield the apolar alkyl tails from water (or vice versa, considering the origin of the hydrophobic interaction) that can only be achieved by incorporating a sufficient number of surfactant molecules. On the other hand, the aggregation number is limited by long range repulsions between the polar groups.[73] Tenacious stacking of linear molecules does not necessarily lead to a concluded object adopting this molecular count. Rather, its shape and required particle number (if it is no continuous entity) would be governed by the dimensions of tail section and head group relative to each other†.[185]

The resulting assembly necessarily constitutes a structural compromise, that in the case of DeTA involves a few nearly linear aliphatic tails filling the innermost core, entwined by a number of additional molecules that in sum provide a sufficient density of polar groups to form a stable aggregate. At first glance, this particular arrangement may appear similar to the configuration predicted by the Dill-Flory model,[30] in that order is highest in the micelle center and progressively dissolves towards the outside of the hydrophobic core. In the present case, however, this is merely true from a perspective of spatial array. A distinct partition of molecules into crystal-like and liquid-like populations by means of carbon

*In this case, φ is defined as the angle between the C1 and C7 connection and the vector from the COG to the C8 methylene group.

†In a simplified geometric approach, that is, however, sufficient for this line of argument.

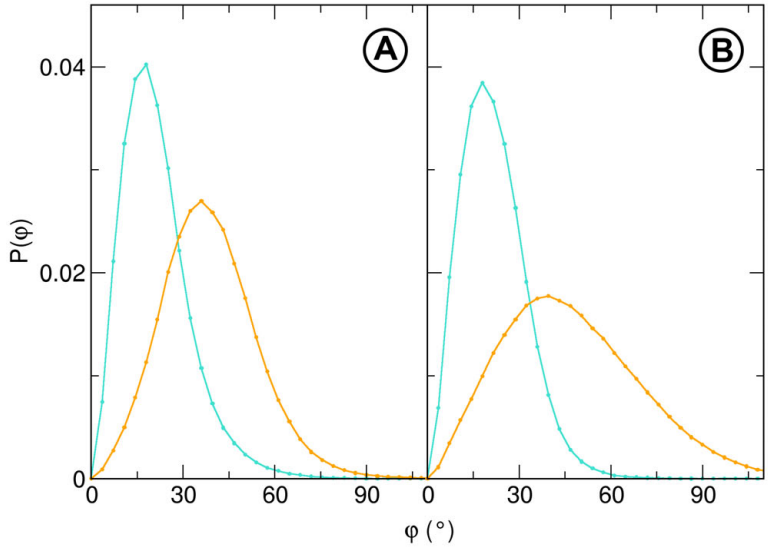

Figure 2.19: Histograms of the angle φ between the connection vectors of **A** C1 and C9 and the aggregate COG and nitrogen in DeTA micelles and **B** C1 and C7 and the aggregate COG and C8 in CAP micelles. **Turquoise** lines show the distribution for the subset of molecules coming closer than 0.5 nm to the geometric center and **orange** lines that for the remaining molecules.

chain order is not justifiable. In accord with the visualizations, the tangential surfactant molecules do not exhibit significantly more *gauche* defects than the radially aligned ones: the probability of *trans* dihedral alignment along the chain is 68 % for the former and 71 % for the latter. Both values are higher than the determined 65 % for a monomer in aqueous solution but do not differ greatly from each other. A major factor contributing to this, albeit small, discrepancy is very possibly the aforementioned intermediate bending necessary to orient the head groups towards the polar medium.

In fact, the structural subdivision is well described by the general notion of HAYTER and ZEMB, that "a fraction of the chains [is] wrapped onto a rather more ordered skeleton", which the authors describe as "exhibiting some degree of radial order".[178]

The noted overall increase in probability of *trans* configurations upon micellization has also been documented in NMR and Raman measurements,[186,187] as well as early computer simulations.[188] For CAP this increase is of a magnitude similar to DeTA, rising from 56 % for a free monomer to 63 % in the micelle.

With the structural preconditions established, insight into water exposure can be further refined by determining the *solvent accessible surface area*. The SASA characterizes the outline of a molecular structure as described by the center of a spherical probe of given radius gliding along its van der Waals surface.[189] The probe in the present analysis is of typical radius 0.14 nm and the van der Waals radii are taken from Ref. 190. Figure

2.20 shows SASA histograms and box plots of the most probable micelles of all surfactant species.

For reasons of clarity, extracted key data is summarized in Table 2.6. As expected, the rough surface of the DeTA relative to the CAP aggregates at similar diameter gives rise to an offset of the distribution to higher surface areas. However, quantitative association would require equal shape that is not given as per the previous section. The SASA increase from DeTA to DTA is significantly higher than that from CAP to DEC. Since DTA aggregates are in fact more spherical than DeTA structures, this, too, can be attributed to the gappy surface of the C_X—trimethylammonium micelles, that accretes very differently with diameter than the more regular *n*—carboxylate surface*. This interpretation also explains the fact that fluctuations are highest for DTA, although it is the micelle species exhibiting the least variation in shape.

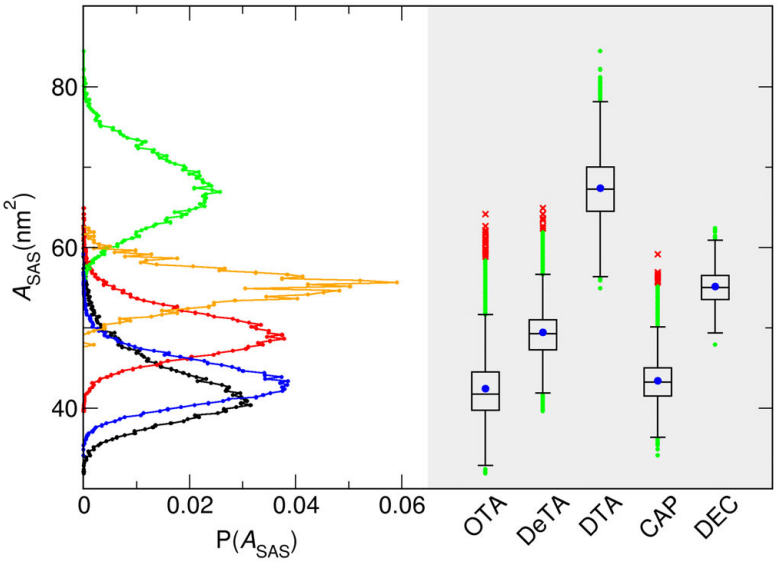

Figure 2.20: Histograms of the solvent accessible surface area A_{SAS} of OTA (**black**), DeTA (**red**), DTA (**green**), CAP (**blue**), and DEC (**orange**).

Species	$\bar{A}_{SAS}$ (nm^2)	**IQR**
OTA	42.4	4.8
DeTA	49.5	3.7
DTA	67.4	5.5
CAP	43.4	3.5
DEC	55.1	3.0

Table 2.6: Mean values of the SASA $\bar{A}_{SAS}$ and interquartile ranges IQR of the distributions by species.

The absolute SASA values can be made more conceivable by a coarse sample calculation. In the previous section, the inertia tensor of DTA micelles was exemplarily mapped to a homogeneous ellipsoid with principal semi-axes 1.86 : 1.59 : 1.40. Direct comparison of the surface area of such an ellipsoid with the determined values of the SASA would be inadequate due to the inherent roughness of the reconstruction. The surface outlined

*It is useful to explicitly refer to Table 2.5 for this argument, which shows that the approximate diameters of DeTA and DTA micelles, as well as the difference in diameter match very well with the values obtained for CAP and DEC.

by a finite size probe gliding over individual volumes of similar scale is necessarily larger than that of a smooth ellipsoid. Therefore, an ellipsoid volume with the denoted principal semi-axes is generated by tight packing of tetramethylammonium ions* for comparison. The rationale behind introducing this configuration is that it approaches the SASA that would emerge from gapless arrangement of trimethylammonium head groups. This gives an estimate of the lower limit of the surface area in this treatment, which amounts to 49.2 nm^2. The actual value of 67.4 nm^2 is 37 % larger, which constitutes a quantitative confirmation that the micelle surface must be interspersed with crevices that enable water penetration.

In a next step, the solvation shell can be analyzed in terms of the proximal and radial distribution of water molecules relative to the micelles classified by the number of formed water-water hydrogen bonds in Figure 2.21.

The proximal distributions give a comprehensive account of the perturbance of hydrogen bond formation close to the micelle surface. The probability to encounter four fold and higher coordinated water molecules decreases considerably with the distance. Accordingly, the relative number of water molecules forming three or less hydrogen bonds is enhanced. The situation is evidently more pronounced for CAP aggregates, where the carboxyl groups provide dedicated hydrogen bonding sites. Conversely, the charged nitrogen atom is shielded by only slightly polar methyl residues that do not constitute favorable partners in the formation of mutual hydrogen bonds.[191]

In the radial distribution around CAP micelles, the local alteration of hydrogen bonding probabilities close to the interface shows up in form of maxima in the densities of three and less fold coordinated water molecules at radii close to 1.5 nm. This feature coincides with the peak probability of carboxyl groups. Conversely, no local enhancement of concentration is visible for either DeTA or DTA. This is a further consequence of the repeatedly pointed out higher surface roughness. Water molecules enter deeper into the micellar surface than into the anionic aggregates which leads to radial blurring of the graphs. Neither do the localized head groups promote visible enhancement of any coordination number due to the aforementioned lack of a specific bonding site.

*The minimum permitted distance between two mutual atoms is set to 0.2 nm.

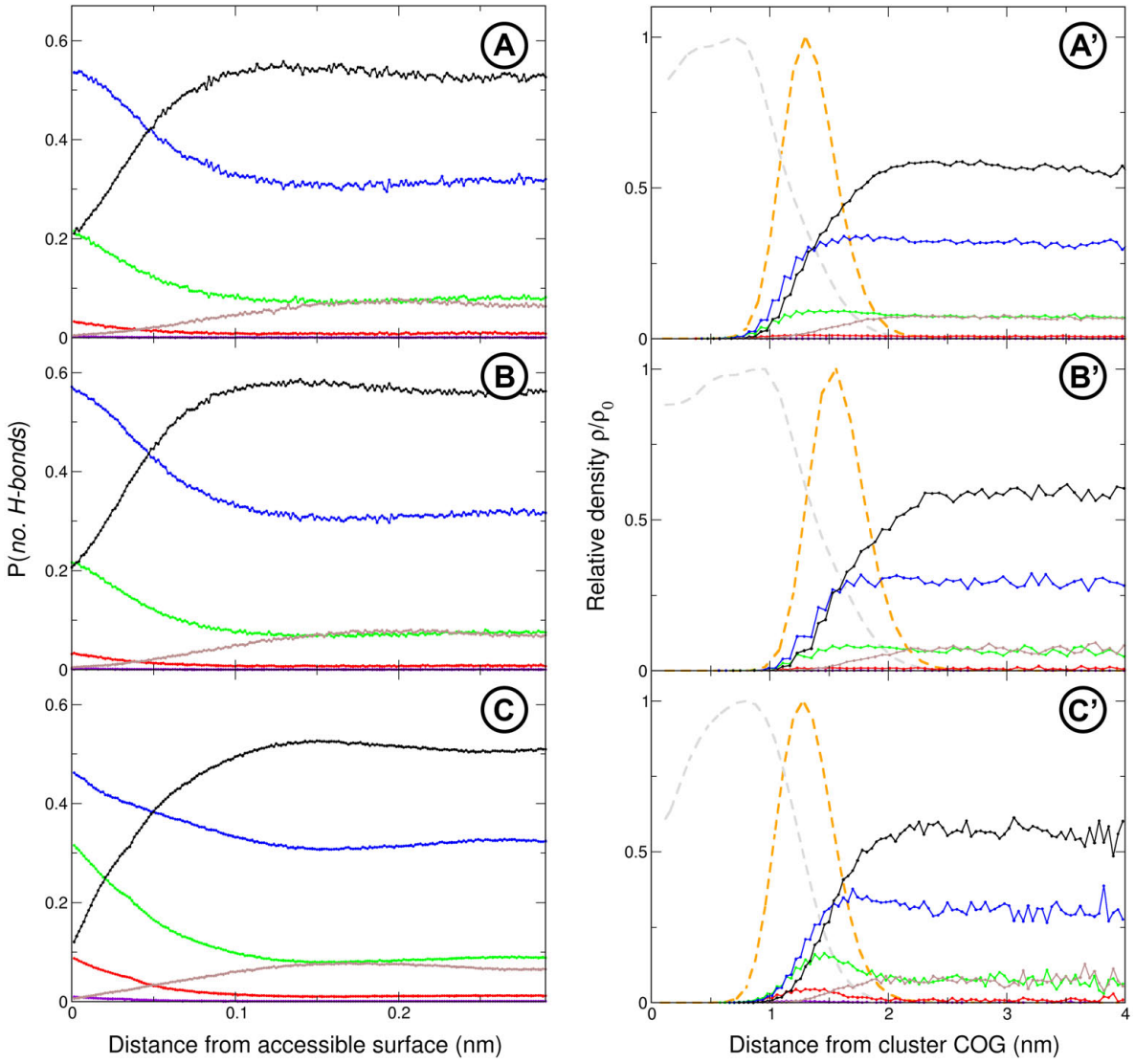

Figure 2.21: Structural properties of the aqueous phase around **A** DeTA, **B** DTA, and **C** CAP micelles. Primes appended to the specifiers formally separate two different visualization schemes. *Left column*: Probability for a water molecule to be involved in the formation of a specific number of hydrogen bonds P(*no. H-bonds*) as a function of the distance to the accessible surface of aggregates. *Right column*: Relative density of water molecules involved in the formation of a specific number of hydrogen bonds as a function of the distance to the centers of geometry of aggregates. The following color code globally applies to the number of hydrogen bonds: **0**, **1**, **2**, **3**, **4**, 5. Contributions from higher coordination numbers identified due to the simplicity of the approach range too close to the baseline to be resolved or are not detected at all. Dashed grey and **orange** lines show the alkyl tail and head group densities, respectively.

2.5 Dynamic properties

As noted in Section 2.2, the trajectories are sufficiently extensive to capture ample information about size fluctuations of the micelles. By labeling aggregates based on the indices of molecules it is composed of at a specific starting frame, individual structures can be traced over time. In the concept developed for this purpose, the micelle is detected in each step as the object that contains the highest number of molecules that formed the aggregate in the previous step*. An exemplary tracking of the aggregation number of an isolated DeTA micelle is shown in Figure 2.22.

The original data exhibits short-term fluctuations of varying intensity superimposed on a much slower oscillation around the preferred aggregation number. These spikes are, in a sense, artifacts of the clustering algorithm produced by collisions with other aggregates that are of no lasting consequence. Nevertheless, this flickering behavior impedes direct determination of the monomer exchange rate without a further criterion that unequivocally separates curve features reflecting "true" changes in aggregation number from statistical events. This difficulty can be evaded by considering the decay of molecules found in a micelle at the initialization of analysis with time. The data resulting from numerous runs are depicted in Figure 2.23 alongside an averaged graph and a fitted curve for all investigated surfactant solutions.

In all cases, the depletion of initial molecules is very well described by an exponential decay with characteristic exponent. The monomer exchange rate can be accessed from this degression by combinatorial considerations. To begin with, it is helpful to reformulate the problem based on the following two assumptions:

*Consequently, at the moment a molecule that was part of the micelle migrates beyond the cutoff range to the aggregate (cf. Section 1.2), it becomes part of the unregistered pool of particles.

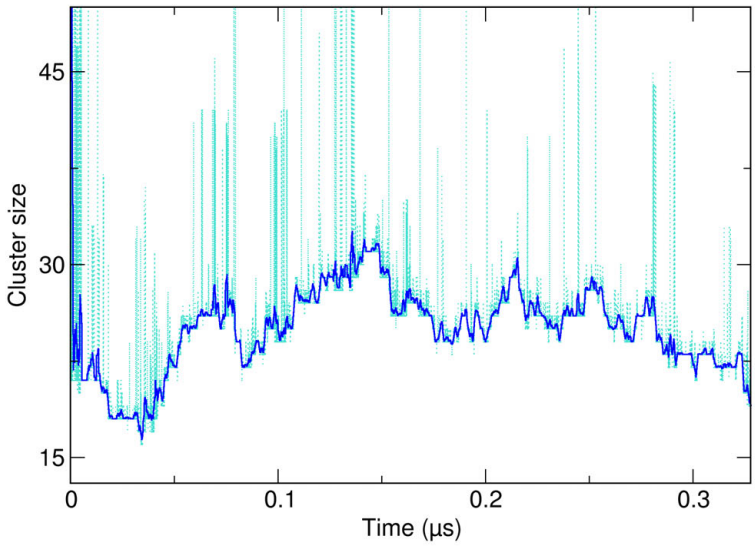

Figure 2.22: Temporal evolution of the size of a single DeTA micelle. The original data is depicted as a dotted **turquoise** line, overlaid by a 100-point moving average represented by a solid **blue** line.

1) The aggregate size is quasi-constant, fluctuating around the preferred aggregation number that represents a minimum in free energy.

2) When an exchange takes place, the probability of release is equal for all monomers in the micelle. This implies that either the positions in reference to the surrounding medium are equal for all monomers, i.e. there is no bulk phase but just an interfacial layer or that the change in positions inside the aggregate is of substantially higher frequency than the exchange rate.

The rationale behind point 1) is that swelling of aggregates will retard the emission of initial molecules as opposed to a theoretical aggregate of constant size, by enlarging the pool of particles, whereas disintegration may accelerate it depending on the mechanism of breakdown. Fulfillment of the first condition is approximated by averaging over a number of aggregates. As observed in the cluster evolution diagrams in Section 2.2, there are incidents of aggregates showing trends of overproportionate swelling or rapid disintegration, but for the most part the distinct maxima in the size distribution histograms demand that the aggregation number oscillates around a central value. As reviewed in Section 2.4, there is a definite ordering of the surfactant molecules, with all polar head groups and carbon chain links occupying certain radial positions. In other words, there is no bulk phase inside the micellar objects, so condition 2) is met as close as the dynamics in the system allow for.

Under this light, the release of a monomer can be reduced to a statistical urn problem. In the beginning, the urn is filled with black balls. Upon each draw, one white ball is

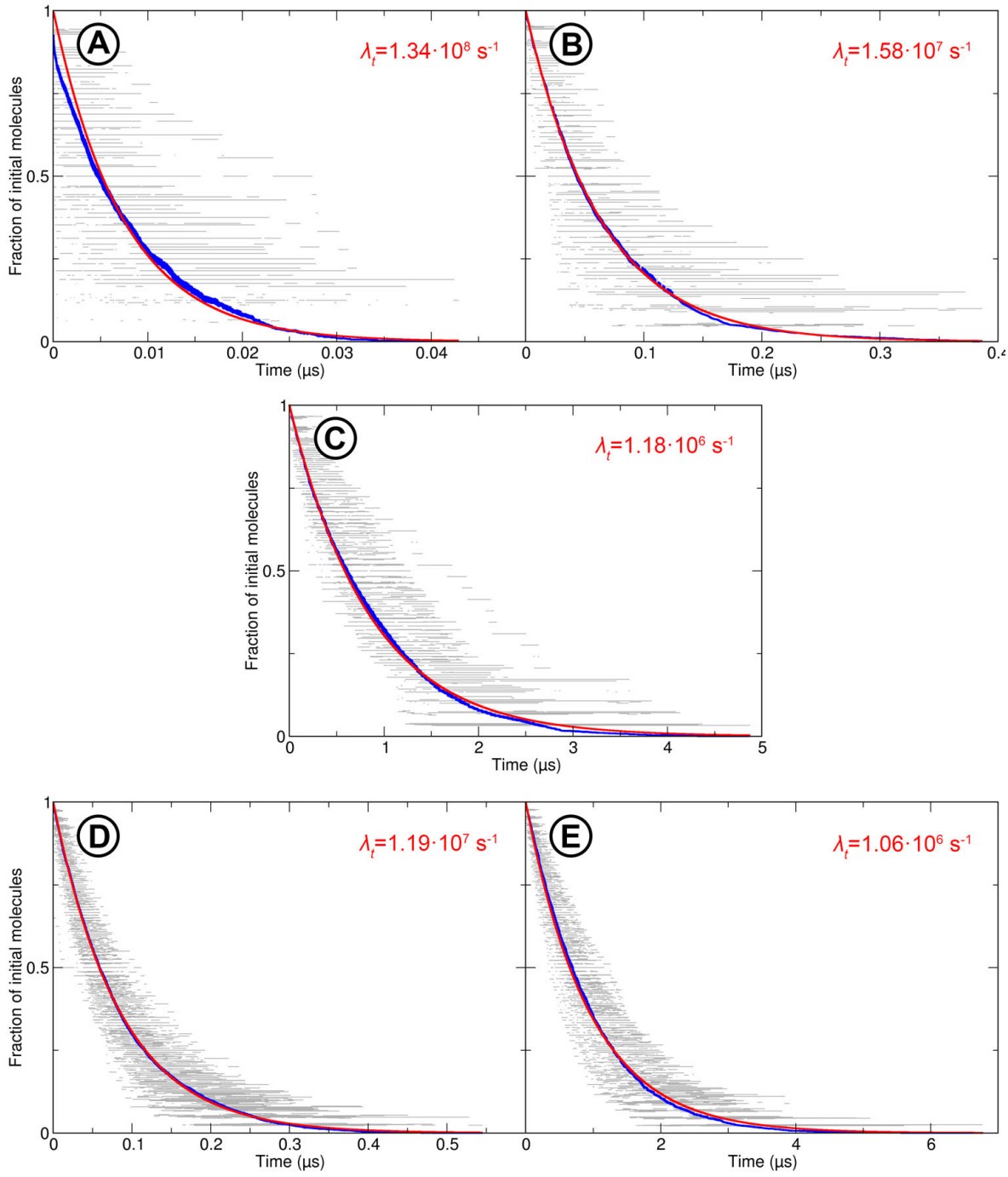

Figure 2.23: Degression of initial molecules over time in **A** OTA, **B** DeTA, **C** DTA, **D** CAP, and **E** DEC. Grey dots represent the data points obtained from 110 individual runs, **blue** lines trace a 1000 point moving average, and **red** lines show exponential fits of the type $[Y] = e^{-\lambda_t \cdot t}$. The associated decay constant is annotated in the respective diagram.

supplemented, so the total number of balls does not change. Here, black balls represent the initial molecules allocated to an aggregate at the beginning of the analysis. White balls represent any surfactant molecule that was not originally part of the micelle or has left it at any point. The statistical event of interest is the drawing of a black ball. In order to treat the problem mathematically rigorous, it is necessary to introduce concepts from probability theory.

For this purpose, let S denote the size of the set at the beginning. According to the premises, S then designates the initial number of black balls, as well as the system size. Probability spaces (Ω_i, P_i) for $i \in \{1,\dots,N\}$, $N \in \{1,\dots,S\}$ are now defined in the following way (interpretation of the mathematical objects will be given below):

- $\Omega_1 = \{1\}$ and the probability mass function is defined as $p_1(1) = 1$, which induces a probability measure P_1.
- If $N > 1$, it applies $\Omega_N = \{1\} \times \{0,1\}^{N-1}$ and for $\nu = (\nu_1,\dots,\nu_N)^T \in \Omega_N$ the probability mass function is defined by

$$p_N(\nu) = \begin{cases} \frac{S-\sum_{i=1}^{N-1}\nu_i}{S} p_{N-1}\left((\nu_1,\dots,\nu_{N-1})^T\right) & \text{if } \nu_N = 1, \\ \frac{\sum_{i=1}^{N-1}\nu_i}{S} p_{N-1}\left((\nu_1,\dots,\nu_{N-1})^T\right) & \text{if } \nu_N = 0. \end{cases} \tag{2.6}$$

  Since by this definition $p_i(\nu_1,\dots,\nu_{i-1},0) + p_i(\nu_1,\dots,\nu_{i-1},1) = p_{i-1}(\nu_1,\dots,\nu_{i-1})$ for all $i \in \{2,\dots,N\}$ and $p_1(1) = 1$, it follows that $\sum_{\nu\in\Omega_N} p_N(\nu) = 1$ and thus p_N really is a probability mass function. This again induces a probability measure P_N.

These definitions should be interpreted in the following manner: For $\nu \in \Omega_N$, an entry 1 in the i-th component means that a black ball was drawn at the i-th drawing, a 0 means that a white ball was drawn. Thus every vector in Ω_N needs to satisfy $\nu_1 = 1$ as there are only black balls in the beginning.

After i drawings, the probability to draw a black ball is equal to the number of all black balls left divided by the system size S. The number of remaining black balls is given by $S - \sum_{i=1}^{N-1}\nu_i$, since the 1-entries in ν denote drawings of black balls. Conversely, the probability of drawing a white ball is $1 - \frac{S-\sum_{i=1}^{N-1}\nu_i}{S} = \frac{\sum_{i=1}^{N-1}\nu_i}{S}$. In order to formulate the probability of the whole chain of drawings ν, it is necessary to trace a tree diagram up to level N, leading to p_N as proposed.

To give an example, let $\nu = (1,0,1)^T \in \Omega_3$. Then

$$p_3(\nu) = \frac{S-1}{S} p_2\left((1,0)^T\right) = \frac{S-1}{S}\frac{1}{S} p_1(1) = \frac{S-1}{S^2}. \tag{2.7}$$

The goal is to calculate the expected number of extracted black balls after N total drawings, where $N \in \{1,\dots,S\}$, thereby obtaining the number of attempts it takes to diminish the number of black balls to a given value. This information enables the relation of the number of monomer exchanges to the elapsed time by means of the above analysis.

To this end, a random variable is introduced, which counts how many black balls were drawn after N steps:

$$X_N : \Omega_N \to \{1,\ldots,N\}, v \mapsto \sum_{i=1}^{N} v_i \tag{2.8}$$

The quantity of interest is now the expected value of X_N, which is defined as

$$E[X_N] := \sum_{i=1}^{N} P_N(X_N = i)\, i, \tag{2.9}$$

where $P(X_N = i) := P(\{v \in \Omega_N X_N(v) = i\})$ for $i \in \{1,\ldots,N\}$. For practical purposes, it is convenient to use the equivalent representation

$$E[X_N] = \sum_{v \in \Omega_N} p_N(v) X_N(v). \tag{2.10}$$

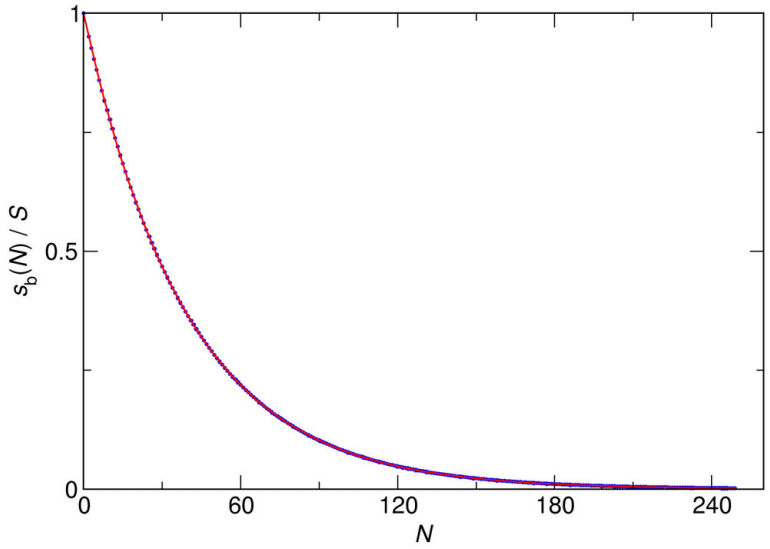

Figure 2.24: Fraction of black balls $s_b(N)/S$ remaining in an urn, from which a random ball is drawn and that is refilled with a white ball; evaluated after N repetitions for an originally fully black urn, according to Equations (2.6) and (2.10). **Blue** dots represent the computed data points and the **red** line the exponential function $s_b(N)/S = e^{-0.025318 \cdot N}$.

Whether the expression resulting from merging Equations (2.6) and (2.9)/(2.10) can be further simplified is beyond the scope of this work. In this context it is sufficient to find that the results of a numerical evaluation are perfectly described by an exponential decay as shown for $S = 40$ in Figure 2.24. An implementation of this model is found in Section 1.2. It should be noted that the restriction of N to $\{1,\ldots,S\}$ is merely applied to simplify the formalism. An extension of the model to an unlimited number of draws can

be achieved by introducing $\widetilde{\Omega}_N = \left\{ \nu \in \Omega_N \,\middle|\, \sum_{i=1}^{N} \nu_i \leqq S \right\}$. This generalization is also used in the numerical treatment.

The agreement of this model with the exponential decay of the number of initial molecules in all ionic micelles over time implies that the monomer exchange rate can be obtained as

$$k = \frac{\lambda_t}{\lambda_N}, \tag{2.11}$$

where λ_t is the decay constant in the time domain and λ_N is the decay constant in the exchange step domain of an exponential function of the form $f(x) = \mathrm{e}^{-\lambda \cdot x}$. More specifically, this rate constant corresponds to the expulsion constant k_- in the ANIANSSON and WALL treatment that starts from the assumption that association and dissociation of aggregates proceed as individual steps

$$\mathrm{A}_1 + \mathrm{A}_{m-1} \underset{k_m^-}{\overset{k_m^+}{\rightleftharpoons}} \mathrm{A}_m, \tag{2.12}$$

where A_s represents an aggregate consisting of m surfactant molecules.[192–195] An overview over the rate constants for the different surfactant species is given in Table 2.7.

Table 2.7: Dissociation constants k derived by means of Equation (2.11) by species and underlying exponential decay constants λ_t and λ_N derived from the statistical model and obtained from the fitting curves to the decay analysis, respectively.

Species	$\boldsymbol{k}$ (s^{-1})	$\boldsymbol{\lambda_t}$ (s^{-1})	$\boldsymbol{\lambda_N}$ (1)
OTA	$2.08 \cdot 10^{9}$	$1.34 \cdot 10^{8}$	$6.45 \cdot 10^{-2}$
DeTA	$3.07 \cdot 10^{8}$	$1.58 \cdot 10^{7}$	$5.13 \cdot 10^{-2}$
DTA	$3.26 \cdot 10^{7}$	$1.18 \cdot 10^{6}$	$3.64 \cdot 10^{-2}$
CAP	$4.69 \cdot 10^{8}$	$1.19 \cdot 10^{7}$	$2.53 \cdot 10^{-2}$
DEC	$4.63 \cdot 10^{7}$	$1.06 \cdot 10^{6}$	$2.30 \cdot 10^{-2}$

The results indicate that within a particular homologous series, the rate constants are significantly affected by the aliphatic chain length. From OTA over DeTA to DTA, k decreases by two orders of magnitude and the same tendency is evident for the anionic surfactants. Such a shift has also been reported by RASSING et al. for sodium n-alkyl sulfates and sulfonates in ultrasonic relaxation studies[196] and by HOFFMANN et al. for n-alkylpyridinium halides using pressure jump and shock tube techniques.[197]

The derived numeric values line up well with rate constants obtained from experiments involving surfactant molecules of similar dimensions. Application of ANIANSSON and WALL's theory to kinetic measurements yields rate constants of $k_- = 1.0 \cdot 10^{8}\,\mathrm{s}^{-1}$ for sodium

octyl sulfate[198] and $2.7 \cdot 10^7\,s^{-1}$ for dodecyltrimethylammonium iodide[199] at a temperature of 298 K. The first value is close to that determined for the anionic CAP and the second matches well that for DTA.

2.6 Summary

At the beginning of this chapter it was shown that the spontaneous formation of micelles from simple surfactant molecules can be thoroughly sampled in atomistic MD simulations, deploying latest technological standards. The most challenging input configurations to converge are systems initiating from a macroscopically phase separated state. This fact only became momentous in case of the longest-chained cationic surfactant sodium decanoate, were system relaxation of this simulation path was not achieved even after more than 15 μs of simulation time. Nevertheless, along the path starting from homogeneous dispersion of surfactant molecules in water, a state of constant distribution of aggregation numbers over numerous simultaneous micelles could be attained. The observed polydispersity is not in contradiction to general belief. Conviction of strict monodispersity at best circulated during the early years of micelle research, when instrumental precision could not resolve small differences in particle dimension,[94] but it was soon clear that the term rather signified a narrow distribution and the lack of multiple preferred aggregation numbers.[171,200] The same is true when discussing the shape, which is subject to sometimes severe fluctuations.[22]

This subject was elaborated in Section 2.3 and it was concluded none of the aggregates perfectly resembles a sphere. Deformations are, however, distributed within narrow margins around average values of fairly high sphericity. A gradation by species is evident, albeit weakly, in that aggregates of similar size are more eccentric when formed by the anionic surfactants than their cationic counterparts. Likewise, a shorter aliphatic chain is accompanied by higher eccentricity than a longer tail section. An additional analysis based on the convex hulls of the aggregates was presented in an attempt to further decompose shape deviations into contributions from ellipsoidal and concave deformations. Indeed, these were shown to occur to a certain extent independently and characterize deformations of the cationic micelles as more concave than those of the anionic aggregates.

A detailed study of the structure in Section 2.4 revealed significant water penetration into a diffuse interfacial region. Beyond that layer, a completely water-free core exists inside all investigated micelles, that occupies between 24 % and 40 % of the total volume* when locating the interface at the most probable position of polar head groups. This result was confirmed by an evaluation of the residual hydration which shows significant water contact for all sections of the hydrophobic tail. This is not entirely due to water penetration but partly originates from peculiarities in spatial assembly. At the examples of CAP and DeTA micelles it was deduced that tangential positioning of monomers is common, which exposes a significant fraction of the terminal alkyl units to the wet interfacial region. In case of DeTA micelles, this effect is more pronounced, since the surface is considerably rougher and features deep crevices between the radially outwards oriented head groups. An evaluation of the solvent accessible surface area of the aggregates further supports this notion. With restrictions in respect to the profoundly chaotic interior, both anionic and cationic aggregates share similarities with the "Menger" micelle,[29] that features an uneven surface with water-filled pockets and a hydrophobic core encompassing only a fraction of the micelle volume. Those water molecules close to this surface are characterized by the formation of significantly less water-water hydrogen bonds than in the bulk. This effect is more pronounced for the anionic surfactant species that possess a dedicated hydrogen-bonding site, but still significant for the cationic species.

Ultimately, the monomer exchange frequency was determined from the decrease of labeled molecules in micelles in conjunction with a probabilistic description of the process. The determined values for the rate constant are on the order of $10^7 - 10^9\,s^{-1}$, which agrees well with documented results.

*It should be clarified that this is a very conservative estimate since only spherical hydrophobic volumes were considered.

2.A Principal moments of inertia

Figure 2.25 shows distributions of the principal moments of inertia for N_{agg}^{0} of all investigated micelles.

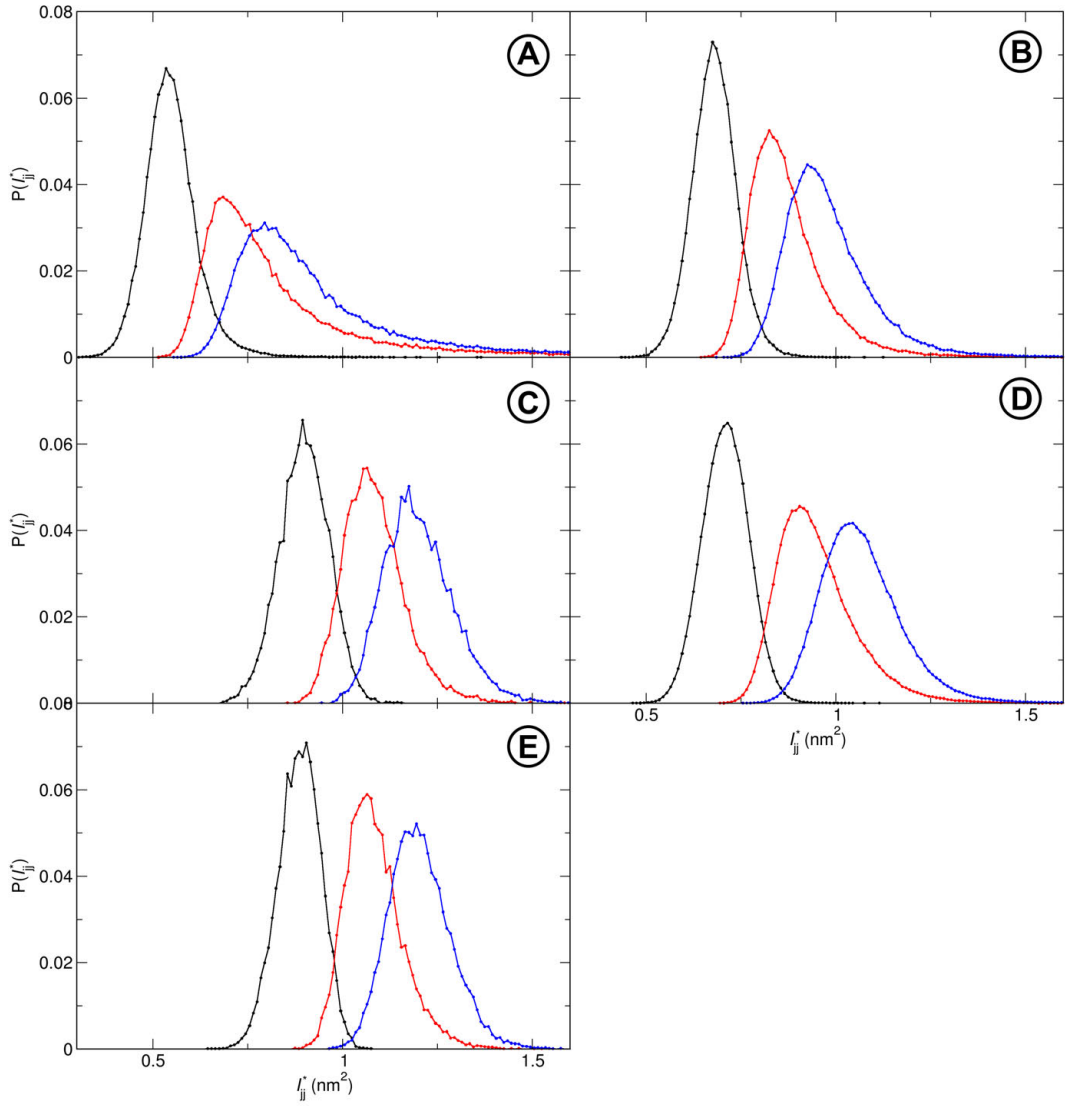

Figure 2.25: Histograms of the mass independent principal moments of inertia I_{xx}^{*} (**black**), I_{yy}^{*} (**red**), and I_{zz}^{*} (**blue**) for **A** OTA, **B** DeTA, **C** DTA, **D** CAP, and **E** DEC. Due to the set size tolerance, the micelle mass can vary. Therefore, the actual moments of inertia I_{jj} are divided by the current mass in each analysis step to yield the mass independent quantity I_{jj}^{*}.

2.B Decomposition of DTA and CAP micelles

Decomposition of a DTA micelle Figure 2.26 shows the distributions of methyl, methylene and head groups around the geometric center of DTA aggregates. Comparable to DeTA micelles (cf. Section 2.4), an inflection point is observed in the graphs for sites C1, C2, and C3. This suggests a geometrical subdivision that can be resolved by isolating the set of molecules that comes closer than a certain cutoff distance to the COG and the respective complement. Renderings of the complete micelle and the two separated fractions are depicted in Figure 2.27.

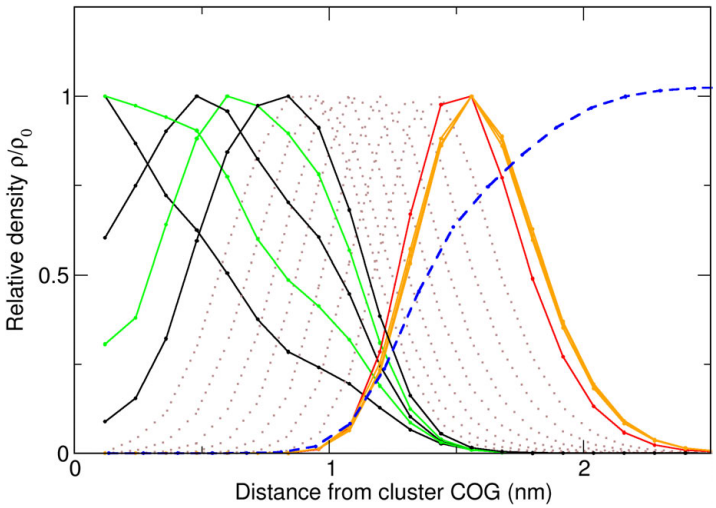

Figure 2.26: Radial distributions of alkyl tail units and head groups around the geometric center of DTA micelles. The first five carbon chain links (C1–C5) are shown in alternating **black** and **green**. For reasons of clarity, the succeeding aliphatic units are merely hinted as dotted **brown** lines. The head group density is split into nitrogen (**red**) and methyl (**orange**) contributions. For reference, the relative water concentration is supplemented in form of a dashed **blue** line.

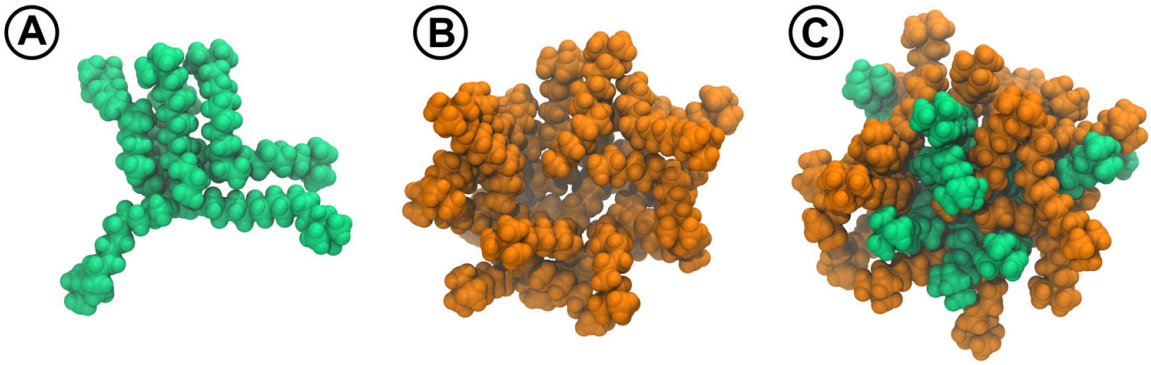

Figure 2.27: Snapshots of molecules constituting a DTA micelle with **A** any atom or **B** no atom situated inside a sphere of radius 0.7 nm around the COG. **C** shows the whole aggregate assembled from **A** and **B**, retaining the coloring of the separated illustrations.

Decomposition of a CAP micelle In contrast to DTA and DeTA aggregates, no inflection point occurs in the density distributions of methyl and methylene groups in CAP micelles. However, two distinct groups of surfactant molecules can be identified by means of radial alignment as demonstrated in Section 2.4. For lack of a meaningful radial cutoff, the value of 0.5 nm is adopted from the DeTA analysis. The resulting decomposition is visualized in Figure 2.28.

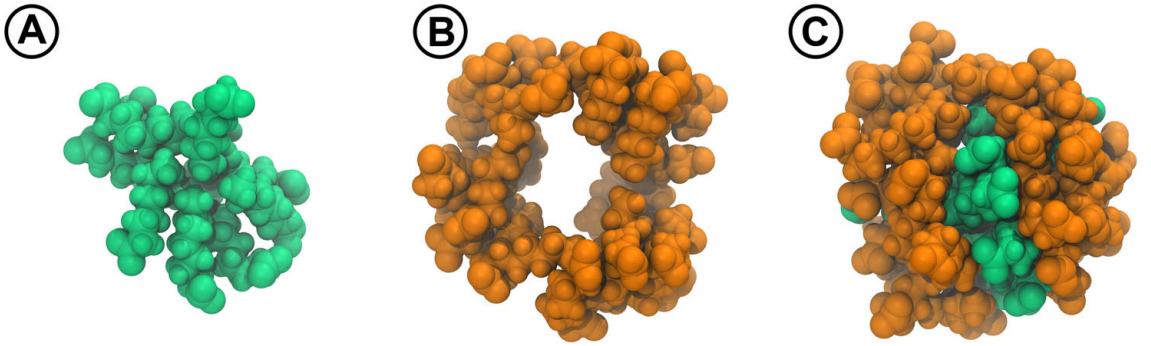

Figure 2.28: Snapshots of molecules constituting a CAP micelle with **A** any atom or **B** no atom situated inside a sphere of radius 0.5 nm around the COG. **C** shows the whole aggregate assembled from **A** and **B**, retaining the coloring of the separated illustrations.

chapter **three**

Surfactant-free microemulsion in water/ethanol/octanol

3.1 Overview

This chapter covers the topic of surfactant free microemulsions in the ternary system water/ethanol/octanol.

The first segment gives an account of the oil-in-water micelles emerging in water-rich mixtures. The choice of composition is rationalized in Section 3.2.1 and the relaxation process is followed. In Section 3.2.2, the radial structure is disclosed and the role of the hydrotrope ethanol in stabilizing the micellar aggregates is studied. Subsequently, several consistent definitions of the aggregate interface are determined in Section 3.2.3. Analogous to the procedure pursued for classical surfactant micelles, the degree of size fluctuations is estimated and the dynamic properties are portrayed in Section 3.2.4. Moreover, a classification of the octanol micelles by means of their lifetimes is delineated. Section 3.2.5 deals with the sphericity of the aggregates and contextualizes the results with the priorly assessed interplay of octanol and hydrotrope in the assembly, as well as longevity of the structures.

The solubilization properties of the SFME are addressed in Section 3.2.6 by means of two model solutes: a large organic compound that is of similar dimensions as the micelles, and a single propane molecule. Moderate quantities of the former allow for a detailed examination of rearrangements in the nano-ordering. Conversely, the small hydrocarbon is expected to generate little perturbance in the system, which enables the computation of the location dependent solvation free energy in and around the octanol domains.

In the last subpoint, Section 3.2.7, the effects of added electrolytes are discussed and itemized into individual responses of the system components.

Section 3.3 describes the transition to other distinct morphologies occurring in the one-phase region close to the decomposition line upon advancing towards compositions

of excess octanol. This comprehensive record is then aligned with experimental results by means of measured and calculated small and wide angle X-ray intensities.

In a brief outlook, the ternary system water/propanol/octanol is discussed. The mutual miscibility of these three components predicts ouzo-like behavior, that is directly compared to the pre-Ouzo model system.

3.2 Direct oil-in-water microemulsion: the pre-Ouzo effect

3.2.1 Incidence

Introductory remark: *This section is part of a brief recapitulation of Ref. 116 and the related publication in Ref. 114. All discussions in this chapter build upon the to date not generally known pre-Ouzo effect. In the author's view, this preliminary summary is mandatory to embed the subsequent studies into a comprehensible framework. Moreover, many considerations in later sections are interwoven with the results presented here. Those would otherwise need to be introduced out of context and clarified in retrospect, which would severely compromise coherency. For the same reason, the original analyses were revised and/or extended.*

Numerous compositions in the water-rich region of the phase diagram were sampled along a dilution line of constant octanol mole fraction. The results are discussed here by means of the three model compositions marked in the ternary phase diagram in Figure 3.1. Since one composition is situated in the (experimental) two-phase region and another deep within the monophasic section of the phase diagram, microemulsion-like ordering of octanol molecules is not apriori expected for all systems. Rather, the extreme cases serve

as reference to a) put in perspective the peculiarities observed for composition II and b) validate the operational capacity of the methodology for this application.

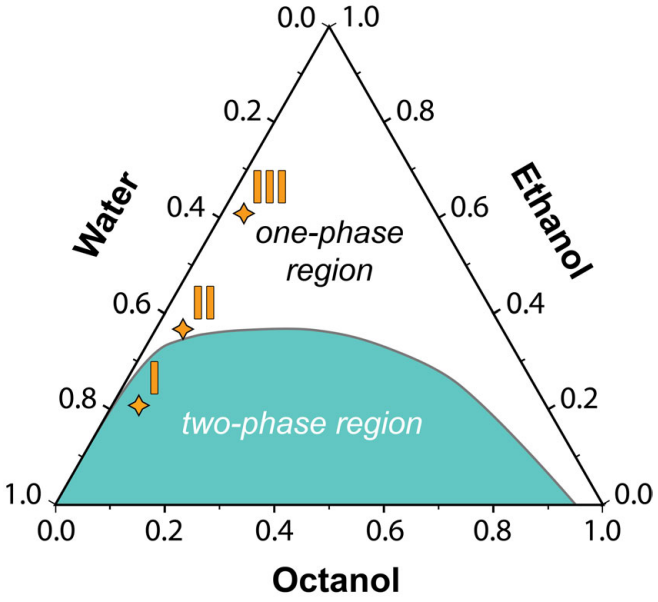

Figure 3.1: Ternary phase diagram of water/ethanol/octanol with **orange** star shapes signifying the investigated compositions. Values are given in weight fraction.*

In analogy to Chapter 2, the starting point is the quantification of aggregate formation. To this end, Figure 3.2 shows the probability for an octanol molecule to be part of a cluster of size N_{agg}, $\mathrm{P}'\left(N_{\mathrm{agg}}\right)$, in compositions I, II, and III. The histogram for I exhibits a pronounced peak at around 220 molecules, which is almost equal to the total number of molecules in the system. Only few monomers are present and no intermediate clusters are detected. The formation of a single cluster comprising almost all octanol molecules is equivalent to macroscopic phase separation, which is unsurprising given the system is well within the two-phase region. Conversely, the distribution for III indicates numerous monomers and small clusters, but none bigger than 20 molecules. A logarithmic plot of the probability to find a cluster of size N_{agg}, $\mathrm{P}\left(N_{\mathrm{agg}}\right)$, (inset) reveals that the distribution is well described by an exponential decay with decay constant -0.8. It is the consequence of subsequent size independent association equilibria occurring in molecular solution of octanol.

The results for composition II show a different picture. Although the mixture is also in the one-phase region of the phase diagram, the graph declines much slower than III and even large aggregates of around 100 molecules occur frequently. As the running total shows, more than half the octanol molecules in the system are part of clus-

*Shape and location of the one- and two-phase region reconstructed from **Figure 1. a)** in Ref. 101.

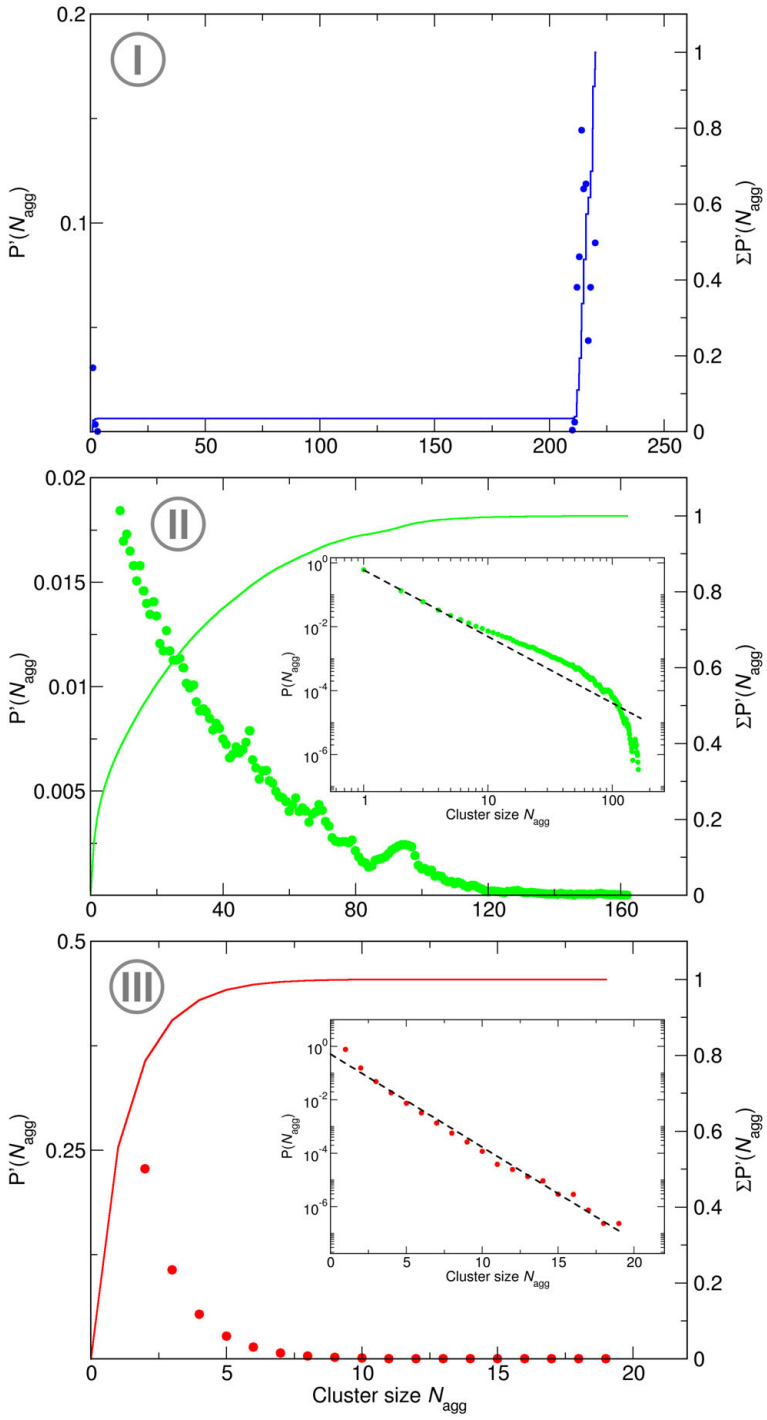

Figure 3.2: Probabilities of an octanol molecule to be part of an aggregate of size N_{agg} $P'(N_{agg})$ in composition I, II, and III shown as dots. Lines represent the running total of the respective probability $\sum P'(N_{agg})$. Insets show the size distributions $P(N_{agg})$ of octanol clusters. The dashed line in the inset diagram in II traces the power-law function $P(N_{agg}) = 0.6 \cdot N_{agg}^{-2.1}$, that in the inset of III the exponential function $P(N_{agg}) = 0.5 \cdot e^{-0.8 N_{agg}}$.

ters with aggregation numbers greater than 16. The highest determined aggregation number in rare instances of ~ 160 is still far from the overall number of 224 molecules, so the characteristics are not an artifact of the finite system size. Furthermore, a log-log plot of $\mathrm{P}\left(N_{\mathrm{agg}}\right)$ (inset) clarifies that the distribution exhibits a broad maximum between aggregation numbers 10 and 110. This feature is augmented on a power-law distribution with exponent -2.1 and therefore is not the result of fluctuations close to a critical point.[201]

To give a visual impression of the structures, a snapshot of the octanol pseudo-phase in composition II is displayed in Figure 3.3 next to the cases of phase separation in I and molecular solution in III. Slices through the supplemented surface representations of individual components show equally hard transitions from aqueous to polar domains in II and I, indicating two separate pseudo-phases within the monophasic region. To a much lesser degree, pockets of high octanol density also show up in the ethanol phase as blurry outlines of gradually decreasing ethanol concentration towards the centers.

The polydispersity observed in the histogram of II raises the question as to whether full convergence of the system has been achieved, particularly since typical aggregation numbers and the time scale of equilibration are not known for this mixture. A measure of the convergence is given by the type of colormap plot already discussed in Section 2.2 (cf. Figure 3.4). For the sake of completeness, plots for all three considered systems are depicted. The graphs for I and III converge instantly on this time scale to uniformly reflect the situation depicted in the histograms in Figure 3.2. The graph for II, which will be referred to as composition α from this point on, however, features strong fluctuations that represent swelling and depletion of aggregates. These processes occur repeatedly for varying cluster sizes and no singular features are visible, nor is an overall trend. On occasion, individual events can be traced for intervals of approximately 10^2 ns, but in the scope of a total simulation time of several microseconds are well averaged out during analysis.

Due to the broad distribution of preferred aggregation numbers, the analyses in this chapter are performed for several distinct cluster sizes. Unless otherwise noted, a 15 % size tolerance is set.

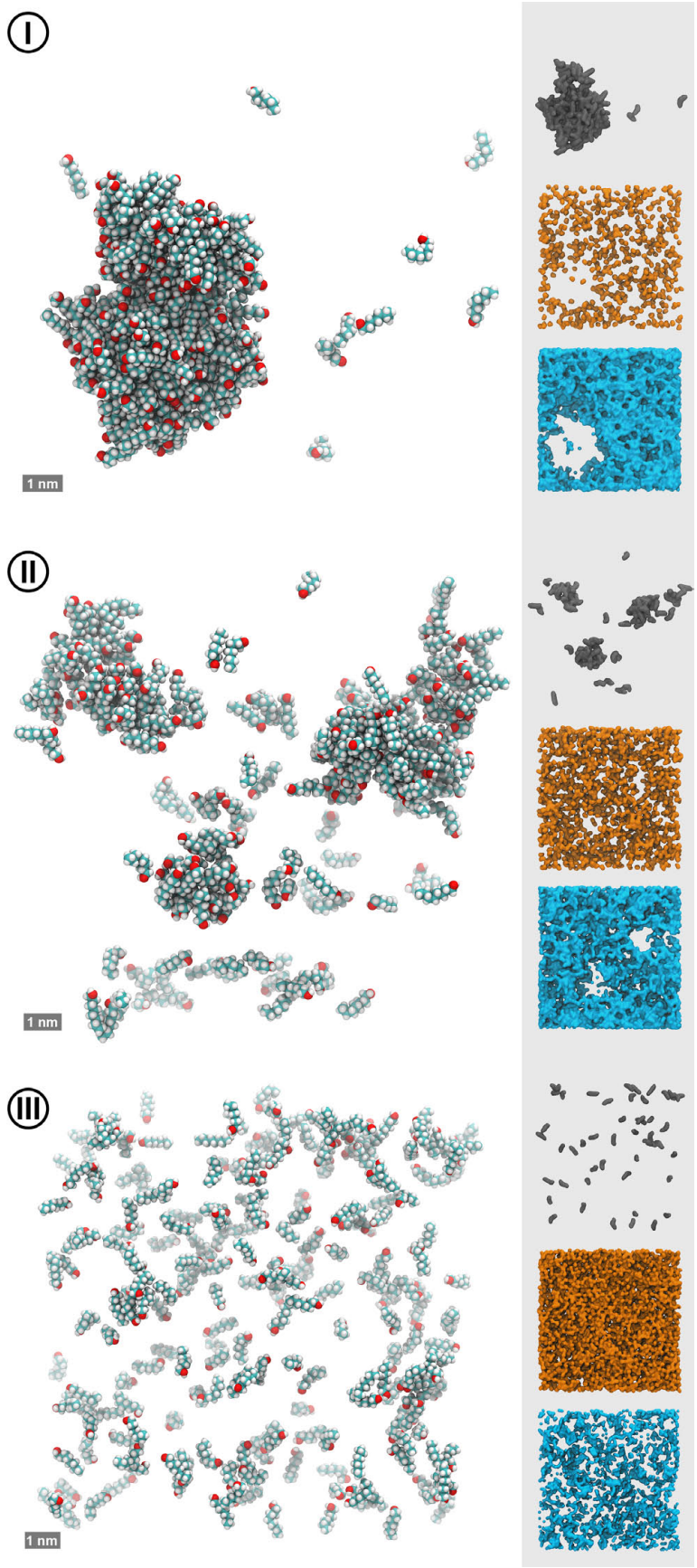

Figure 3.3: Snapshots of octanol in compositions I-III in van der Waals representation. To the right of each rendering, separate surface representations of 2 nm deep slices through the simulation box are depicted for every component in the following color coding: **octanol**, **ethanol**, **water**.

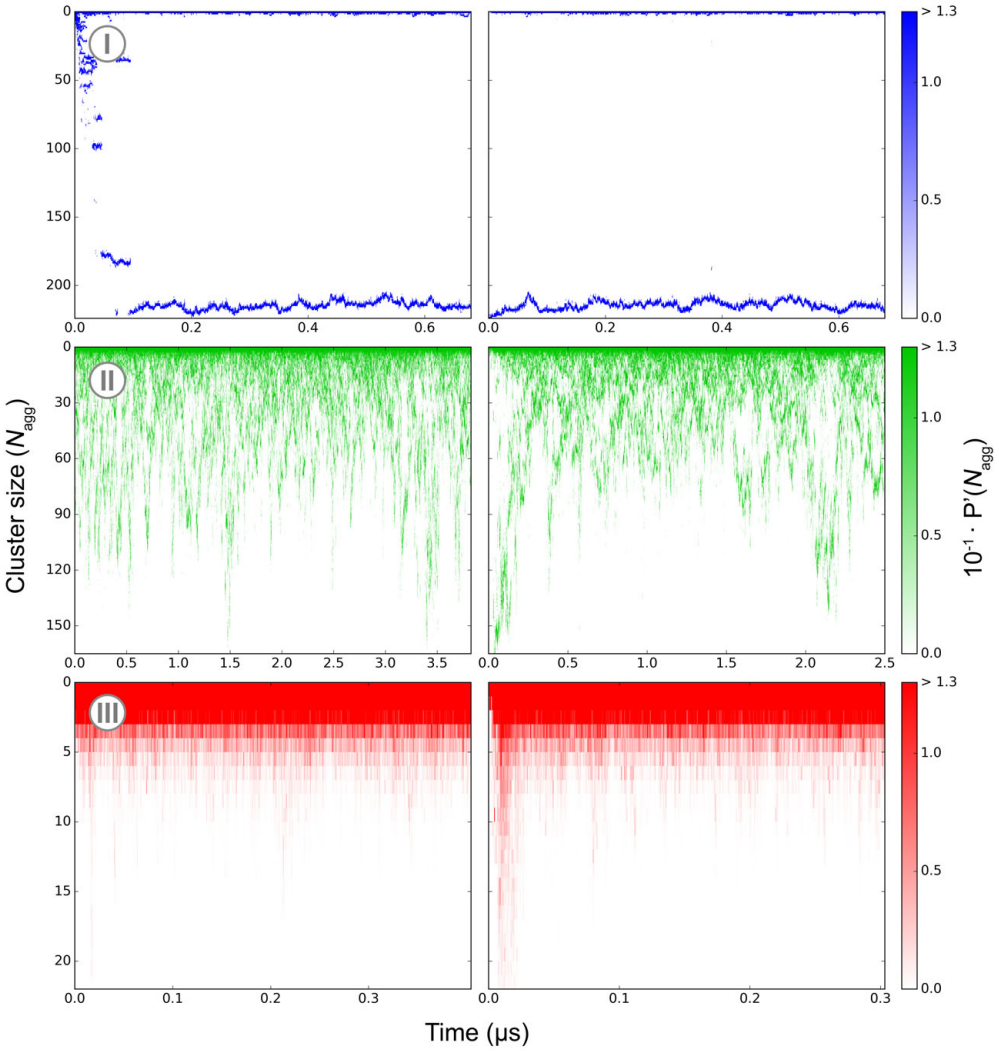

Figure 3.4: Colormap plots of the temporal evolution of octanol cluster size distributions in compositions I, II, and III starting from homogeneous distribution of the system components (left column) and a single droplet of octanol in molecular mixture of water and ethanol (right column). The color grading denotes the probability for an octanol molecule to be part of an aggregate of size N_{agg} $P'(N_{agg})$ with respect to the provided color bars.

3.2.2 Structure of the aggregates

Introductory remark: *This section is part of a brief recapitulation of Ref. 116 and the related publication in Ref. 114. All discussions in this chapter build upon the to date not generally known pre-Ouzo effect. In the author's view, this preliminary summary is mandatory to embed the subsequent studies into a comprehensible framework. Moreover, many considerations in later sections are interwoven with the results presented here. Those would otherwise need to be introduced out of context and clarified in retrospect, which would severely compromise coherency. For the same reason, the original analyses were revised and/or extended.*

In the previous section, the existence of octanol aggregates in the pre-Ouzo region of water/ethanol/octanol has been established, but in order to draw more detailed conclusions about this phenomenon and parallels to classical micelles, it is necessary to determine the structure of these objects. Like in the case of ionic micelles in Chapter 2, analyses are performed assuming on average spherical shape of the octanol aggregates. Along these lines, the local densities of the system components relative to the center of geometry of the clusters are obtained as one-dimensional functions. The results are presented in Figure 3.5 for aggregation numbers 22, 40, and 55. Clusters of larger size are excluded from the analysis for reasons addressed in Section 3.2.5.

Naturally, octanol concentration is highest close to the centers of the aggregates and decays with increasing distance. Similar to the surfactant micelles, there is a mild intermediate dip in density that signifies a depletion zone around the aggregates due to natural characteristic spacing. The principal peak equates to $c_{0,\mathrm{oct}} = 5.3\,\mathrm{mol\,l^{-1}}$ and $4.3\,\mathrm{mol\,l^{-1}}$ for clusters of size 22 and 55, respectively. Inverse behavior is observed for the water density, rising from almost zero to its bulk value ($c_{\mathrm{bulk,water}} = 40.8\,\mathrm{mol\,l^{-1}}$). With increasing cluster size, more and more water is detected in the aggregate center, rising from $c_{0,\mathrm{water}} = 0.9\,\mathrm{mol\,l^{-1}}$ for $N_{\mathrm{agg}} = 22$ to $5.2\,\mathrm{mol\,l^{-1}}$ for the largest considered structure. The solubility of water in pure octanol is $2.4\,\mathrm{mol\,l^{-1}}$,[202] which is more than twice the amount inside the smallest aggregates, suggesting a prevailingly apolar environment in the micelle core. This argument is strengthened by the presence of considerable amounts of ethanol close to the center that should actually facilitate penetration by water. With increasing aggregation number, the concentration of core ethanol increases from $c_{0,\mathrm{eth}} = 1.6\,\mathrm{mol\,l^{-1}}$ to $3.9\,\mathrm{mol\,l^{-1}}$.

A striking feature of the ethanol graph is the maximum close to the supposed aggregate surface. It is most pronounced for small aggregation numbers, where in case of $N_{\mathrm{agg}} = 22$ it exceeds the bulk density $c_{\mathrm{bulk,eth}} = 7.6\,\mathrm{mol\,l^{-1}}$ by 8 %. This accumulation is best studied by an initial examination of the interaction of ethanol with octanol. Histograms of the van

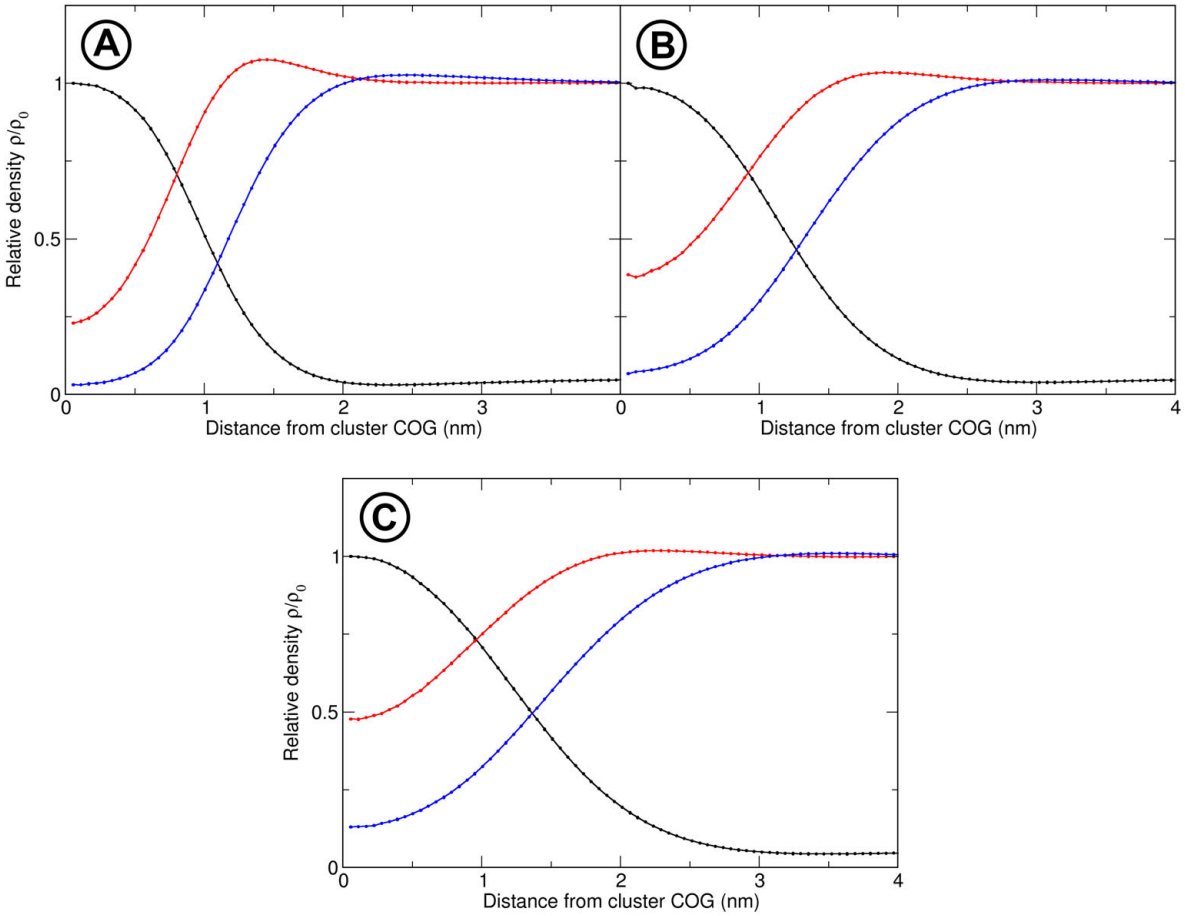

Figure 3.5: Radial distribution of the system components around the COG of aggregates of size **A** 22, **B** 40, and **C** 55 molecules. The **black** line corresponds to octanol, **blue** to water, and **red** to ethanol.

der Waals and Coulomb interaction energies of ethanol with octanol are shown in Figure 3.6.

The maxima at higher interaction energies indicate that, in addition to a non-interacting majority responsible for the large peaks at zero, a second population of "bound" ethanol can be identified in each case and isolated via a cutoff criterion. This separation reveals that in total 18.9 % of ethanol molecules are involved in van der Waals interaction with octanol and energies stronger than $-1.6\,\mathrm{kJ\,mol^{-1}}$ and 1.3 % in Coulomb interaction with energies stronger than $-11.0\,\mathrm{kJ\,mol^{-1}}$. Of the latter, 73.1 % also belong to the van der Waals group. This decisively exposes van der Waals interaction as the primary type of interaction between ethanol and octanol. If the concentration of ethanol around the aggregate COG is split into two contributions by means of this interaction criterion, the graphs in Figure 3.7 are obtained.

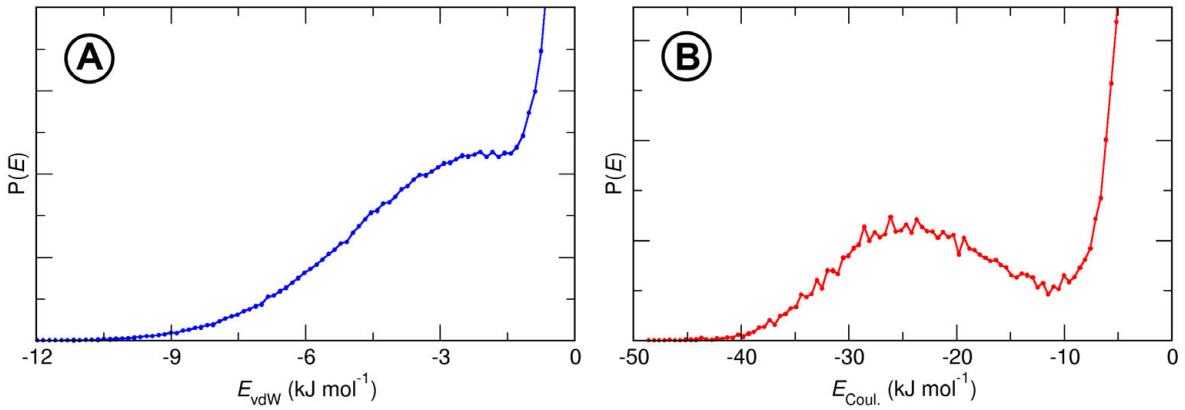

Figure 3.6: Histogram of **A** van der Waals interactions E_{vdW} and **B** Coulomb interactions $E_{Coul.}$ of ethanol molecules with octanol.

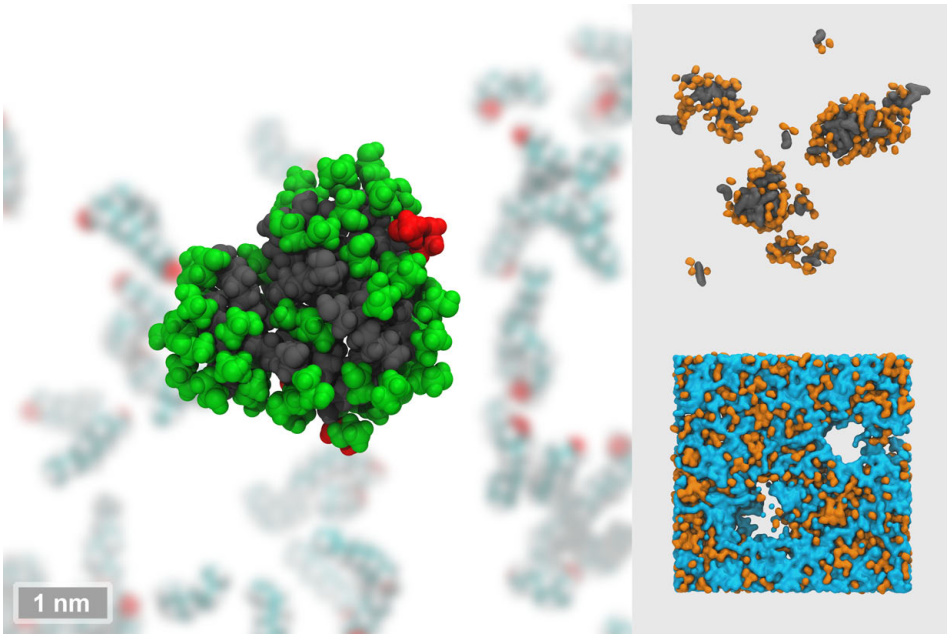

Figure 3.8: Rendering of an octanol aggregate of $N_{agg} = 22$, displayed in **grey**. Ethanol molecules bound to the aggregate in terms of van der Waals interaction stronger than $E_{vdW} = -1.6$ kJ mol^{-1} are colored **green**, those with Coulomb interaction $E_{Coul.} < -11.0$ kJ mol^{-1} are colored **red**. The pane to the right contains separate surface representations of the polar and apolar pseudo-phases as classified by this interaction energy criterion by means of 2 nm deep slices through the simulation box in the following color coding: **octanol**, **ethanol**, **water**.

All ethanol found inside the aggregates is part of the bound fraction, while noninteracting ethanol is present only in the water pseudo-phase. It can therefore complementarily be referred to as “unbound”. The peak in ethanol concentration observed earlier is clearly the

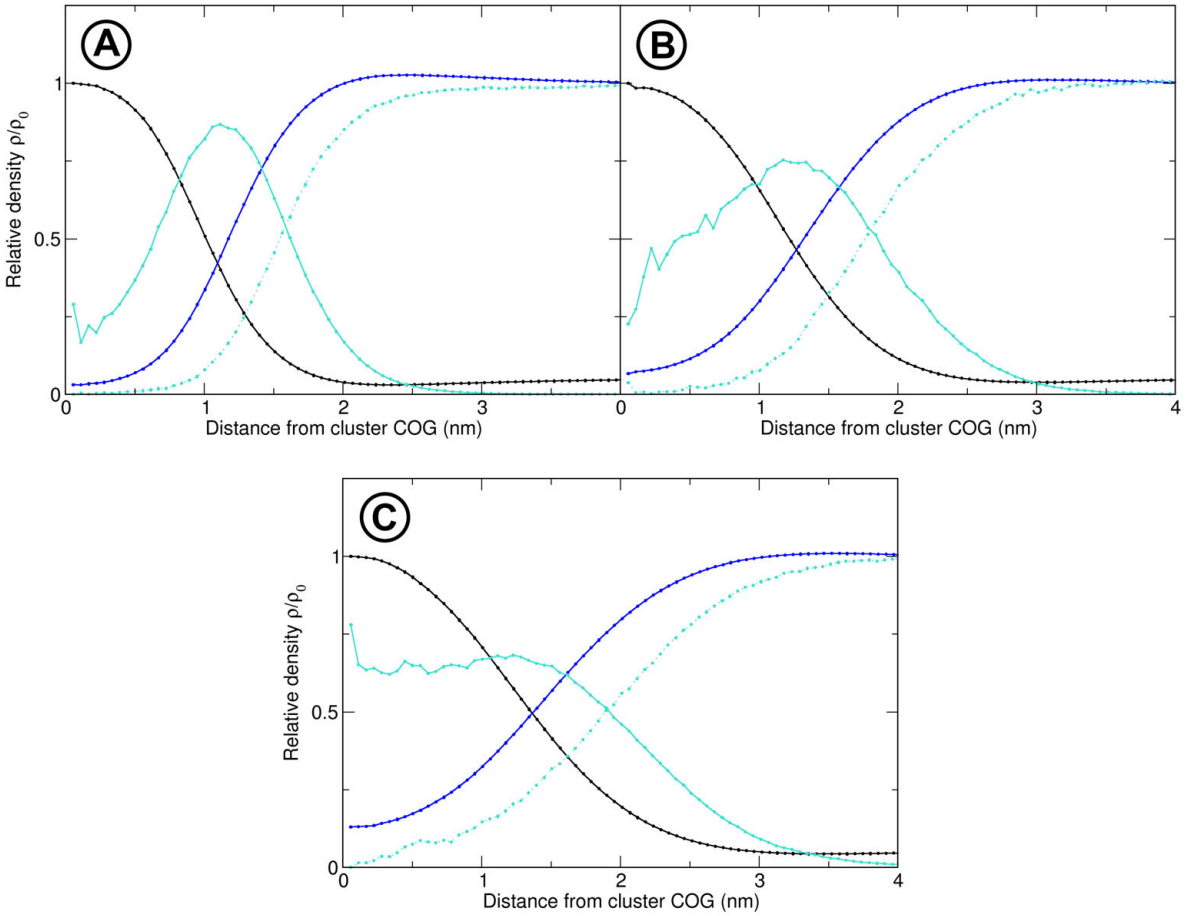

Figure 3.7: Radial distribution of the system components around the COG of aggregates of size **A** 22, **B** 40, and **C** 55 molecules with separated curves for interacting and noninteracting ethanol. The **black** line corresponds to octanol and the **blue** line to water. The solid **turquoise** line represents bound ethanol, the dotted line unbound ethanol.

consequence of an accumulation of bound ethanol forming an interfacial layer analogous to the ordering of surfactants in classical micelles. These micellar structures are consequently well characterized as “ethanol swollen micelles”. A visualization of the partitioning into polar and apolar pseudo-phases is presented in Figure 3.8.

Isolated octanol aggregates are coated in and partially penetrated by strongly interacting ethanol molecules. A homogeneous mixture of water and unbound ethanol constitutes the apolar pseudo-phase that encloses these structures. The micellar aggregates show up as sharply outlined pockets in the aqueous pseudo-phase, indicating a distinct separation of the two domains.

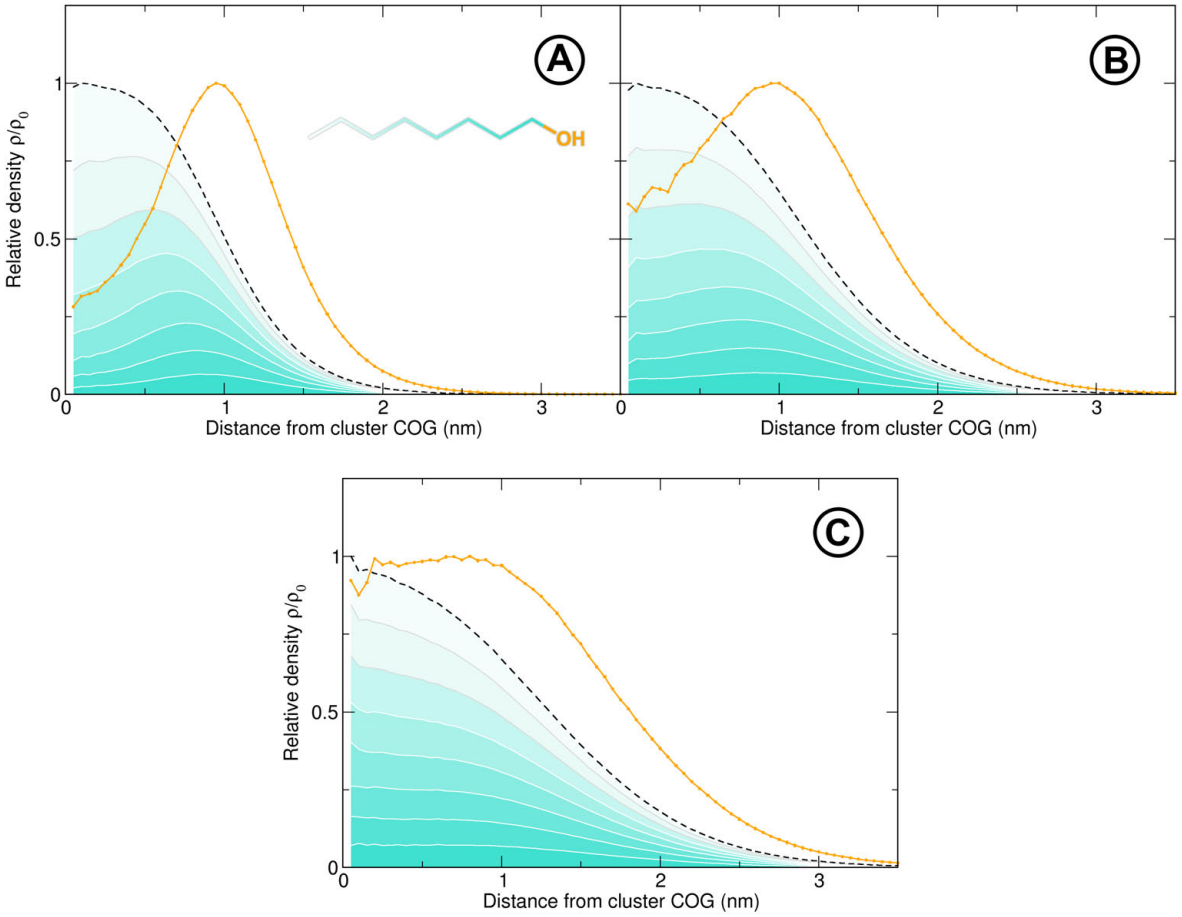

Figure 3.9: Densities of octanol hydroxyl and individual hydrocarbon carbon groups that constitute the aggregates around the geometric centers of clusters of size **A** 22, **B** 40, and **C** 55. The dashed **black** line traces the density of the entire aliphatic tail section. The enclosed area is partitioned into contributions from methyl and methylene units in terms of the color legend overlaid on the structure formula supplied in **A**. Hydroxyl group density is represented by a solid **orange** line.

The internal structure of the octanol droplets is illustrated by means of an evaluation of octanol hydroxyl group and carbon chain unit densities around the cluster centers in Figure 3.9. Overall, the distributions resemble those of the ionic micelles discussed in Section 2.4, albeit significantly more blurred. In any case, the head groups are predominantly oriented towards the polar phase, yet a significant number is present in the center, too. The sharpness of the hydroxyl peak lessens with increasing aggregation number and more and more head groups are found in the center. In the same manner, preferred radial positions of the individual carbon sites, that can be discerned in the spectrum for $N_{\mathrm{agg}} = 22$ in terms of staggered density maxima, are successively dissolved. In case of $N_{\mathrm{agg}} = 55$, at least the first four methyl and methylene groups provide almost equal contributions at all

radial positions. A plausible explanation for this apparent loss of order is a decreasingly spherical shape of larger aggregates – and thus an ineptitude of this type of analysis for these structures – that will be closer studied in Section 3.2.5. This rationale also agrees with the noted amplification of ethanol and water signals inside the larger micelles.

3.2.3 Definitions of the interface

Introductory remark: *This topic is part of the publication in Ref. 203.*

The precise definition of an interface is essential for thermodynamic characterization of systems with a phase boundary.[204] Surface excess and derived properties like quantitative adsorption are sensible to the location of the interface,[205] as is the equation of state needed to predict phase diagrams.[206] However, a universal criterion to assess its location is absent. A common consensus for vapor/liquid interfaces is the Gibbs dividing surface (GDS), which constitutes the interfacial plane with zero liquid surface excess.[207] Alternative definitions like the inflection point of the density profile or the location where density is equivalent to half the bulk value usually correspond to the GDS in this field of application, where the density profiles are symmetrical. These can also be applied to liquid/liquid interfaces, in which case partial densities of the two phases are considered.[208]

Another approach is to define the interface as the point where the normalized partial densities are equal. Consistency is only given, though, if the density profiles are symmetrical, which is not necessarily true. Further, a criterion based on density profiles need not coincide with the neutral plane of bending, which leads to diverging definitions.[209] Therefore, the suitability of a definition depends strongly on the structures present. Unambiguous definitions of the interface have been proposed for micellar solutions of ionic,[210] nonionic,[211] as well as oil soluble surfactants.[212]

The structural analyses of pre-Ouzo aggregates in Section 3.2.2 set the cornerstone for a variety of criteria to locate the nonpolar/polar interface. Three commonly employed criteria can directly be applied to the radial distributions of the system components around the aggregate center (cf. Figure 3.5): the point where octanol and water densities cross, the radius at which octanol density decays to 0.5, and the inflection point of solvent concentration. Similarly to a plane of fixed charge, that is used for systems containing charged surfactants[213] whose location is naturally close to the interface, the maximum in the distribution of bound ethanol (cf. Figure 3.7) can be determined as the interface. Likewise, the peak in the polar octanol head group density (cf. Figure 3.9) can be regarded as the boundary. Table 3.1 summarizes the determined aggregate radii based on the listed definitions.

By comparison, only the last two criteria yield discordant results. Both occur at approximately equal distances from the cluster COG, that do not systematically correlate with aggregation number. According to these criteria, aggregates of size 40 are of virtually the

Table 3.1: Radii of clusters with aggregation numbers 22, 40, and 55 as obtained by different estimates of the interface: the point r_c where the normalized water and octanol densities cross, the point r_d where octanol density decays to 0.5, the inflection point r_i of water density, the maximum in the radial distribution of octanol hydroxyl groups r_{ox}, and the most probable location r_{bound} of bound ethanol.

Criterion	Aggregation number		
	22	40	55
	(molecules)		
r_c (nm)	1.10	1.27	1.36
r_d (nm)	1.06	1.23	1.40
r_i (nm)	1.15	1.37	1.43
r_{ox} (nm)	0.95	1.01	0.89
r_{bound} (nm)	0.96	1.00	0.85

same dimensions as size 22 aggregates. For the largest aggregate, even a backwards shift to smaller radii is observed. This behavior is not surprising, considering that increasing amounts of both hydroxyl groups and ethanol are present close to the micelle center, as assessed in Section 3.2.2, relocating the respective maxima to smaller radii. Therefore, r_{ox} as well as r_{bound} do not represent meaningful distances with respect to the aggregate dimension.

The first three criteria, however, give a consistent definition of the interfacial plane. The determined values agree well for all aggregation numbers and show a coherent shift towards larger radii with growing cluster size, which reflects the increase in volume needed to accommodate more particles.

3.2.4 Dynamic properties

In Section 2.5, the monomer exchange frequency in micelles formed by ionic surfactants was derived based on the decline of molecules that were part of the aggregates at onset of the analysis over time. As was shown, the decrease obeyed an exponential decay law.

The same procedure is applicable in the pre-Ouzo case, but as the exponential curve fits to the average decay graphs for aggregates of size 22, 40,and 50 in Figure 3.10 indicate, the behavior is less ideal. An important factor contributing to these deviations is the lack of an unequivocal preferred aggregation number. This is accompanied by severe fluctuations of cluster sizes as shown in Figure 3.11. To stress this point, the diagram is supplemented by an analogous plot for CAP micelles.

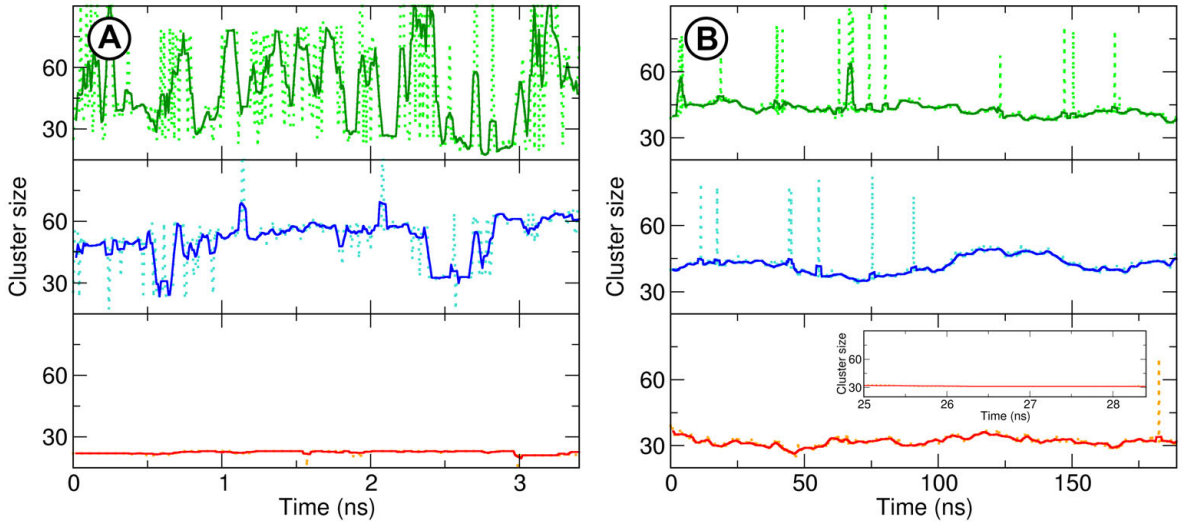

Figure 3.11: Size fluctuations in **A** octanol aggregates comprising 22 molecules and **B** CAP micelles of size N_{agg}^{0}. Solid lines represent moving averages over 20 points, dotted lines the actual trace of the micelles. The **green** graph shows the most severe, the **blue** graph the average, and the **red** graph the smallest fluctuations captured as evaluated by the total sum of stepwise differences of the moving average. In order to resolve characteristic fluctuation properties of the systems, substantially different time scales were chosen for **A** and **B**. Since this may create the false impression, that the curve shape of the graph of least fluctuations is more uniform in the pre-Ouzo case than in the case of CAP, an inset in the last graph in **B** shows a curve segment on the same time scale as used in **A**.

The three graphs represent the minimum, average and maximum intensity of size fluctuations of aggregates of initial size $N_{agg} = 22$ as measured by the total sum of stepwise differences. This evaluation was performed on the moving average of length five rather than the actual data to smoothen out artifacts introduced by isolated short-term collisions of clusters.

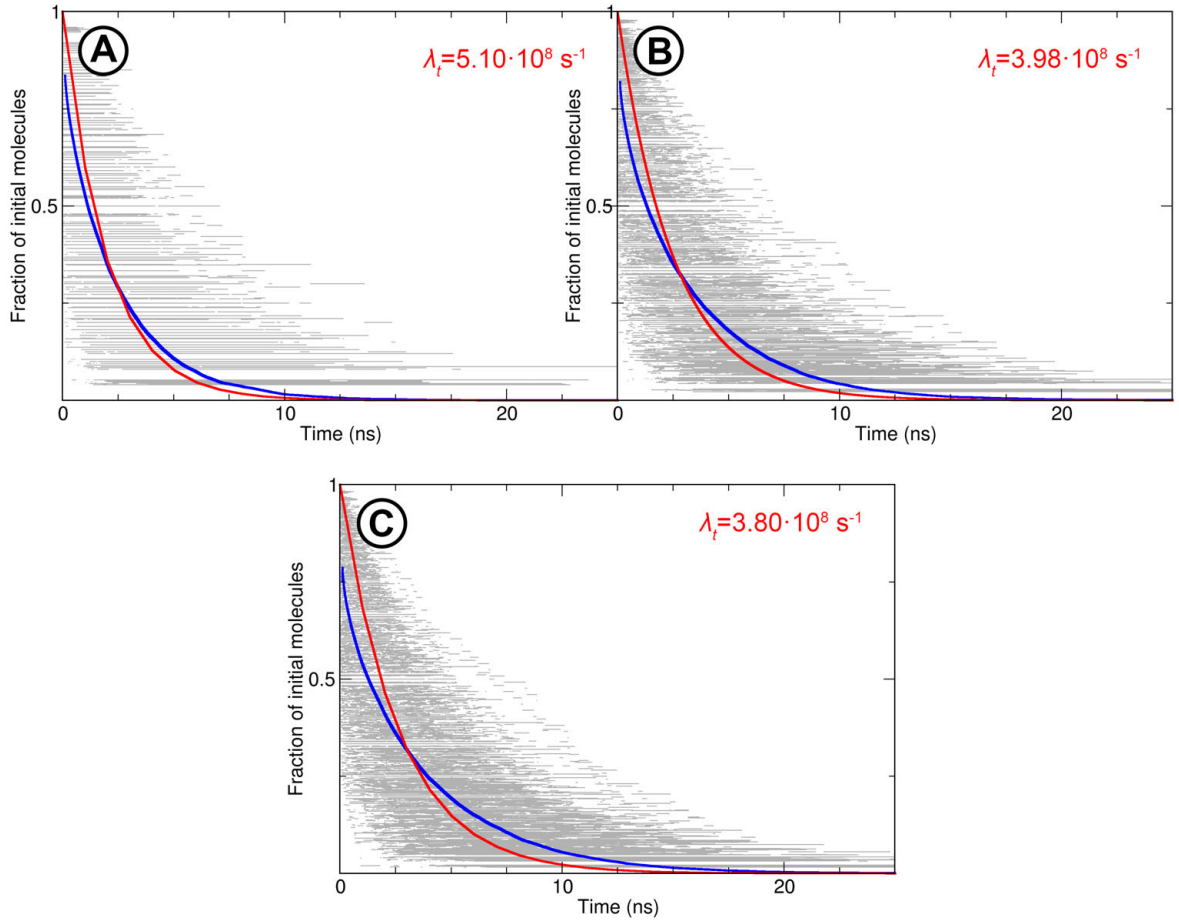

Figure 3.10: Decline of initial molecules in clusters of aggregation number **A** 22, **B** 40, and **C** 55. **Grey** dots represent the individual data points obtained from the analyses of 440 micelles. Connecting lines are omitted for reasons of clarity. A 10000-point moving average is shown in **blue** in addition to an exponential function of the type $[Y] = e^{-\lambda_t \cdot t}$ in **red**. The associated decay constant is annotated in the respective diagram.

The graph reflecting the lowest sum demonstrates that indeed, pre-Ouzo aggregates exist that show negligible fluctuations comparable to the surfactant micelles. Yet whilst differences between the three graphs for CAP micelles are altogether minor and each of those aggregates would be suited for a decay analysis using the method proposed here, the behavior of octanol micelles is decidedly diverse. In case of maximum fluctuation

intensity, a reference aggregation number does not exist. Over periods of hundreds of pico seconds, the cluster size flickers between values close to $N_{agg} = 30$ and $N_{agg} = 80$ or greater. The longest time span of quasi-constant size is less than 150 ps, a value that is over an order of magnitude smaller than the time scale on which the decay of initial molecules occurs. Even the graph representing the mean severity of fluctuations exhibits several jumps corresponding to almost a doubling of aggregation number. These fluctuations occur abruptly, suggesting that the processes of coalescence with other micelles and spontaneous disintegration into smaller objects play a major role in the dynamics of this SFME.

As reasoned in Section 2.5, processes of swelling and disintegration distort the degression rate of initial molecules profoundly for plain combinatorial reasons. Incorporation of another aggregate will lead to a slower decay, as more monomers are available to be randomly exchanged with the surrounding medium. By contrast, breakdown into two or more smaller aggregates will cause the algorithm to further follow one of these, containing a fraction of initial molecules not necessarily related to its size. This is recorded as a primary drop in initial molecules followed by a decay dictated by the ratio of initial molecules to the total number of particles in the "new" micelle. The latter process becomes more and more important, the larger the examined aggregates are, as disintegration into smaller clusters of preferred aggregation numbers becomes possible. This explains why the first value in the running average for $N_{agg} = 55$ is well below 80 %, whereas it is roughly 85 % for $N_{agg} = 22$.

In awareness of these errors, following the statistical model described in Section 2.5 yields a monomer exchange frequency of approximately $10^{10}\ s^{-1}$ (cf. Table 3.2 for details) for $N_{agg} = 22$, 40, and 50, which is at least one order of magnitude higher than was determined for the classical micelles.

Table 3.2: Dissociation constants k derived by means of Equation (2.11) by species and underlying exponential decay constants λ_t and λ_N derived from the statistical model presented in Section 2.5 and obtained from the fitting curves to the decay analysis, respectively.

Aggregation number (molecules)	$\boldsymbol{k}$ (s^{-1})	$\boldsymbol{\lambda_t}$ (s^{-1})	$\boldsymbol{\lambda_N}$ (1)
22	$0.99 \cdot 10^{10}$	$5.10 \cdot 10^{8}$	$5.13 \cdot 10^{-2}$
40	$1.57 \cdot 10^{10}$	$3.98 \cdot 10^{8}$	$2.53 \cdot 10^{-2}$
55	$2.07 \cdot 10^{10}$	$3.80 \cdot 10^{8}$	$1.83 \cdot 10^{-2}$

The high rate of fluctuations raises the question of average stability of the aggregates. The size distribution histogram reviewed in Section 3.2.1 sheds light on the frequency at which certain aggregation numbers are detected, but does not contain any information on how long-lived these structures are. The green graph displaying maximum amplitude in fluctuation, for example, would translate into a cluster size histogram with two peaks at

$N_{agg} \approx 25$ and 80, but, as mentioned before, none of these detected aggregates remains stable for longer than 150 ps.

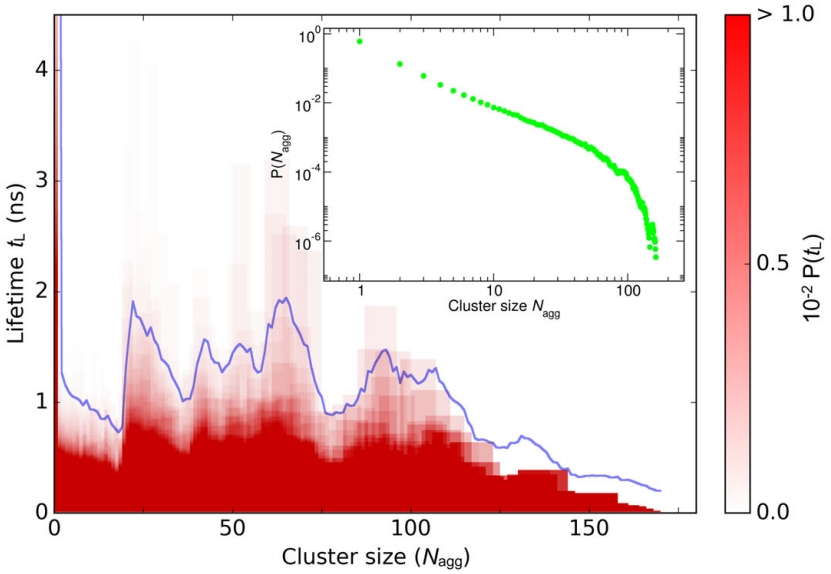

Figure 3.12: Lifetime t_L of pre-Ouzo aggregates by aggregation number. **Red** bars represent nonvanishing probabilities P (t_L) by color shading with respect to the color bar scale to the right. The **blue** line traces the average, magnified by a factor of 10 for improved visibility. For reference, a histogram of the cluster sizes is shown in the inset.

To address this topic, instead of the probability to find an aggregate of size N_{agg} (or a molecule inside an aggregate that size), the probability for these aggregates to exist for a given time period before deviating by more than 5 % from their initial size is plotted in Figure 3.12. To give a more lucid impression of the contributing probabilities, a colormap representation is shown in addition to the distribution of averages. The longest average lifetime is measured for monomers followed by an instantaneous drop for $N_{agg} \geqq 2$ and a subsequent linear decay up to aggregation number ~ 20. At this point, the stability of aggregates steeply increases by a factor of approximately 2.5. Going to larger aggregation numbers, several further local minima and maxima are observed, with the most distinct dips at around $N_{agg} = 35$ and 80, and a pronounced peak at ~ 65, followed by a broad maximum between 90 and 115.

The colormap representation complements this information by showing the probability for the individual events, which give a measure of the tendency of longevity. In narrow zones around particular aggregation numbers, nonvanishing probability for lifetimes significantly longer than the respective average is determined, e.g. $N_{agg} \approx 23$ and 65. By comparison, aggregates containing ~ 35, 80, or more than 120 molecules display a distinctly limited range of lifespans. In general, these characteristics correlate with the distribution of average lifetimes, yet not necessarily in proportion. A plausible explanation

would be that in principle, micelles of certain size would be stable over even longer periods, but limits are imposed by statistical collisions with other clusters. For an evaluation of the convergence of the presented data, it is referred to the supplementary section 3.A.

This consideration shows that mere knowledge of the size distribution is not sufficient for characterizing the kinetic stability of micelles in this polydisperse system. The relative frequency of aggregation numbers between 10 and 110 forms a single broad maximum (cf. Section 3.2.1), but some contributions originate from regularly detected, but short-lived transitory cluster sizes, while others are due to long-living, comparatively stable aggregates.

To emphasize this point, the size histogram of *t*-butanol clusters in binary aqueous solution ($c_{\text{t-but.}} = 1.9\,\text{mol}\,\text{l}^{-1}$) is depicted in Figure 3.13 alongside a lifetime diagram. The distribution strictly follows a power-law with an exponent of approximately -2 with an augmented peak at $N_{\text{agg}} \approx 88$, signifying incipient phase separation. Although probabilities are generally slightly increased over the pre-Ouzo distribution, the lifetime diagram exhibits a uniformly flat signal with only a negligible ascent towards the largest aggregates. This picture is not the result of too low a colormap sensibility to capture the probabilities of events in this particular system, as the contrast is magnified to display any nonzero probability in red. Albeit a trivial fact, it is worth emphasizing that although information about the kinetic stability of aggregates is inevitably encoded in the relative frequency, it cannot be deduced in reverse.

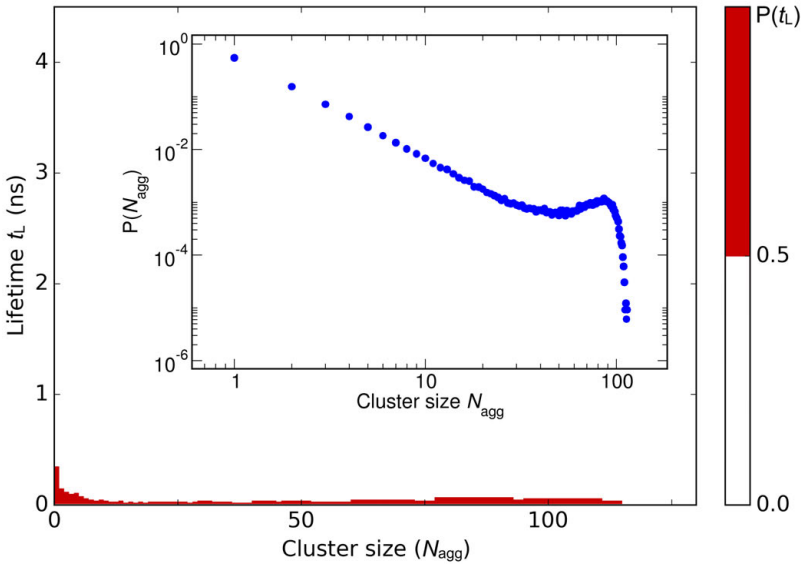

Figure 3.13: Lifetime t_L of *t*-butanol aggregates in a binary mixture with water by aggregation number. The **red** bars represent the maximum lifetime. The inset shows the associated size distribution of clusters. The y-axis scaling is chosen to match that of the pre-Ouzo evaluation to facilitate a direct comparison.

3.2.5 Sphericity

So far, the aggregates were treated as spherical objects. This assumption is reasonable for the extraction of averaged data over the considered time spans given the quick rearrangements described in the previous section. In a further step to characterize the structures emerging in water/ethanol/octanol, their eccentricity is determined analogously to Section 2.3. Figure 3.14 depicts histograms of η and corresponding box plots for octanol clusters with aggregation numbers 22, 40, 55, and 100. Table 3.3 contains extracted key data of the surfactant-free micelles and juxtapositions of these quantities to those obtained for the least spherical ionic micelles that are formed by OTA.

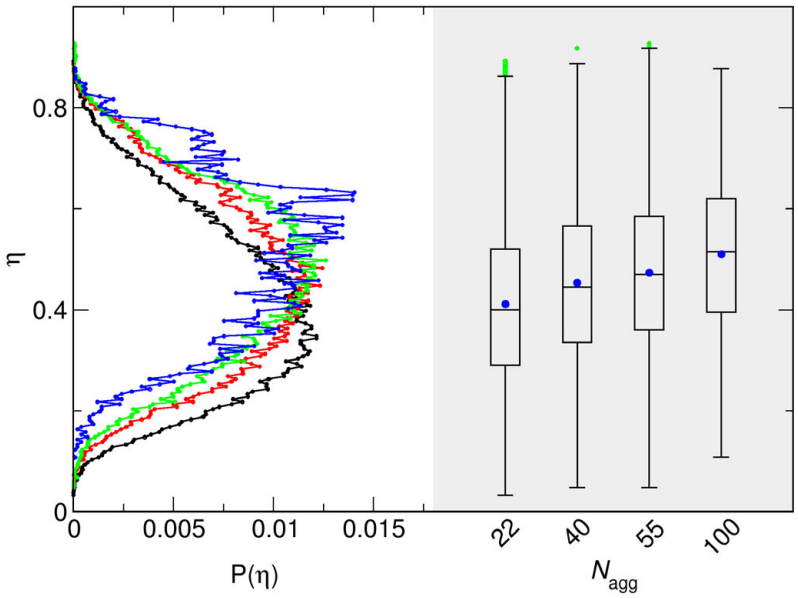

Figure 3.14: Histograms of eccentricity η and corresponding box plots for pre-Ouzo aggregates of size 22 (**black**), 40 (**red**), 55 (**green**), and 100 (**blue**) molecules.

Table 3.3: Mean values of eccentricity $\bar{\eta}$ and interquartile ranges IQR of the distributions by aggregation number. The two rightmost columns show the deviations from the values obtained for OTA micelles.

N_{agg}	$\bar{\eta}$	IQR	$\Delta\bar{\eta}$	ΔIQR
22	0.41	0.23	0.13	0.06
40	0.45	0.23	0.17	0.06
50	0.47	0.23	0.19	0.06
100	0.51	0.23	0.23	0.06

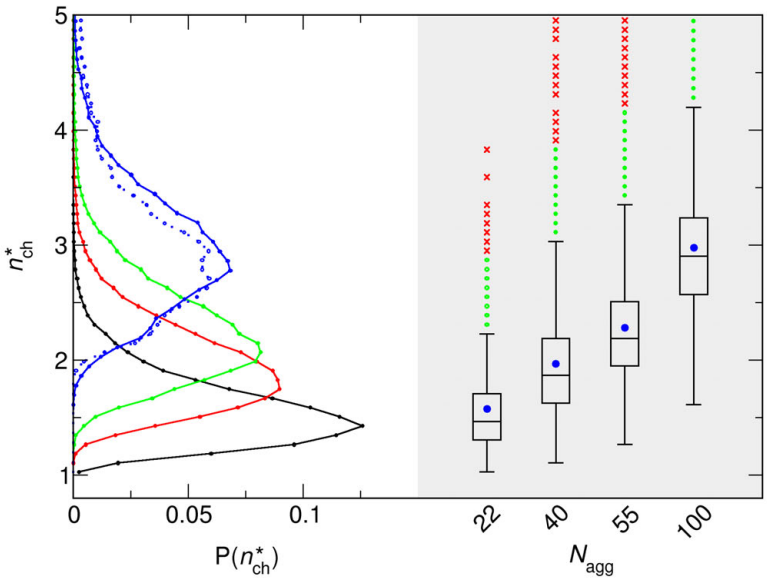

Figure 3.15: Relative deviation of the particle density inside the convex hull of aggregates of size 22 (**black**), 40 (**red**), 55 (**green**), and 100 (**blue**) from that of an ideal $N_{agg} = 22$ micelle $\bar{n}^*_{ch}$. For the largest aggregates, the distribution was obtained using corrected distance evaluation. The dashed (**blue**) line shows the uncorrected results.

N_{agg}	$\bar{n}^*_{ch}$	IQR
22	1.58	0.40
40	1.97	0.56
55	2.28	0.56
100	2.98	0.67

Table 3.4: Mean values of n^*_{ch} and interquartile ranges IQR of the distributions by aggregation number.

The pre-Ouzo aggregates uniformly appear at higher eccentricities and generate more widespread distributions, due to stronger fluctuations in shape. Going to larger aggregation numbers, there is a noticeable trend towards higher eccentricity, reaching a maximum of $\bar{\eta} = 0.51$ for cluster sizes of 100. Furthermore, superimpositions appear in the distribution for $N_{agg} = 100$, that significantly contribute to the relatively high average. These features are artifacts produced by aggregates that span more than half the box length. Using periodic boundary conditions, the distance between two points is usually the minimum of the direct distance and the distance from one point to the closest periodic image of

the other. If the dimension of an object exceeds that of half the simulation box, this criterion produces incorrect connection vectors and a more complex (and much more expensive) approach is necessary. Here, however, the contribution of the false results is not critical, but merely leads to underestimation of the already high eccentricity. At most, this deficiency causes clipping of the right-hand side of the distribution for $N_{agg} = 100$ as those less symmetrical aggregates are captured as artifacts in the superimposed modes. In the previously introduced radially symmetric analyses, however, incorrect distance computations would affect the outcome inextricably and, given their frequency for $N_{agg} = 100$, yield misleading results.

A chart of the particle density inside the convex hull of the surfactant-free micelles normalized to an ideal $N_{agg} = 22$ micelle (cf. Section 2.3) in Figure 3.15 in conjunction with the abstracted data in Table 3.4 clarifies that profoundly less convex structures emerge than is the case for the investigated surfactant micelles. Moreover, the distributions for larger aggregates are offset towards higher n^*_{ch}. This is confirmed by the snapshots of the most compact aggregates in Figure 3.16, which illustrate that even the most compact micelle is a concave structure for aggregation numbers $N_{agg} \geq 40$. Micelles of size 100 are conclusively characterized by both, the outline of the most compact micelle, and the secluded location of the distribution with onset close to $n^*_{ch} = 2$, as loose agglomerates of nondescript shape. In this case, a separate run of the analysis using corrected distance vectors was performed for the largest aggregates, since fragmentation of the structure resulting from incorrect distance evaluation can result in a widely underestimated particle density. However, this merely entails a minor decline of the mean from $\bar{n}^*_{ch} = 3.16$ to 2.98.

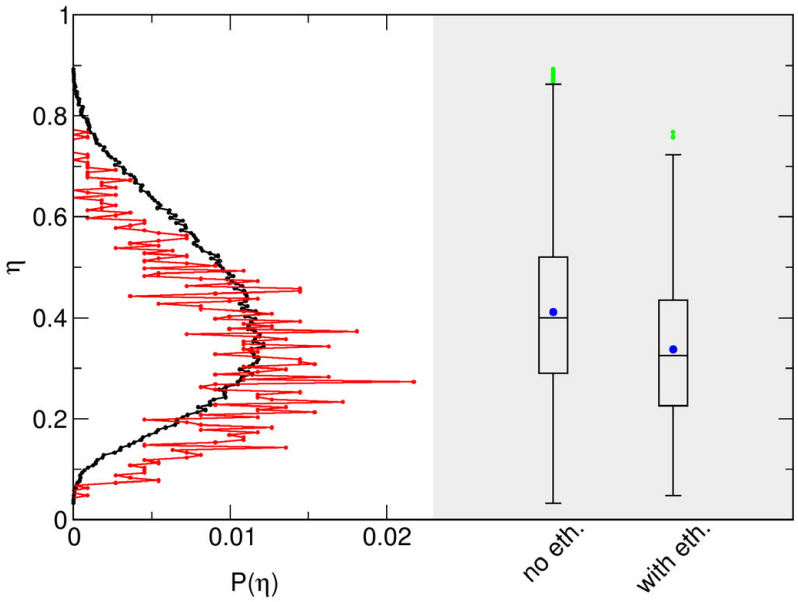

Figure 3.17: Histogram and box plot of the eccentricity η of $N_{agg} = 22$ octanol aggregates under inclusion of bound ethanol (**red**) next to the distribution and box plot for octanol only (**black**).

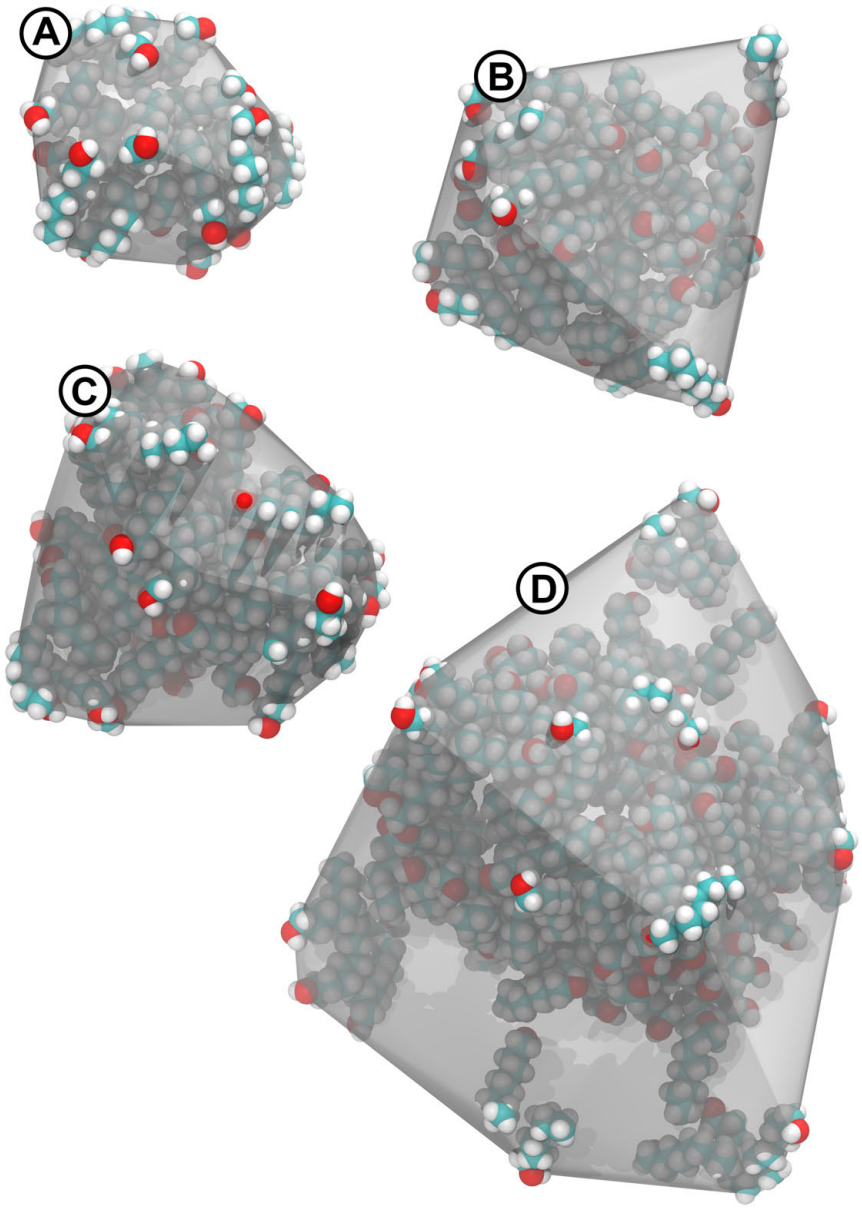

Figure 3.16: Snapshots of the most compact pre-Ouzo aggregates of aggregation number **A** 22, **B** 40, **C** 55, and **D** 100. A representation of the convex hull surface is shown around the clusters in translucent **grey**. Although all coordinates lie inside the convex hull, the envelope is permeated by the van der Waals representation chosen for better visibility.

If in addition to octanol molecules, all bound ethanol (cf. Section 3.2.2) is considered to be part of the aggregate, a substantial shift in eccentricity is observed, as displayed in Figure 3.17. Owing to the costly procedure of allocating ethanol molecules to an aggregate, this analysis was performed on a comparatively small data set only, which entails a significant amount of noise in the graph. The general consequence, however, is evidently the detection of objects of significantly increased sphericity with an average of $\bar{\eta} = 0.34$. This value is close to the mean eccentricity of $\bar{\eta} = 0.28$ computed for the OTA micelles.

With the results of Section 3.2.4 in mind, it is reasonable to examine the correlation between sphericity and temporal stability of the aggregates. This is realized in Figure 3.18 by determining the average sphericity tied to the lifetime of a $N_{\mathrm{agg}} = 22$ octanol micelle as defined by the timespan during which it does not deviate by more than 14 % from its initial size. Shown is a probability colormap overlaid with the curve of average lifetime. A plain peak at $\eta \approx 0.23$ clearly proves that higher stability is, at least on average, accompanied by higher spherical symmetry. In other words, the high η contributions in the frequency domain are due to short-lived aggregates, that are, in a sense, momentary manifestations of the size fluctuations in the system.

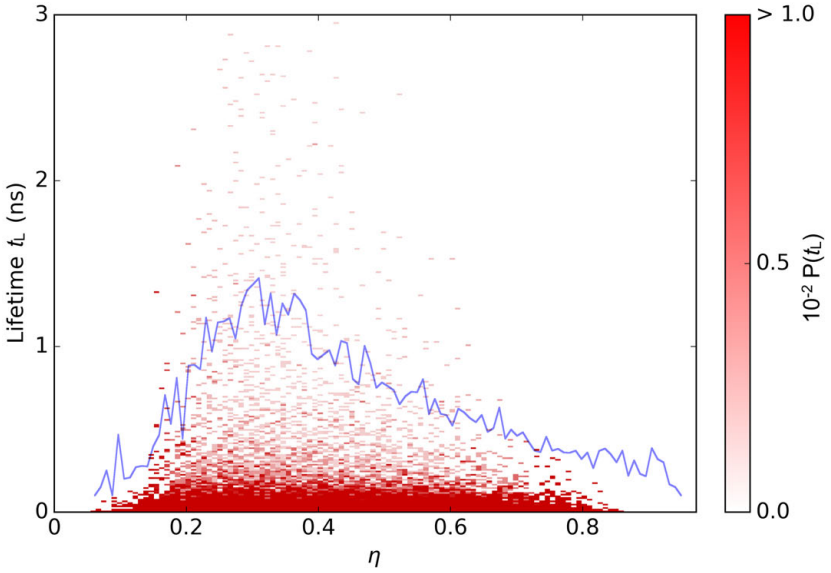

Figure 3.18: Lifetime t_L of size 22 aggregates as a function of eccentricity. **Red** areas indicate nonvanishing probabilities P (t_L) by color shading with respect to the color scale to the right. The **blue** line traces the average, magnified by a factor of 10 for improved visibility.

Taken together, the results further solidify the picture of micelle-like structures in the pre-Ouzo region, provided that the concept of aggregation is extended to include the bound hydrotrope molecules. The average sphericity is further diminished by the strong size fluctuations that characterize this system. Those entail contributions in the high-η

regime of significant overall weight affiliated to comparatively short-lived aggregates. The geometric similarities between surfactant free and classical micelles diminish with growing aggregation number as octanol molecules form progressively less spherical structures. Deviation from ideal spherical shape is known to occur in classical surfactant micelles beyond a critical aggregation number.[73] The length of the hydrophobic tail dictates the maximum diameter of a micellar aggregate before a cavity would be formed in the center. This constraint can be circumvented by a change of geometry.

3.2.6 Solubilizing properties

The targeted utilization of ouzo-like systems in any scope of application, whether as a reaction or extraction medium, or as a solvent, puts demands on the solubilization capability of the microemulsion. In order to assess this property, two experiments are conducted. Firstly, small amounts of the apolar compound squalene are added to composition α. This 30-carbon organic compound is virtually insoluble in water and is large enough to induce sufficient changes in the nano-ordering to allow for a phenomenological study. Secondly, the solvation free energy of one propane molecule is evaluated as a function of the distance to an aggregate.

3.2.6.1 Solubilization of squalene

Squalene is an organic unsaturated compound of the triterpene class (cf. Figure 3.19) with sum formula $C_{30}H_{50}$ and systematic IUPAC name (6E,10E,14E,18E)-2,6,10,15,19,23-Hexamethyltetracosa-2,6,10,14,18,22-hexaene.

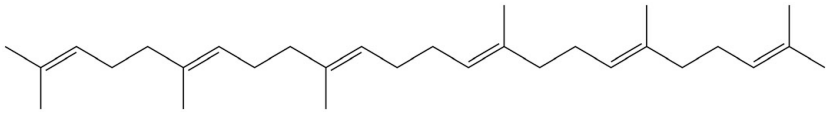

Figure 3.19: Structure formula of a squalene molecule.

It occurs naturally, among others, in humans as an essential component of epidermal surface lipids and is present in the blood serum.[214,215] It is further a biochemical precursor to all plant and animal sterols.[216] It's insolubility in water and only marginal solubility in alcohol[217,218] qualify this substance as a well-suited trial case in the determination of the solubilization capability of an SFME.

In order to make any assertion about the solubilizing properties of pre-Ouzo aggregates it is necessary to examine the situation in an analogous water/ethanol mixture. For this purpose, size histograms of squalene agglomerates in a 4.9 mmol l^{-1} solution (corresponding to four molecules) in composition α and in a mixture of ethanol and water corresponding to that in composition α are compared in Figure 3.20. From those it is plain that even the small octanol concentration of less than 10 mmol l^{-1} significantly improves the solubility of squalene. Whereas in the water plus alcohol mixture, squalene molecules invariably consolidate into one single cluster, the presence of octanol entails the formation of considerable amounts of squalene trimers, dimers and monomers.

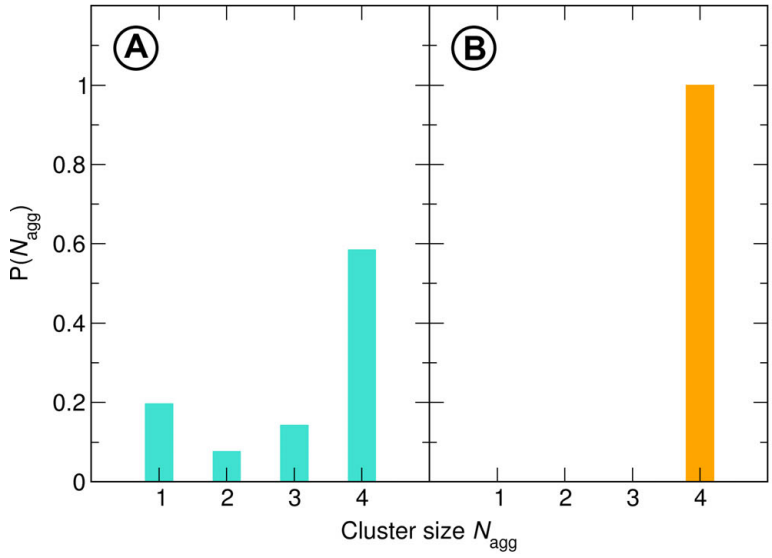

Figure 3.20: Size histogram of squalene clusters in **A** composition α and **B** a water and ethanol mixture with ratio corresponding to composition α. Each system contains four squalene molecules.

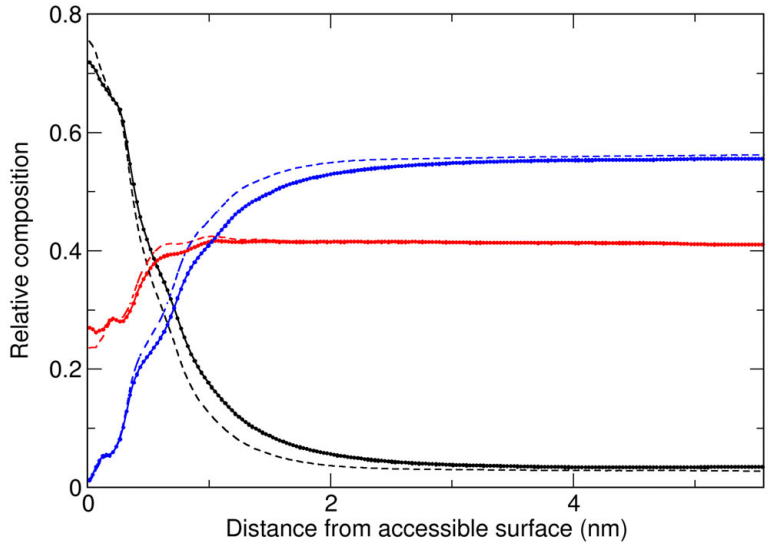

Figure 3.21: Ratio of atoms belonging to octanol (**black**), ethanol (**red**), or water molecules (**blue**) with regard to the accessible surface of squalene (cf. Section 1.2). Solid lines are drawn for a system containing one squalene molecule and dashed lines for the 4.9 mmol l^{-1} mixture.

The proximal distribution of system components with regard to squalene in Figure 3.21 shows that, as expected, primary contacts are most likely with octanol molecules. Besides, a moderate amount of ethanol is present in close vicinity to the surface, that equates to

roughly 65 % of the bulk value in case of one squalene molecule in the system. By contrast, only few water molecules enter the near environment and the probability of encountering a water molecule directly at the surface is almost zero. Snapshots of a squalene agglomerate in the 4.9 mmol l^{-1} solution and its immediate surroundings are depicted in Figure 3.22.

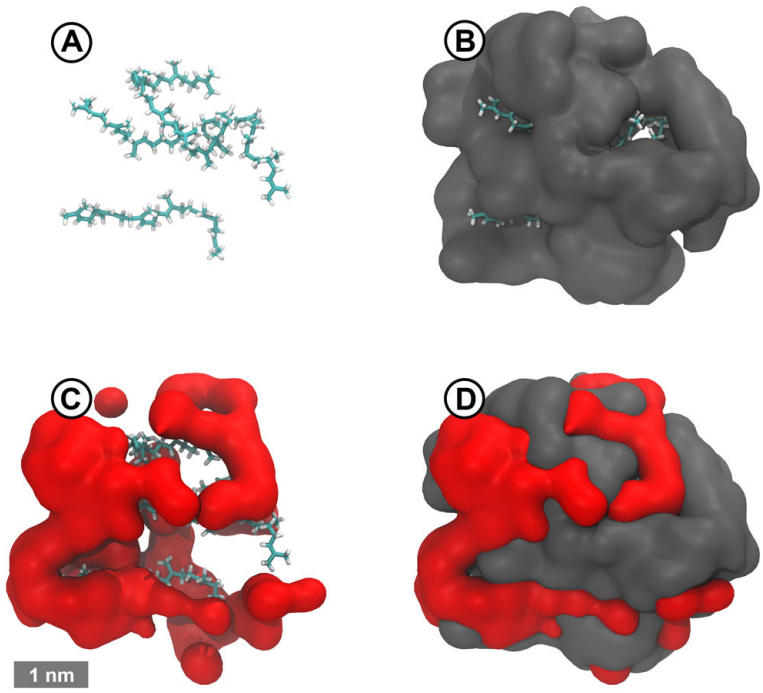

Figure 3.22: Stick representation of an agglomerate of four squalene molecules **A** displayed isolatedly, **B** in conjunction with a surface representation of octanol within 0.66 nm of any squalene atom, **C** in conjunction with a surface representation of ethanol within 0.66 nm of any squalene atom, and **D** in conjunction with a surface representation of ethanol and octanol within 0.66 nm of any squalene atom. The surface calculated from octanol coordinates is colored **grey**, that from ethanol coordinates **red**.

Octanol and ethanol molecules unite to a composite intertwined conformation encompassing the squalene molecules. Thereby, the closest surface contacts are the hydrophobic tail sections of the alcohol molecules as disclosed by the proximal distributions in Figure 3.23.

In each case, this initial peak* is followed by a maximum in oxygen probability. In case of ethanol the two profiles are staggered in terms of several alternating maxima, whereby the distance between the first oxygen and carbon peak equates to 0.18 nm. This value is very

*The fact that the primary extrema are preceded by converging probabilities is a consequence of unfavorably close distance. Zero is defined as the distance where the Lennard-Jones potential between two particles equals $k_B T$, therefore this immediate region is dominated by statistical events rather than allocation due to beneficial interactions.

close to the expected difference in distance from the surface for adsorption perpendicular to the C–C bond, when working with the average C–C–O angle of 109.5°*. Two further layers repeated on this characteristic length scale are observed at larger distances from the accessible surface. The respective signals are progressively dampened as correlations vanish until the curves permanently coincide from a distance of approximately 1.5 nm onward.

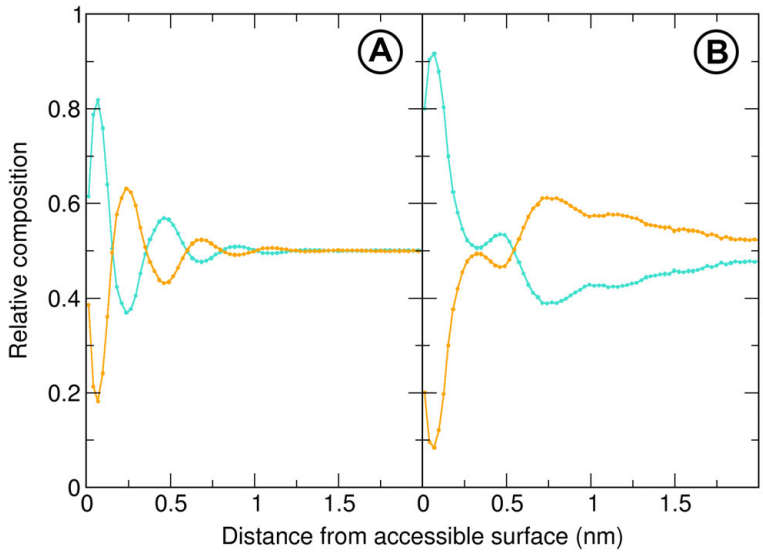

Figure 3.23: Ratio of terminal carbon (turquoise) to oxygen atoms (orange) belonging to **A** octanol and **B** ethanol molecules as a function of the distance to the accessible surface of a squalene molecule.

The first layer of polar ethanol head groups shows up in the octanol profile in form of a local minimum of carbon and local maximum of oxygen atoms. A clear reversal of probabilities, that signifies the boundary of an octanol layer, occurs at a greater separation of ~ 0.5 nm, after intermittent re-bifurcation of the curves within the apolar section of the second ethanol layer. The subsequent maximum in the oxygen graph reaches its highest value close to 0.8 nm and decays slowly towards larger distances, signifying a diffuse interface. Superimposed on this feature is a shallow minimum that follows the prior local maximum at a separation of ~ 0.7 nm. At the present level of accuracy, this coincides with the distance between initial carbon and main oxygen maximum and thus gives a characteristic measure of the thickness of the octanol layer. A valuation of this result can be made by means of a phase separated water/octanol slab system. In agreement with similar studies,[219,220] octanol molecules assemble to bilayer-like structures at the interface as shown in Figure 3.24. The typical end-to-end distance in this configuration is 0.9 nm.

*The actual result for this simple model is a difference of 0.21 nm, taking into account the small difference in effective van der Waals radii of on average 0.01 nm. This deviation is within the uncertainty introduced by the finite interval width of 0.03 nm.

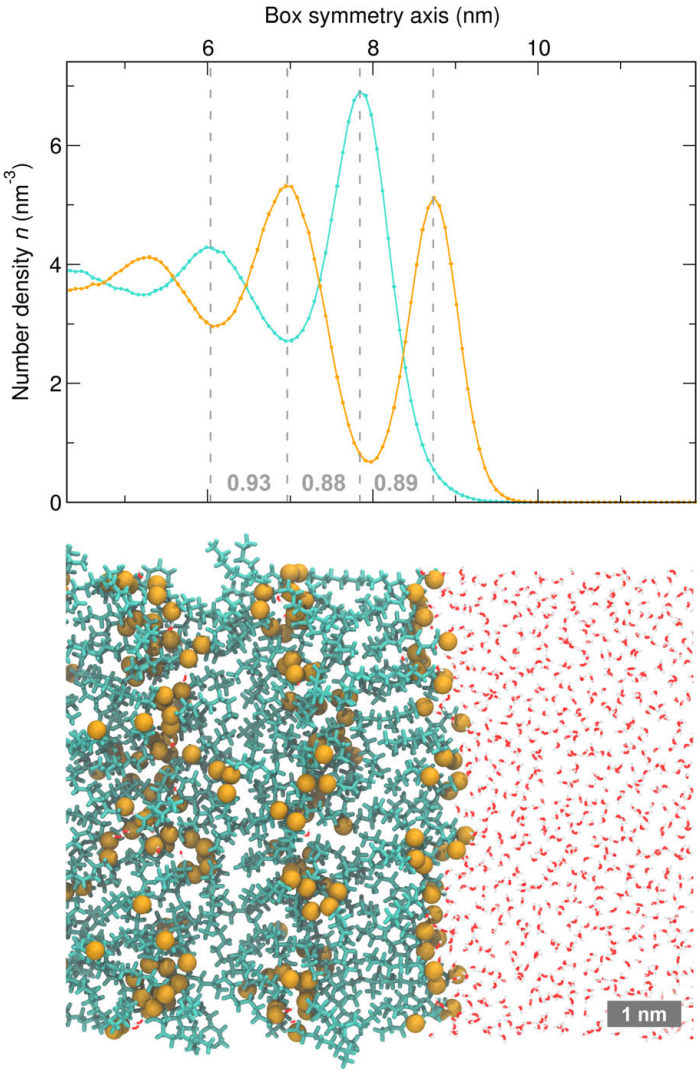

Figure 3.24: Illustration of a slice of 1 nm thickness through the simulation box of a water/octanol slab system. Octanol alkyl tails are depicted in **turquoise** stick representation, the hydroxyl groups are accentuated as **orange** beads, and water is shown in a line representation. The rendering is positioned to give a visual match to the location-dependent number density n of terminal carbon (**turquoise**) as well as octanol oxygen atoms (**orange**). The compartments identified to correspond to the extent of one octanol layer by means of the separation of maxima and the measured widths are indicated in the diagram for the first three oscillations.

An explanation for this discrepancy is the softening of that otherwise strict arrangement by interactions with other hydrophobic moieties that are not present in the slab system.

The ordering of organic compounds around the squalene molecules evokes distinct rearrangements in the characteristic size distribution of octanol aggregates as shown in Figure 3.25.

Even if only a single squalene molecule is added (tantamount to 1.2 mmol l^{-1}), the formerly broad maximum between $N_{agg} = 10$ and 110 is overall depressed except for a narrow region around $N_{agg} = 80$, where the probability is considerably elevated. The included conditional size distribution clearly correlates this particular feature, as well as two preceding minor peaks that do not stand out against the original distribution, to octanol clusters that are in direct contact with the hydrophobic substance. The situation becomes considerably more marked upon enhancement of squalene concentration to 4.9 mmol l^{-1}.

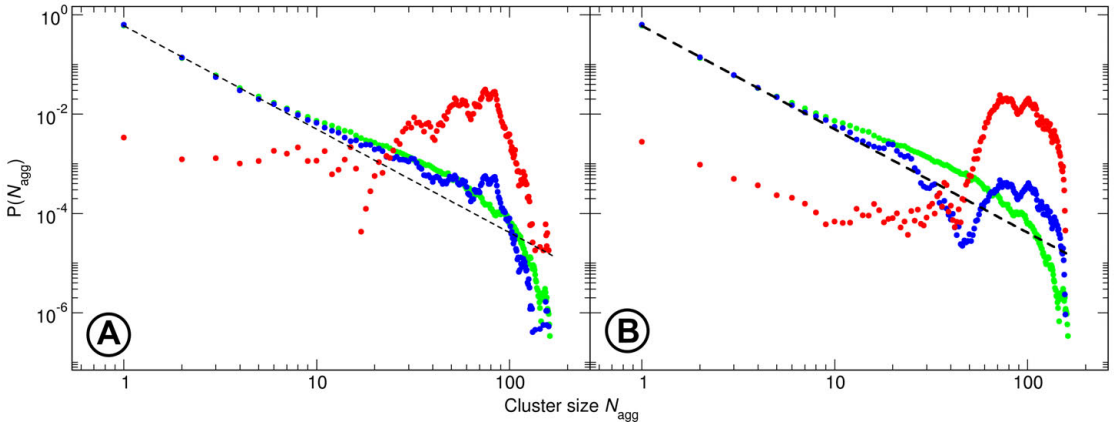

Figure 3.25: Size histograms of octanol clusters in composition α upon the addition of **A** 1.2 mmol l^{-1} and **B** 4.9 mmol l^{-1} squalene represented by **blue** dots. The distribution in the pure system is supplied in **green** and the size histogram of clusters in direct contact with squalene in **red** color.

The resulting distribution is decidedly dominated by large aggregates within cutoff distance to squalene molecules. The relative frequency of smaller aggregates, especially close to size $N_{\text{agg}} = 45$, is significantly reduced compared to the original histogram. These observations are not surprising in a system exhibiting weak aggregation, since it is known that solutes can in some circumstances strongly affect micellar structure in conventional microemulsions.[221,222]

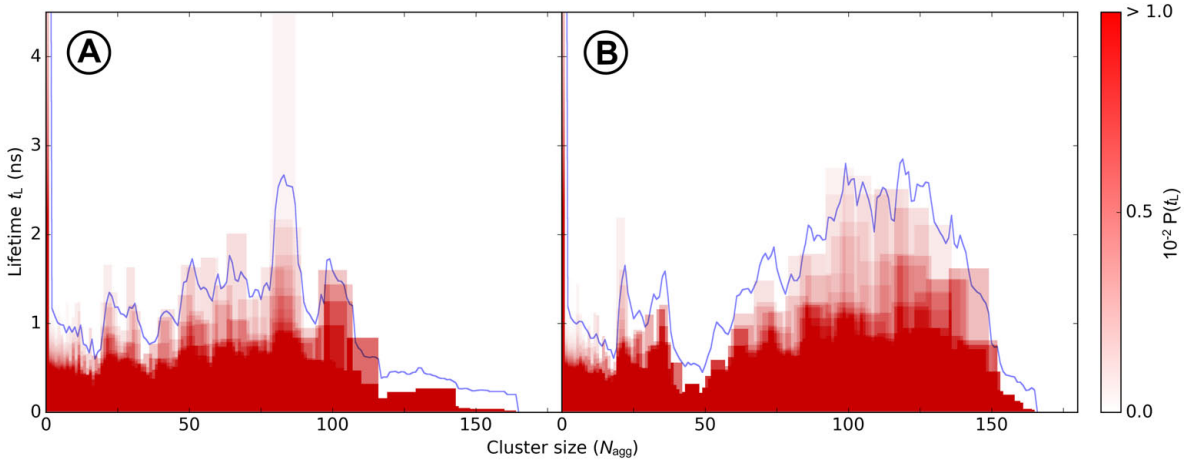

Figure 3.26: Lifetime t_{L} of octanol aggregates by aggregation number in composition α containing **A** a single squalene molecule and **B** four squalene molecules. **Red** bars represent nonvanishing probabilities $\text{P}(t_{\text{L}})$ by color shading with respect to the color bar scale to the right. The **blue** lines trace the averages, magnified by a factor of 10 for improved visibility.

The emerging structures are relatively stable over time as displayed in Figure 3.26 by means of the same type of colormap plot already employed in Section 3.2.4. In this case, the distributions in frequency and life-time domains are very similar. Clusters of aggregation numbers likely to be found close to squalene molecules exist for significantly longer time spans than aggregates of the same size in the pure composition. Conversely, aggregates close to size 45, the minimum in the frequency domain, are never traced for longer than 250 ps.

3.2.6.2 Solvation free energy of propane

The goal of this particular study is to quantitatively assess the solubilization power of pre-Ouzo micelles. To this end, a single propane molecule is added to composition α. For a single, comparatively small molecule, the induced perturbation is expected to be negligible.

Propane being a nonpolar hydrocarbon, its solubility in water is rather poor with a solvation free energy of 13.8 kJ mol^{-1}.[223] In a system partitioned into distinct domains of prevailingly polar and apolar nature, the solvation free energy should substantially depend on the location of this molecule. A common approach for free energy calculations along a space coordinate is umbrella sampling. However, application of this method is problematic since it would necessitate adequate sampling within different distance intervals to selected reference points in the respective pseudo-phases. Given the rapid rearrangements reviewed in Section 3.2.4, configurationally consistent data on a time scale exceeding a few nanoseconds can only be recorded by applying positional constraints to the structures. To avoid this additional bias, the approximate solvation free energy is determined by means of a method based on energetic representation as implemented by the ERmod project.[158,160,161] The quick convergence of this method renders it a suitable approach for a conditional analysis in terms of the aggregate-propane distance. In a similar study, this approach already proved viable in the analysis of solubilization in a sodium dodecyl sulfate micelle.[224]

To establish reference values, solvation free energies for propane are calculated in pure water, pure ethanol, pure octanol, and the respective compositions of the polar and apolar domains in composition α. The result for water only is 13.9 kJ mol^{-1}, which agrees very well with the experimental value mentioned earlier. For ethanol, a moderately favorable value of -3.6 kJ mol^{-1} is obtained. These isolated outcomes already suggest that plain addition of ethanol to water is unlikely to produce a good solvent for the alkane hydrocarbon. By contrast, octanol presents a favorable medium with a predicted solvation free energy of -10.6 kJ mol^{-1}.

Systems representing the aqueous and octanol-rich pseudo-phases are generated with the water/ethanol and octanol/ethanol ratios appointed by means of the interaction energy criterion introduced in Section 3.2.2. In the organic mixture, consisting of 16 (mole)% octanol and 84 % ethanol, the solvation free energy results to -6.7 kJ mol^{-1}. Consequently, this mixture of ethanol and octanol is still a good solvent. Accordingly, the complementary pseudo-phase consisting of 83 % water and 17 % ethanol is still a poor solvent with a free energy of solvation of 7.5 kJ mol^{-1}*.

*The thus far stated values are all within a 0.14 kJ mol^{-1} margin in terms of the 95 % error computed by ERmod.

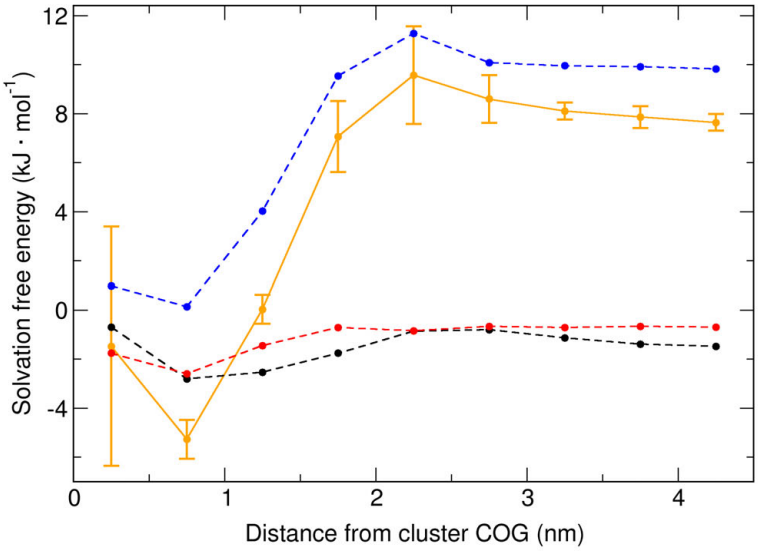

Figure 3.27: Solvation free energy of propane in composition α as a function of the distance from the center of geometry of an aggregate containing 25 octanol molecules, represented by the solid **orange** line. The individual contributions of octanol (**black**), ethanol (**red**), and water (**blue**) are shown as dashed lines.

In a next step, a simulation of one propane molecule in composition α without additional bias is analyzed. The solvation free energy is evaluated in concentric regions of 0.5nm width around the geometric center of a $N_{\text{agg}} = 25$ octanol micelle. The respective contributions of the system components as well as the total are radially resolved in Figure 3.27.

Along the lines of the considerations in Section 3.2.3, the interface can be assumed to be located close to 1 nm. Below this value, and consequently inside the micelle, a favorable solvation free energy of $-5.3\,\text{kJ mol}^{-1}$ is computed, which is only slightly smaller than the result for the corresponding binary system. In this distance segment, the primary contributions originate from ethanol and octanol. In proximity to the expected interface, a change of sign occurs, when the water contribution becomes significant and the solvation free energy swiftly increases, settling to values in the range $7-8\,\text{kJ mol}^{-1}$ for large distances. Outside the aggregate, the hydrophobic effect predominates and leaves the ethanol and octanol contributions as secondary influential factors.

The distribution of data points suggests most unfavorable conditions at separations between 1.5 and 3 nm from the core, where consistently sampling is poor. Consequently, the error in this region is material and margins even overlap with the adjacent data points, which effectively masks the curve shape. To understand this behavior, it is helpful to examine the immediate surroundings of a propane molecule as a function of the distance from the micelle COG. For this purpose, the composition of the first solvation shell of the hydrocarbon is shown in Figure 3.28.

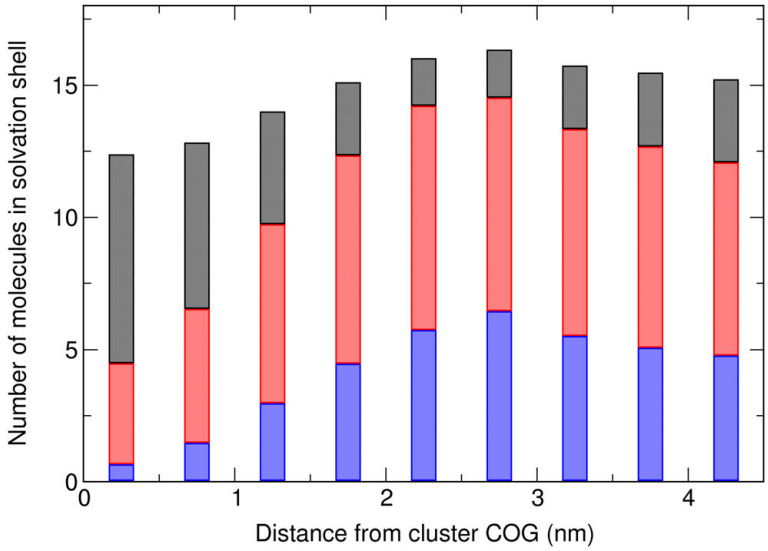

Figure 3.28: Composition of the first solvation shell of a propane molecule in composition α as a function of the distance to the geometric center of an octanol aggregate containing 25 molecules. **Black** bars represent the count of octanol, **red** bars the count of ethanol, and **blue** bars the count of water molecules.

It is obvious that the region of poorest solubility overlaps with the distance intervals in which the least amount of octanol contacts are counted. This is compensated by a higher number of ethanol and water molecules and thus explains the comparatively small number of data frames satisfying this condition. This distance range coincides with the radial zone in which a depletion of octanol density, that is due to the natural spacing between aggregates, was ascertained during the discussion of the micellar structure in Section 3.2.2.

The actual interface that is enriched with polar hydroxyl groups does not produce any noticeable feature in the solvation free energy profile. The polar shell formed by the outwardly oriented polar head groups, that is deliberately visualized in Figure 3.29, is in itself not a favorable environment for a polar compound. However, in this radial segment, ethanol forms a diffuse interfacial layer which entails local enhancement also of the hydrotrope concentration. This effectively reduces the overall polar character of the micelle boundary and rationalizes the smooth slope of the graph.

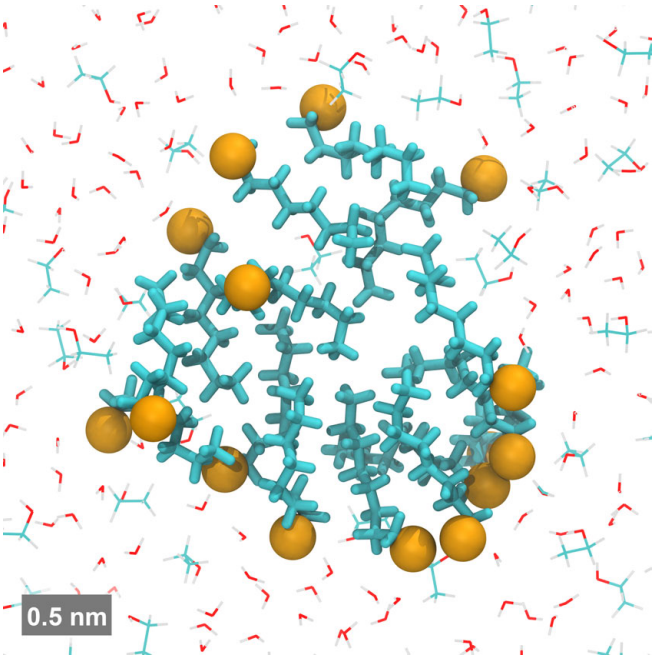

Figure 3.29: Rendering of a 1 nm thick slice through an octanol aggregate comprising 15 molecules. Octanol is depicted in **turquoise** stick representation and the polar head groups are accentuated as **orange** beads. The remaining system components are shown in in line representation.

3.2.7 Influence of salts

Introductory remark: *This topic is part of the publication in Ref. 225.*

The weakly associated micellar aggregates discussed in this chapter occur only for certain ratios of water, ethanol and octanol. This nano-ordering is easily perturbed by the introduction of apolar domains, for example in form of the dedicated solute squalene as surveyed in Section 3.2.6.1. The sensitivity to changes in system composition naturally raises the question how this SFME responds to the presence of electrolytes, as they are common components in countless systems. This issue is pursued by means of the separate addition of 1 mol l^{-1} NaI and LiCl to composition α.

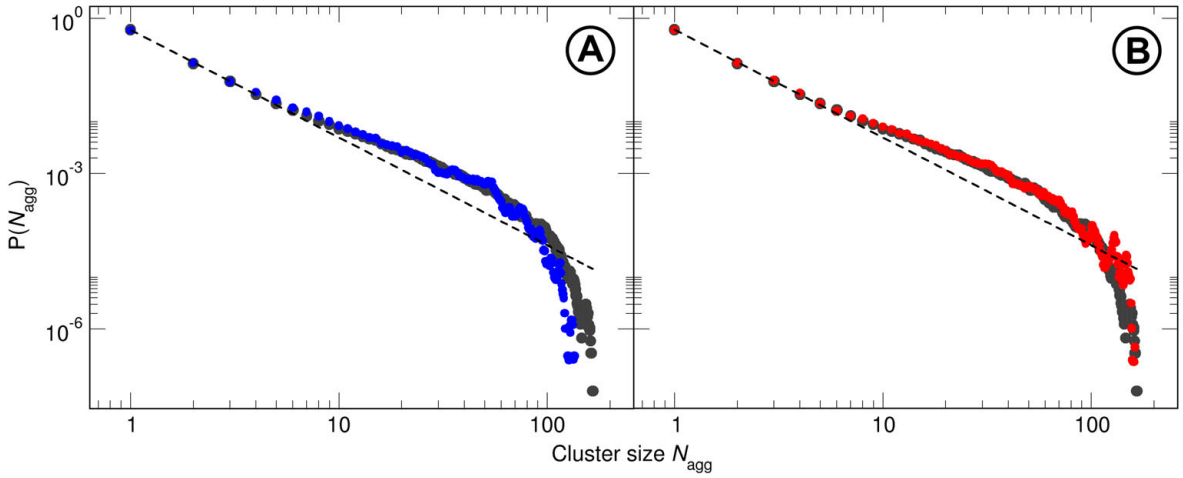

Figure 3.30: Cluster size histograms in 1 mol l^{-1} solutions of **A** NaI and **B** LiCl in color alongside the distribution in the pure system in a shaded representation.

Subtle changes manifest in the size distributions of aggregates as shown in Figure 3.30. The addition of NaI slightly diminishes the broad maximum between $N_{agg} = 10$ and 110, while the frequency of aggregates larger than 100 molecules hardly changes. In case of LiCl, by contrast, an increased probability of large aggregates is observed, while the broad maximum at intermediate aggregation numbers is retained. These changes can be attributed to two effects induced by the presence of electrolytes. On the one hand, the properties of the solvent are altered due to the interaction of water and ethanol with the

ions. On the other hand, the interaction of ions and octanol directly affects the stability of the aggregates. The influence of each of these mechanisms can be traced by the local densities of system components around the micelle centers.

To quantify the impact of the first mechanism, the concentration profiles of ethanol and water around aggregates of size 22 are presented in Figure 3.31. In comparison to the pure ternary composition, the accumulation of ethanol in the interfacial region, as well as its concentration inside the aggregates are significantly augmented in the electrolyte solutions, regardless of the species. Or considered in reverse, ethanol is displaced from the aqueous pseudo-phase, a process that is known as "salting out".[226,227] It is simply the consequence of the limited solubilization power of water that is exhausted by the prioritized solvation of one component over another. This is an ion-specific effect in accordance with the Hofmeister series of salts.[228,229] A side effect of this local enhancement of ethanol concentration is the slight decrease of water density detected in this region. Apart from this weak shift, the water profile remains virtually unchanged.

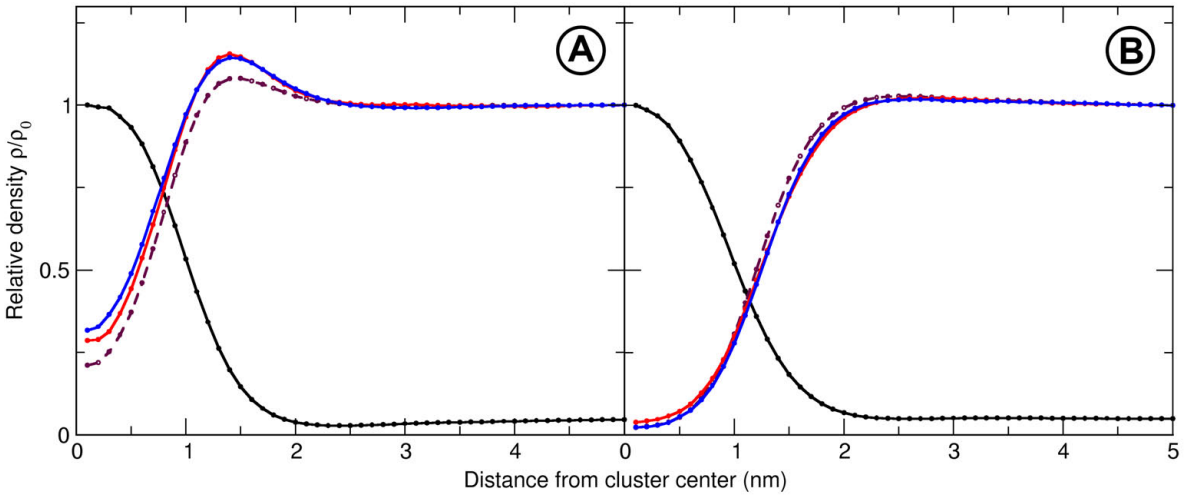

Figure 3.31: Densities of **A** ethanol and **B** water around the COG of octanol aggregates of size $N_{agg} = 22$. Solid **black** lines correspond to octanol, solid **red** lines to the distribution in the NaI solution and **blue** lines in the LiCl solution, respectively, and the dashed **maroon** line to the data obtained from the pure system.

Ethanol being the component mediating mutual solubility of octanol and water, its displacement from the aqueous pseudo-phase effectively pushes the system towards phase separation. An estimate of the relative drop in ethanol concentration can be derived from the difference of the integrated curves with and without salt up to $r = 1.7$ nm, the point where the densities of bound and unbound ethanol cross (cf. Section 3.2.2). This yields a net decrease of 3.0 % aqueous ethanol upon the addition of LiCl and 2.3 % upon the addition of NaCl, with an increase of interfacial ethanol of 12.5 % and 9.8 %, respectively.

The concentration profiles of the ions in Figure 3.32 give information about the influence of the second mechanism at hand. The graphs for respective anions and cations exhibit identical behavior but for small distances from the aggregates. In that region, splitting of the graphs occurs, that is altogether marginal but more pronounced in the case of LiCl. The deviations indicate charge separation at the interface that results in a mildly negative surface charge in the presence of NaCl and a somewhat higher positive surface charge for LiCl. The consequence is an electrostatic repulsion that adds to the stability of the aggregates.[230] Conversely, a charged interface also limits the maximum aggregation number.[231]

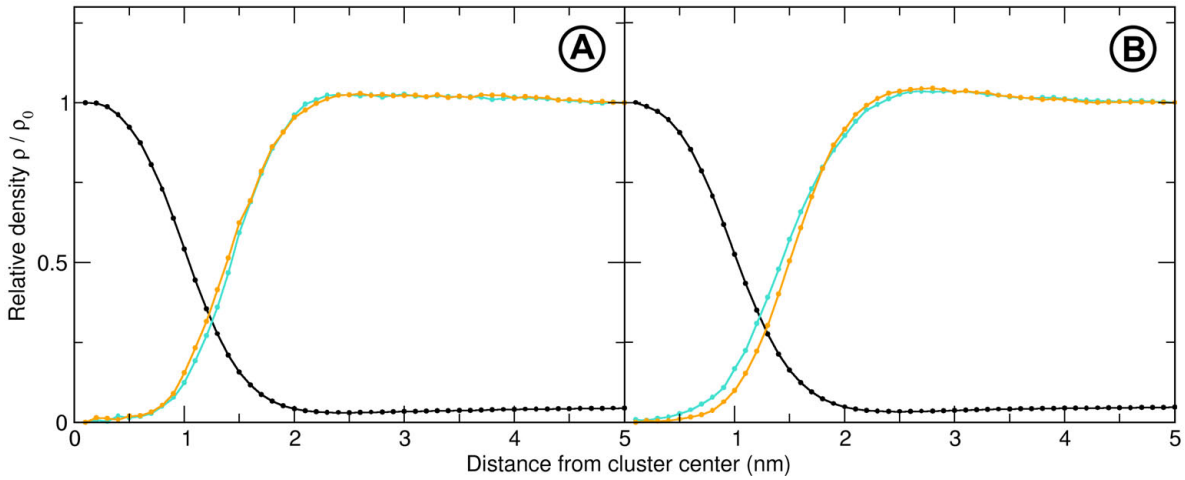

Figure 3.32: Distribution of ions around the COG of $N_{agg} = 22$ micelles in composition α containing **A** NaI and **B** LiCl. Octanol density is represented in **black**, cations in **turquoise**, and anions in **orange**.

However, the effect is rather weak. Lithium and iodide are both known to exhibit distinct preferential adsorption to typical hydrophobic surfaces.[232,233] By contrast, sodium and chloride are attracted to hydroxylated surfaces in a reversal of the Hofmeister classification.[234] Under this premise, the minor surface charge of the pre-Ouzo aggregates is in need of explanation.

In the course of covering this issue, the system is modified step by step towards featuring an entirely hydrophobic surface. Foremost, however, ranks the elimination of possible systematic errors inherent to the analysis method. Averaging over a large number of aggregates that deviate to a greater or lesser degree from ideal spherical shape (cf. Section 3.2.5) may introduce blurring of the graphs, thereby diminishing local differences in anion and cation distributions. This is prevented by performing a separate MD simulation of an isolated average (by means of its radius of gyration) octanol micelle of the considered aggregation number with frozen atom positions in an equivalent composition of water, ethanol, and salt.

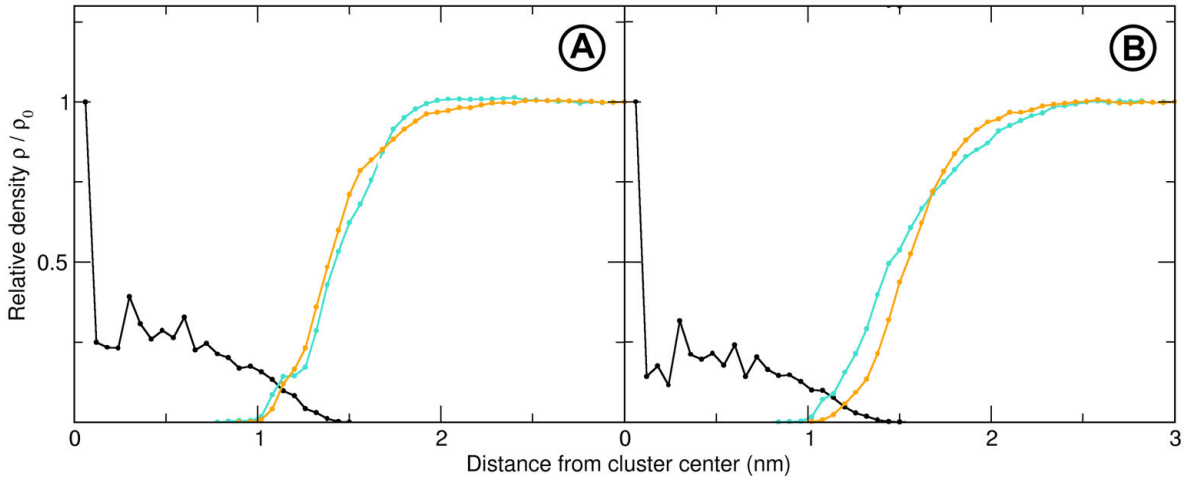

Figure 3.33: Distribution of ions around the COG of a frozen octanol aggregate of size 20 in a water/ethanol mixture of identical ratio as composition α, containing **A** NaI and **B** LiCl. Octanol density is represented in **black**, cations in **turquoise**, and anions in **orange**.

As the resulting graphs in Figure 3.33 prove, averaging over different aggregate geometries has little impact on the distributions of ions and is not the cause for the observed weak charge separation. Due to the immobile octanol atoms, the curve shapes are considerably more jagged than in the previous diagrams, while simulation time is the same. Naturally, the impact is most severe in case of octanol itself, where stationary atom positions cause large spikes.

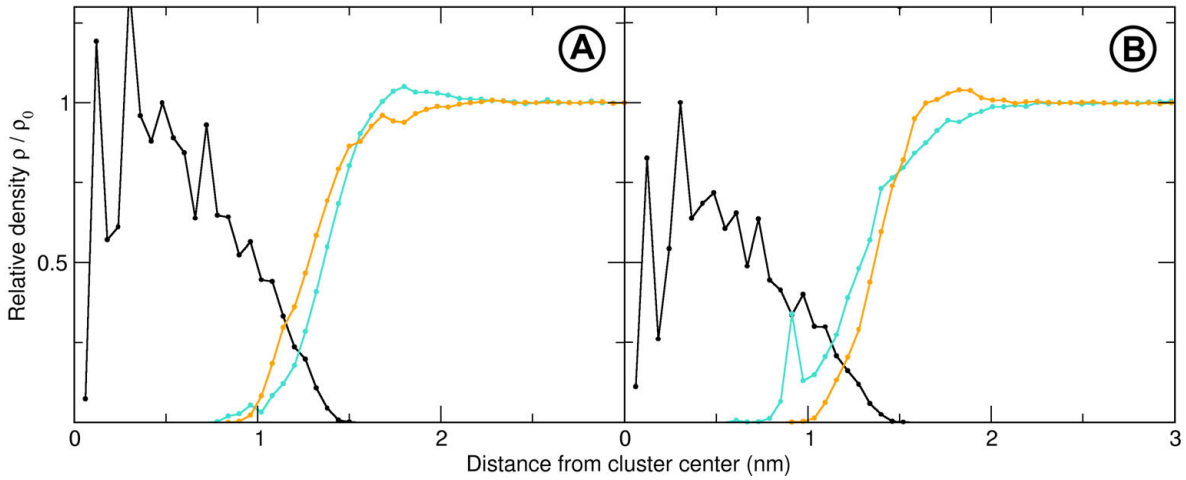

Figure 3.34: Distribution of ions around the COG of a frozen octanol aggregate of size 20 in aqueous solution of **A** NaI and **B** LiCl. Octanol density is represented in **black**, cations in **turquoise**, and anions in **orange**.

With the octanol atoms still fixed, the aggregate surface is next exposed to the aqueous pseudo-phase by removal of ethanol from the system, while maintaining the electrolyte concentrations. As the obtained graphs in Figure 3.34 indicate, the absence of interfacial ethanol leads to a significantly increased adsorption of I^- and Li^+ at the interface, as the apparent surface becomes less polar.

Ultimately, the hydrophobic character of the micelle is maximized by exchanging the octanol hydroxyl groups for hydrogen atoms, thus creating an octane aggregate of similar shape. The purely hydrophobic surface promotes the even more pronounced separation of ions displayed in Figure 3.35. The graphs reflect the distinct charging of the generated apolar aggregate via preferential adsorption of iodide and lithium that in the DLVO classification[235] form the Stern layer, whereas Na^+ and Cl^- merely act as counterions in the diffuse layer.

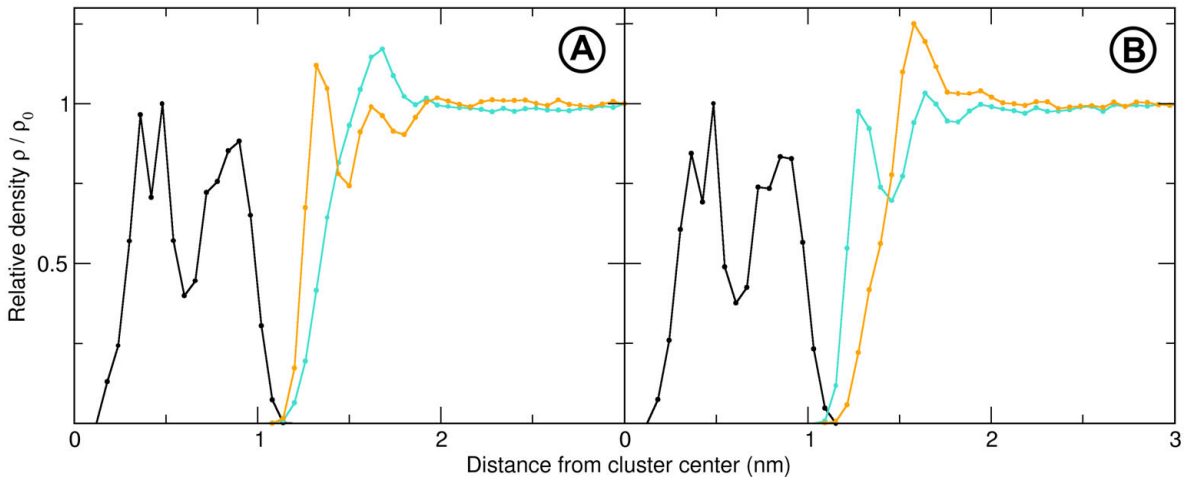

Figure 3.35: Distribution of ions around the COG of a frozen octane aggregate of size 20 in aqueous solution of **A** NaI and **B** LiCl. Octane density is represented in **black**, cations in **turquoise**, and anions in **orange**.

The results can be discussed comprehensibly with the help of snapshots of the analyzed aggregates shown in Figure 3.36. Aside from the micelles, ions within 0.7 nm of the surface are displayed and, in the case of the unbiased system, also the bound ethanol molecules. The difference between the ethanol-free micelle and the octane aggregate is hardly discerned in this static picture, but the latter is added for the sake of completeness. It is, however, obvious that the total number of ions close to the micelle is magnified upon the elimination of ethanol from the system. Moreover, the distribution of ions around the pre-Ouzo aggregate is nonuniform by comparison, with ions only captured in close proximity when next to hydrophobic surface patches free of ethanol. Essentially, interfacial ethanol is screening the greater part of the apolar portion of the aggregate, but as a short-chained alcohol does not itself create sufficient continuous hydrophobic expanse to induce preferential adsorption.

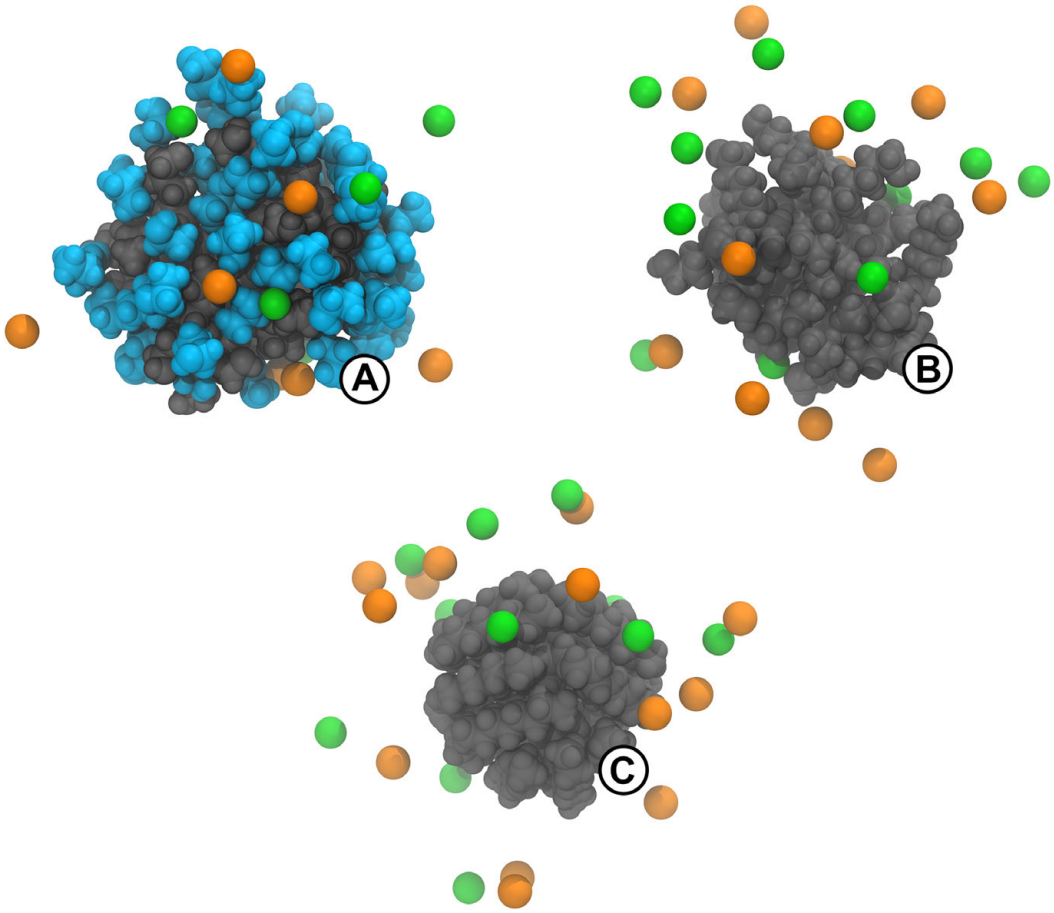

Figure 3.36: Van der Waals representation of **A** an unconstrained octanol micelle in composition α containing NaI, **B** an octanol aggregate with fixed atom positions in aqueous solution of NaI, and **C** a frozen octane aggregate in aqueous solution of NaI. Na^+ and I^- ions within a distance of 0.7 nm from the micelle are displayed as **green** and **orange** spheres, respectively. Octanol and octane are colored **grey** and bound ethanol is depicted in **blue**.

In conclusion, the predominant salt-induced effect is the stabilization of aggregates via the salting out of ethanol from the aqueous phase. Considering how this leads to an even higher interfacial excess of ethanol than already registered in the pure system, the salting out at least partially negates the effects of charge separation. It is further diminished by the patchy surface of octanol micelles, that inherently consist of apolar and polar regions. The observed effects are in line with results from MARCUS et al.[104] who studied pre-Ouzo systems in the presence of Na^+ and Cl^- and reported an increase in correlation lengths for water and octanol against a decrease for ethanol in SAXS measurements.

3.3 Further morphologies

Introductory remark: *This topic is part of the publication in Ref. 236.*

Bicontinuous region Moving along the line separating homogeneous solution and phase separation in the ternary phase diagram to higher octanol concentrations, as illustrated schematically as path **A** in Figure 3.37, the micellar structures described in Section 3.2 vanish. Instead, larger-scale octanol agglomerates of low symmetry form that eventually coalesce to a sponge-like network in composition β, as depicted in Figure 3.38.

This occurrence in itself is not an exclusive property of the investigated system. Even in disregard of any interactions between the components, it is a spatial necessity that continuous, interconnected structures of one constituent emerge when its volume fraction exceeds a certain threshold. This so-called percolation threshold is a well-researched mathematical concept that has been studied in countless model systems ranging from simple 2D lattice sites[237] to interpenetrable hypergeometries in continuous higher-dimensional space.[237,238] However, the percolation problem can only analytically be solved in dimensions $d = 1$ and $d = \infty$ on the Bethe lattice[239] and becomes more complicated when correlations are present in the system.[240] Usually, a numerical approach using Monte Carlo simulations is pursued.

In a crude approximation, the critical volume fraction of particles in a colloidal liquid mixture could be assumed to fall somewhere between that for hard spheres and overlapping spheres in a continuum 3D model. These have been calculated to $\phi_c \approx 0.18-0.19$[241,242] and 0.29,[243] respectively. It has, however, been shown that the value of ϕ_c depends heavily

on the strength of inter-particle interactions in a soft-sphere model with a square-well potential, which drastically increases this range with respect to real systems.[244]

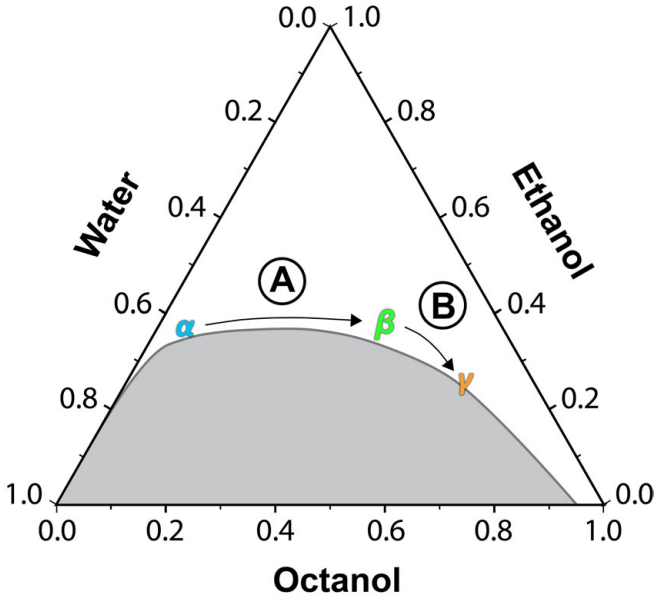

Figure 3.37: Ternary phase diagram of water/ethanol/octanol with marked compositions α, β, and γ. The two-phase region is shaded grey and the monophasic region is blank. Values are given in weight fraction.*

The multitude of correlations in water/ethanol/octanol put a theoretical ascertainment of the percolation threshold well beyond the scope of this work. Nonetheless, principles derived from percolation theory permit reasoning regarding the continuity of the pseudo-phases in the system. Commonly used criteria for the percolation threshold in liquid mixtures are:[201,245,246]

1) the probability of an infinite cluster P_∞ is greater than 50 %,

2) this formation is a fractal object with dimension $d = 2.53$, and

3) the size distribution of aggregates follows a power-law with exponent -2.19.

Within the confines of a finite, although periodically repeated, simulation box, every cluster connected to its periodic image is considered an infinite cluster. In light of this definition, a calculated value of $P_\infty = 1$ in β for octanol clearly signifies the apolar pseudo-phase is well beyond percolation. It further is continuous since this infinite structure is evidently not the result of a macroscopic phase separation, which would manifest as the formation of one single droplet (cf. Section 3.2.1) in the simulation box or a slab-like symmetry, depending on the volume fraction.

*Shape and location of the one- and two-phase region reconstructed from **Figure 1. a)** in Ref. 101.

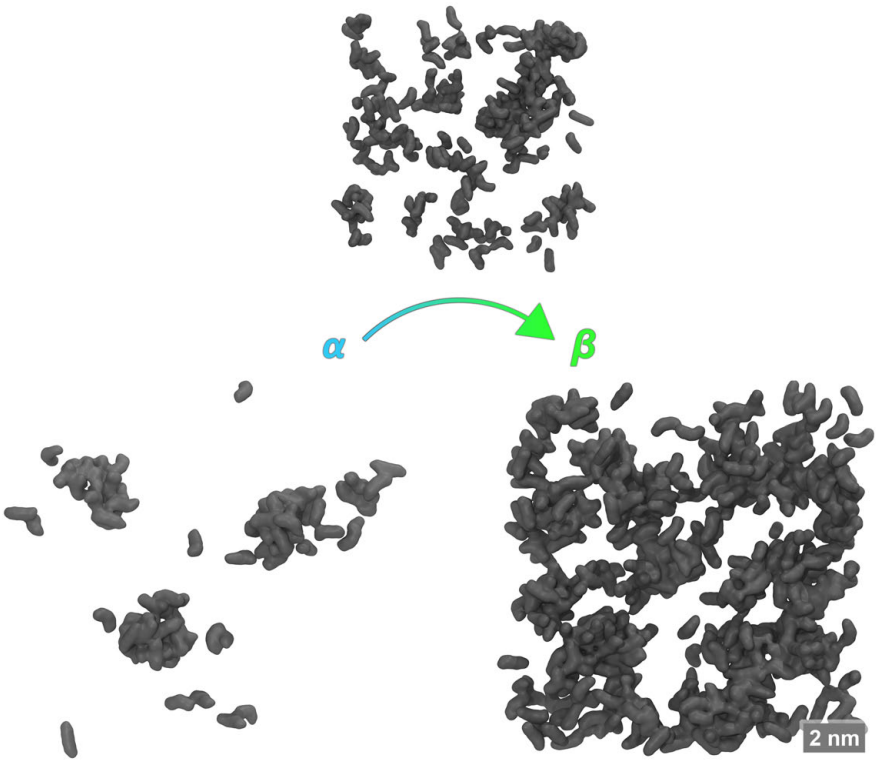

Figure 3.38: Slices of 2 nm thickness through surface representations of the octanol phases in composition α (bottom left), β (bottom right), and an intermediate composition (top).

Figure 3.39 shows equivalent snapshots of ethanol and water in this system. Similar to composition α (cf. Section 3.2.1 / Figure 3.2), ethanol is distributed quite evenly over the polar and apolar pseudo-phases with only marginally decreased density at the very center of the octanol domain. Water constitutes the complement to octanol, filling in the white regions in the snapshot of the organic pseudo-phase and thus, to an extent, a similar network is discernible, yet not nearly as consolidated.

Evaluation of the criteria listed above yields 1) a probability for the infinite water aggregate of close to 90 %, that 2) is of dimensionality $d = 2.78$, and 3) a cluster size distribution obeying a power law with exponent -2.09. Details on the acquisition of 2) and 3) are summarized in Figure 3.40. The dimensionality of the infinite structure is determined by means of the number of molecules inside spherical volumes of radius r centered around an arbitrary point inside the aggregate. In case of a homogeneous distribution of particles, an r^d dependency with dimensionality $d = 3$ would be expected as soon as the volume segments become significantly larger than intermolecular distances. The observed $d = 2.78$ dependency characterizes a porous object well above the theoretical percolation limit.

The power-law fit curve $\mathrm{P}\left(N_{\mathrm{agg}}\right) = 0.67 \cdot N_{\mathrm{agg}}^{-2.09}$ overlaid on the cluster size histogram describes the distribution very well up to sizes of ~ 100. From that point on, the probability

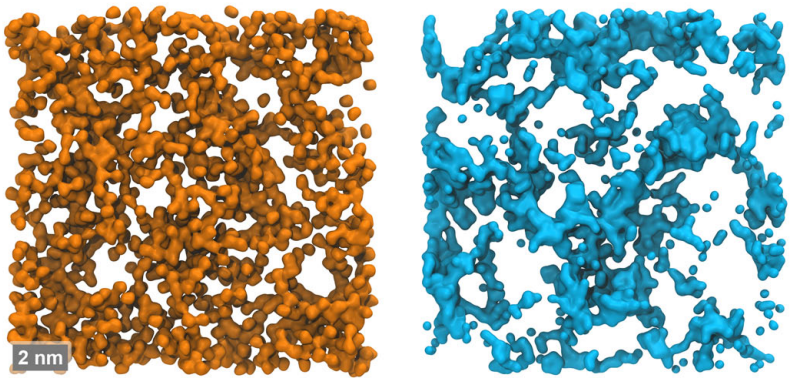

Figure 3.39: Slices of 2 nm thickness through the simulation box of composition β displaying ethanol (**orange**) and water (**blue**) in separate surface representations.

decays faster than the fit and ultimately terminates in a maximum at $N_{\mathrm{Agg}} \approx 6600$. The strict power-law in the first section indicates that the aqueous pseudo-phase is close to a critical point and shows percolation behavior, while the subsequent decline and concluding maximum designate the tendency towards a continuous phase. However, this region is problematic to interpret and exposes a weakness of finite-size, albeit periodic, methods when dealing with spacious structures: both large (technically) finite aggregates surpassing the box dimensions and the true infinite cluster contribute to a condensed probability at the high-N_{agg} limit of the histogram, which is dictated by the box size. For this reason, the high-N_{agg} section of the distribution is disregarded in the fitting process. A second curve with ideal exponent -2.19 is further shown to clarify that in this scheme, the deviation from the determined fit is small enough that with regard to the variance of the data points, it is equally plausible.

Results 1) – 3) uniformly point to an aqueous phase beyond the percolation threshold, characterizing composition β as continuous in octanol as well as water. For the sake of coherency, it should be noted that the stated finite-size limitations are, of course, also true for the algorithm determining the frequency of the "infinite" aggregate to satisfy 1). However, regarding the exceedingly high probability of 90 % alongside the affirmative results for 2) and 3) it is justified to consider this criterion fulfilled.

Reverse aggregation Following the coexistence line into the region of octanol excess (cf. Figure 3.37, path **B**), continuity in the aqueous pseudo-phase eventually breaks into isolated pools of water molecules as depicted in Figure 3.41 alongside snapshots of the octanol pseudo-phase and ethanol. Since the solubility of water in octanol is substantially higher than vice versa and is further increased by ethanol, water is not confined to aggregates as compact as in the pre-Ouzo region. Instead, amorphous agglomerates of

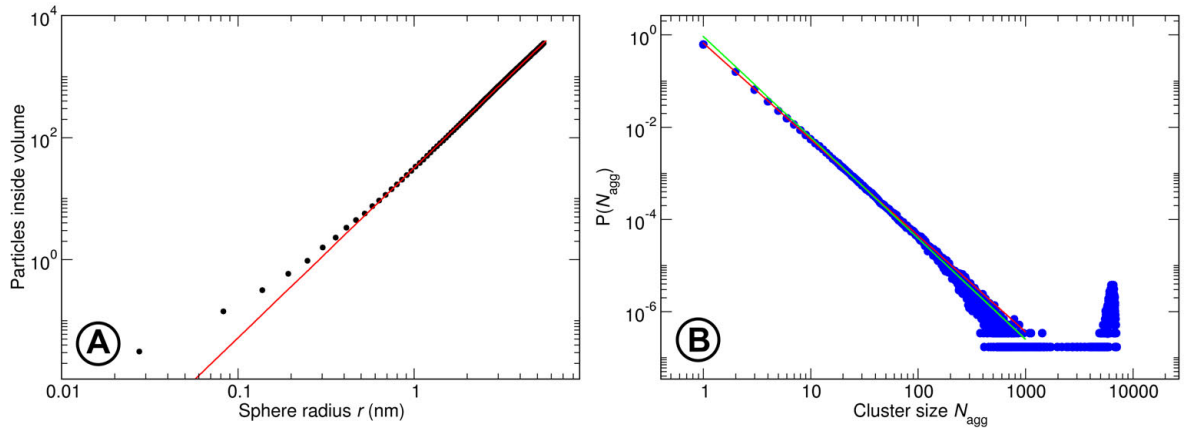

Figure 3.40: A Black dots represent the number of water molecules belonging to the infinite aggregate inside concentrical spherical volumes with radius r. The **red** line traces the power-law function $[Y] = 31.7 \cdot r^{-2.78}$. **B Blue** dots represent the probability to find a water cluster of size N_{agg}. The **red** line shows the potential fit $\mathrm{P}(N_{agg}) = 0.67 \cdot N_{agg}^{-2.09}$, the **green** line $\mathrm{P}(N_{agg}) = 0.93 \cdot N_{agg}^{-2.19}$.

varying size are formed amongst numerous monomers. These aggregates show up as cavities in the octanol phase and the uneven distribution of ethanol molecules leads to assume that the hydrotrope is located at the interface.
Indeed, a cumulative depiction of water and all alcohol oxygen atoms in the system in Figure 3.42 clearly shows that water patches are encompassed by ethanol and octanol hydroxyl groups. Moreover, they are connected among themselves through a hydrogen-bond network of ethanol and octanol hydroxyl groups interspersed with polar regions completely free of oxygen. This picture is an extension of the ordering of hydroxyl groups around and between small pockets of water reported by CHEN and SIEPMANN in wet octanol.[247] Ethanol expands the pool of available hydrogen groups proportional to overall polar volume and thus enables the stability of larger water domains, which therefore are well described as “ethanol swollen” aggregates.

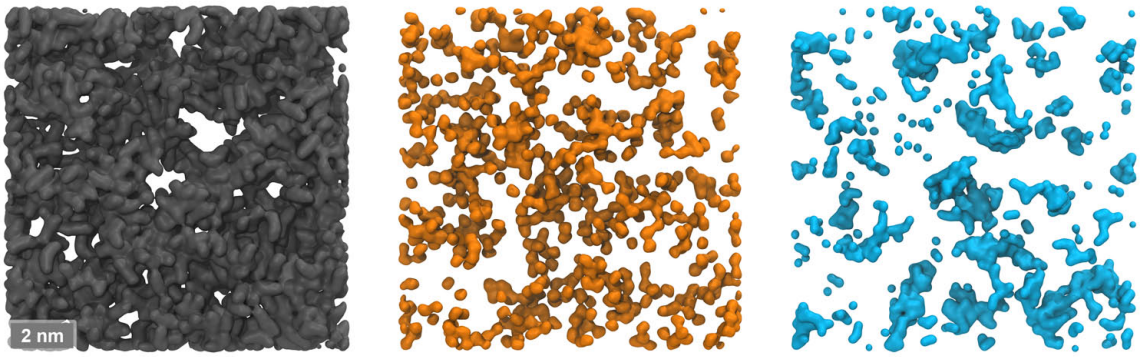

Figure 3.41: Slices of 2 nm thickness through the simulation box of composition γ displaying octanol in **grey**, ethanol in **orange**, and water in **blue** surface representation.

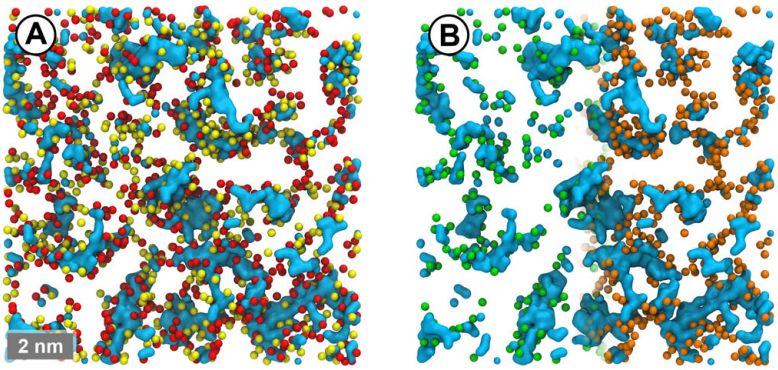

Figure 3.42: A Slice of 2 nm thickness through the simulation box of composition γ displaying water in **blue** surface representation, octanol hydroxyl groups as **yellow**, and ethanol hydroxyl groups as **red** spheres. **B** A version of **A** summarizing all organic hydroxyl groups not connected by at least one mutual hydrogen bond as **green** and the complement as **orange** spheres in a symmetrically subdivided illustration.

These findings conclude the distinct morphologies observed in the monophasic region of water/ethanol/octanol and give rise to the mapping of regimes depicted in Figure 3.43. On the water-rich side, micelle-like octanol aggregates are formed, whereas in excess of octanol secluded water domains emerge. The gap in between is closed by a bicontinuous region, which leads to the same sequence of phases found in classical water/oil/surfactant microemulsions.[248] Structurization is most pronounced in close proximity to the phase boundary and progressively gives way to molecular solution upon dilution with ethanol as signified by color gradients.

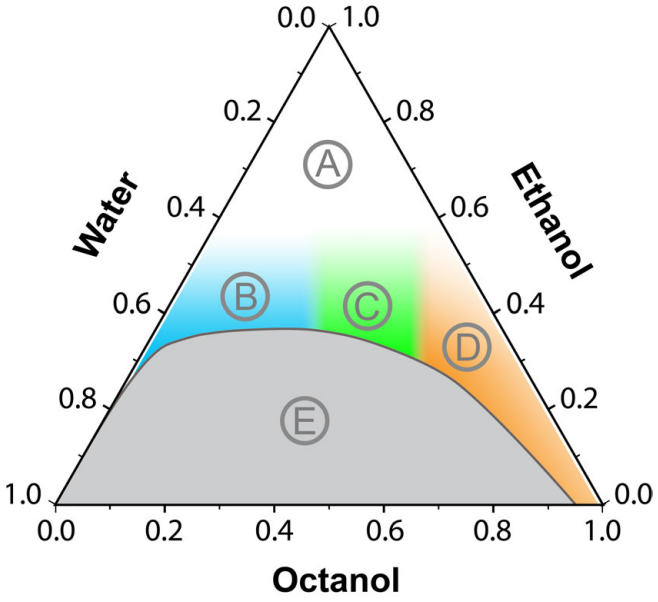

Figure 3.43: Ternary phase diagram of water/ethanol/octanol. The identified morphologies are marked in the graphic, where **A** stands for molecular solution, **B** for oil-in-water microemulsion, **C** for bicontinuous microemulsion, **D** for water-in-oil microemulsion, and **E** for phase separation. The color gradients for the mappings **B**, **C**, and **D** (and therefore implicitly **A**) indicate smooth transitions between regimes.*

*Shape and location of the one- and two-phase region reconstructed from **Figure 1. a)** in Ref. 101.

3.4 Comparison of experimental and calculated X-ray scattering spectra

Introductory remark: *This topic is part of the publication in Ref. 236.*

Since the various forms of nano-ordering in water/ethanol/octanol cannot directly be observed in experiments, MD data is translated into SWAXS spectra (cf. Section 1.2) to establish a common basis. A juxtaposition of the obtained intensities is shown in Figure 3.44 for compositions α, β, and γ. In addition, the graphs of the pure components are hinted at in the MD chart for reference.

The morphologies emerging in these systems entail distinctive features in the scattering signals that blend with entangled signatures originating from characteristic packing of the mixture components. The latter appear as prominent peaks situated in the high-q region of the diagrams. For the system with the highest water content (α), this profile is dominated by a water-specific double-peak discernible between $q = 17\,\mathrm{nm}^{-1}$ and $q = 28\,\mathrm{nm}^{-1}$.[249,250] In the high-octanol regime (γ), by contrast, a single principal peak emerges around $q = 14\,\mathrm{nm}^{-1}$ accompanied by a distinct side maximum close to $q = 3\,\mathrm{nm}^{-1}$. These aspects are typical for aliphatic alcohols as can be seen in the curves for pure ethanol and octanol.[251,252] The low-q part has been mapped to hydroxyl contacts between alcohol groups,[253,254] whereas the larger peak corresponds to the molecular packing of the aliphatic chains.[255,256] Opposed to pure octanol, the hydroxyl peak is amplified and shifted to higher wavelengths. Similar observations have been reported in wet octanol and

were linked to the entrapment of water agglomerates in the hydroxyl network pervading the organic phase.[247]

The curve shape for very small wave vectors below $0.6\,\mathrm{nm}^{-1}$ is implied by the calculated spectra but cannot be resolved due to the restricted box size. Up to that point, however, experimental and theoretic intensities match very well and the practically measured graphs continue to much smaller values of q. In this section, the data of composition β enters a plateau, showing no clear correlation. Resembling profiles have been obtained in the bicontinuous region of systems called "flexible microemulsions".[257]

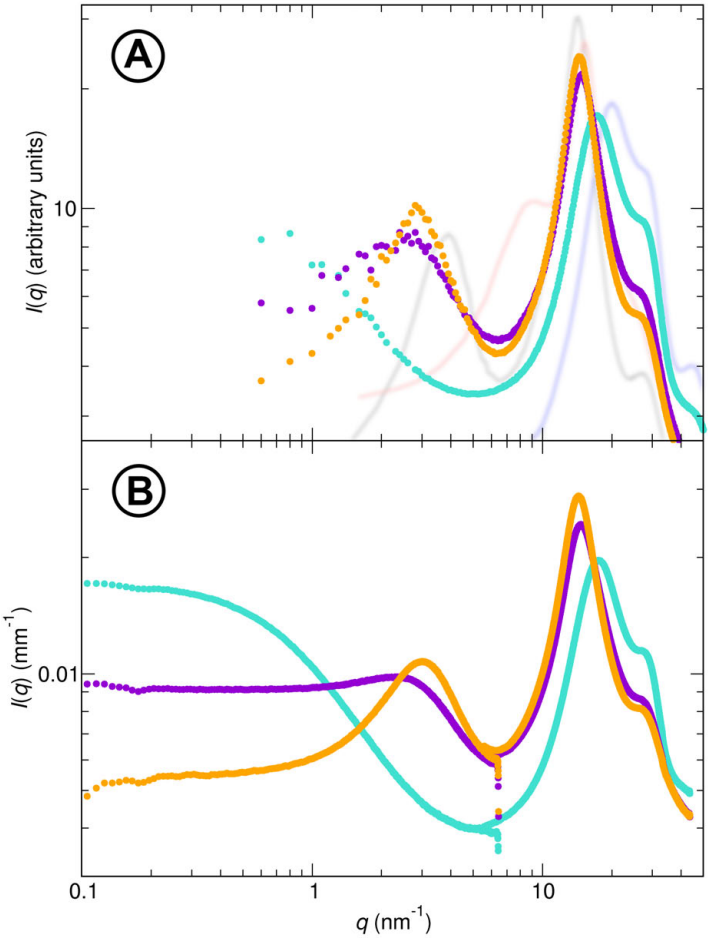

Figure 3.44: X-ray scattering intensities obtained from **A** MD simulations and **B** experimental data*. **Turquoise** dots correspond to composition α, **violet** dots to composition β, and **orange** dots to composition γ. In addition, the SWAXS spectra of the pure components are indicated by means of solid lines in the background of **A** in the following color coding: **octanol**, **ethanol**, **water**.

A substantially different trend is described by the intensities obtained from composition α. Proceeding towards small wave vectors, a steadily increasing signal is recorded, resulting in a signature that is close to that obtained for micelles formed by sodium octanoate.[178,258]

Overall, the spectra derived from the simulation output agree very well with the experimental SWAXS data. Minor differences are to be expected given the simplifications inherent to classical MD simulations and approximations involved in the computation

*Redrawn from **Figure 2. (ii)** in Ref. 236.

of intensities. Nevertheless, accordance of positions as well as patterns of the discussed features uniformly point to equal characteristics of the model systems and the experimental mixtures: the formation of oil-in-water micelles in composition α, the presence bicontinuous structures in composition β, and reverse aggregation in composition γ.

3.5 Outlook: water/propanol/octanol SFME

It has been remarked in the introductory part that incidents of nano-ordering have been reported in a variety of different systems. The next rational step towards a more comprehensive understanding of SFMEs is to incrementally modify the composition of the by now well explored water/ethanol/octanol solutions. In a first variation, to be discussed here, ethanol is interchanged with the next larger aliphatic alcohol propan-1-ol (propanol). In line with the proceedings described in Section 3.2.1, several systems composed of different ratios of the three compounds were tested.

Indeed, at molar fractions of approximately 89 % water and 10 % propanol, signatures of aggregation are observed in the molecule and size distribution histogram of octanol aggregates that is shown in Figure 3.45.

Very similar to the pre-Ouzo case, a wide range of aggregation numbers is observed. Only the first few data points of $\mathrm{P}\left(N_{\mathrm{agg}}\right)$ obey a power-law before it is surmounted by a broad maximum that reaches to almost $N_{\mathrm{agg}} = 200$. Radial analysis around the geometric centers of clusters containing 28 molecules yields the distribution of system components depicted in Figure 3.46.

In analogy to water/ethanol/octanol, only a small amount of water enters the aggregates, but a considerable number of propanol molecules is present inside the structures. The pronounced maximum in the hydrotrope curve points to a sizeable excess concentration close to the interface.

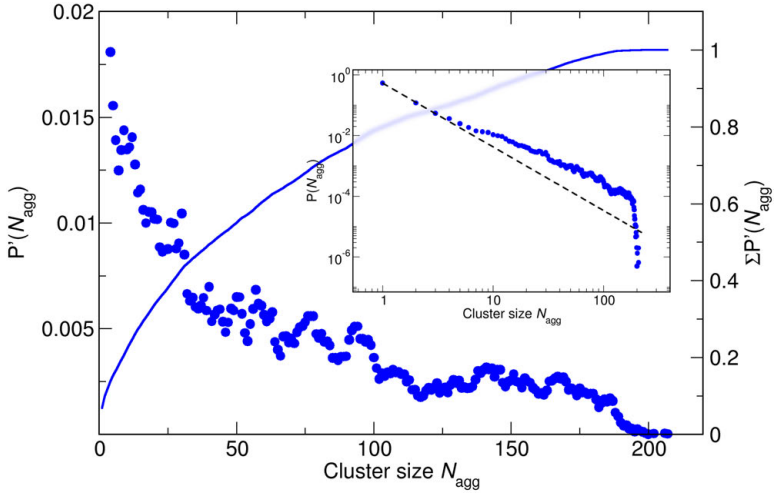

Figure 3.45: Probability to find an octanol molecule in an aggregate of size N_{agg} $P'(N_{agg})$ shown as **blue** dots complemented by a line tracing the running total $\sum P'(N_{agg})$. The inset displays the size distribution of octanol clusters overlaid by a power-law function with exponent -2.1.

Evaluation of the van der Waals interaction of propanol with octanol yields the histogram shown in Figure 3.47. In parallel to the categorization of ethanol into bound and unbound populations discussed in Section 3.2.2, propanol molecules can be separated into two subsets by means of a van der Waals interaction cutoff. The results are supplemented as dashed and dotted lines in the radial distributions and clearly attribute the enhanced surficial propanol density to the bound fraction.

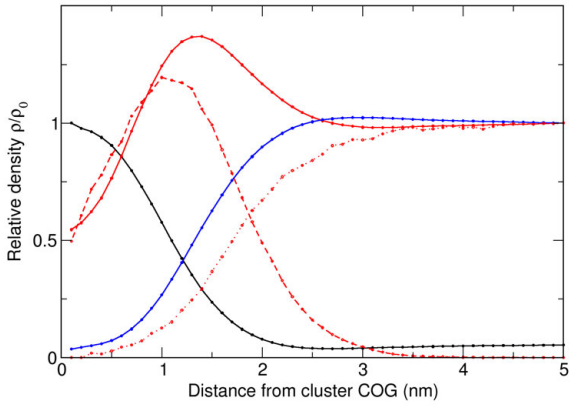

Figure 3.46: Radial distribution of system components around the center of geometry of octanol aggregates containing 28 molecules. Octanol density is colored **black**, propanol density **red**, and water density **blue**. The dashed line corresponds to bound and the dotted line to unbound propanol as determined with an interaction cutoff of -1.8 kJ mol^{-1}.

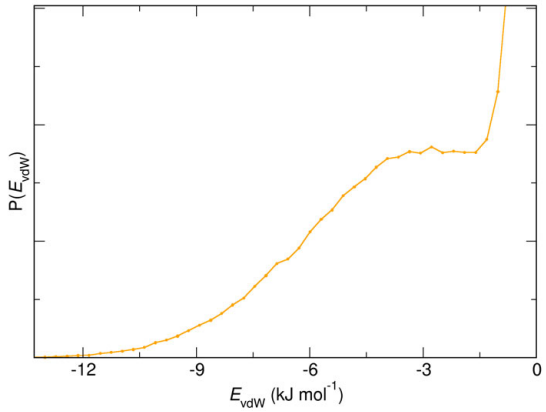

Figure 3.47: Histogram of van der Waals interaction energy E_{vdW} of propanol with octanol.

3.6 Summary

The focus of this chapter was to further progress the characterization of the structurization in the one-phase region of the ouzo-like system water/ethanol/octanol. The initial classification of octanol-rich domains in the pre-Ouzo region as micelle resembling objects was substantiated by numerous considerations. It was shown that the emergence of these aggregates is confined to a specific region of the phase diagram and reinforced that it is neither the result of phase separation nor the consequence of critical fluctuations. The weak aggregation is accompanied by a broad distribution of preferred aggregation numbers, which hints at rapid transformations. Indeed the system is governed by quick rearrangements due to inter-particle collisions and decomposition processes. Specific cluster sizes, however, can be traced over longer time spans than others, that appear only as transient states. The longest living aggregates also constitute the most spherical structures in the ensemble. In general, spherical symmetry decreases with increasing aggregation number up to the point where the formed objects are best described as loose, amorphous agglomerates. In the smallest aggregates, octanol alignment approximates that of surfactant molecules in classical micelles, although in a less rigid variant. Each methyl and methylene group has a preferred radial position in the water-poor interior with the polar head groups oriented towards the solvent. In the transitional zone between octanol-rich and water-rich domains, ethanol concentration is significantly enhanced. The hydrotrope stabilizes the aggregates by forming an interfacial film analogous to surfactant molecules in classical microemulsions.

This oil-in-water SFME displays excellent solubilizing properties of the organic compounds squalene and propane. The solvation free energy for a single propane molecule strongly depends on its location and assumes the most favorable value inside an octanol aggregate. In this region, the solvation free energy agrees well with that determined in a

binary octanol/ethanol mixture. The large squalene molecules, by contrast, contribute significantly to the total amount of nonpolar moieties in the system and thereby entail an interdependent scheme of solvation: the size distribution of clusters is noticeably shifted towards particular aggregation numbers that are large enough to encompass one or more of the C_{30} molecules. This results in the formation of composite structures that do not necessarily resemble the pre-Ouzo micelles, but substantially increase squalene solubility over a binary water/ethanol system.

The addition of the salts NaI and LiCl, by contrast, increases the stability of the pre-Ouzo aggregates through the salting-out of ethanol, which consequently is forced into the oil-rich domains. An additional influence of charge separation on micellization due to preferential adsorption at the interface is very weak due to two factors: a) the aggregate surface is screened by the interfacial ethanol film and is b) not exclusively apolar itself due to surficial accumulation of octanol hydroxyl groups.

Apart from the direct oil-in-water microemulsion, two additional regimes characterized by distinct structurization were identified in the one-phase region of water/ethanol/octanol close to the coexistence line. Elevation of octanol content eventually leads to coalescence of individual aggregates and bicontinuity in octanol as well as water. Ultimately, in excess of octanol, the aqueous pseudo-phase decomposes into spatially separated consolidations, or “reverse aggregates”, that are entangled in a network of ethanol and octanol hydroxyl groups.

3.A Convergence of the aggregate lifetime analysis

In order to assess the reliability of the data presented in Section 3.2.4 / Figure 3.12, the same analysis is performed separately on two equally long and non-overlapping segments of the trajectory. Together, these segments correspond to the part of the trajectory that the original analysis was performed on.

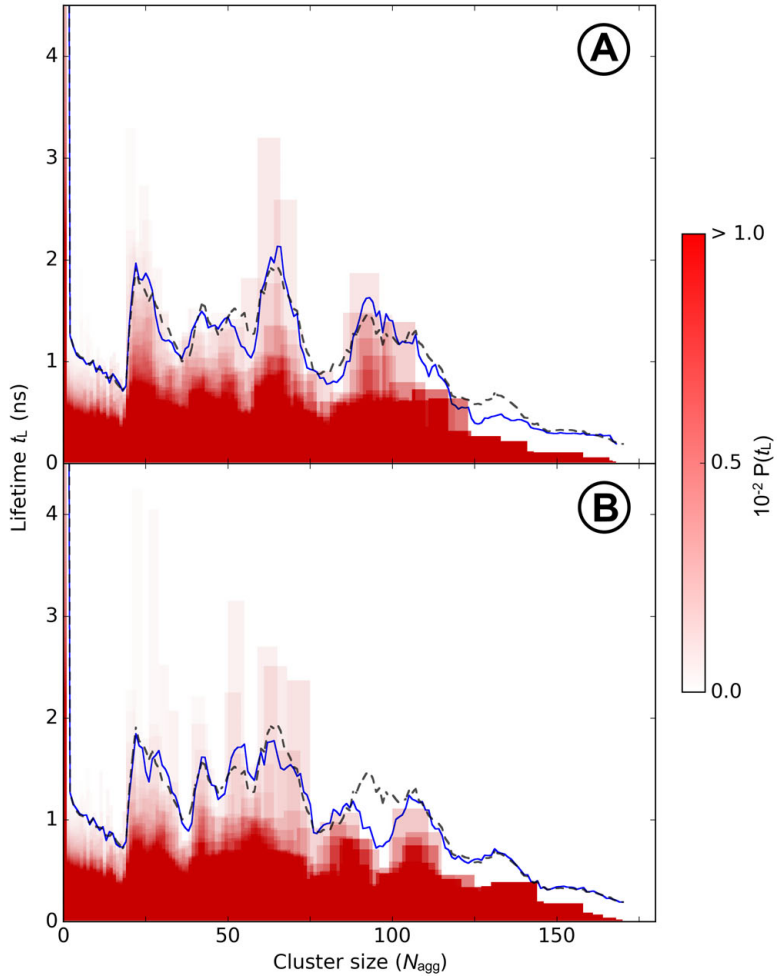

Figure 3.48: Lifetimes t_L of pre-Ouzo aggregates evaluated on two equivalent sections of the trajectory **A** and **B**, represented by colormap plots. The **blue** line traces the average of the respective analysis and the dashed **black** line the cumulative average of **A** and **B**. Both averages are magnified by a factor of 10 for improved visibility.

The results in Figure 3.48 show that characteristic features discussed in the main text persist in both processed sections: an initial decay of the lifetime between $N_{agg} = 2$ and ~ 20, followed by an abrupt increase, and a subsequent minimum close to $N_{agg} = 35$. A

strong signal is again observed in the region of $N_{agg} = 65$, that is delimitated from maxima occurring for $N_{agg} \geqq 90$ by an intermediate minimum close to $N_{agg} = 80$.

Outlook

In this work, a combined study of micellar structures formed in two conceptually different systems was presented. It became evident, that the octanol-rich domains in a surfactant-free ternary mixture of water, ethanol, and octanol share many similarities with the micelles formed by classical ionic surfactant molecules. Need for research remains in both instances, SFMEs and conventional surfactant solutions.

Some of the results hint that not even the particles assembled by the structurally similar cationic and anionic surfactant molecules investigated here are fully comparable. Albeit not gravely, they differ distinctly in internal structure and characteristic contact to the surrounding aqueous medium. In this light it is not unreasonable to suspect that some controversies are owed to the attempt of establishing a general model that unifies this diversified class under one comprehensive description. At this stage, where computer processing power allows for increasingly detailed case studies, some enlightenment can certainly be expected. Not least because classical surfactants represent a lucrative business and are essential in numerous industrial processes and everyday products. An in-depth understanding of the molecular mechanisms allows not only application-specific fine tuning, but also facilitates the targeted identification of alternative compounds in case the employed substances become intolerable under the ever more relevant paradigm of "green chemistry".

A possible principally different alternative may be given by surfactant-free microemulsions formulated from substances that are free from the stigma of environmental or health concerns. Although it is evident that micro-heterogeneities are already common in many

types of surfactant-free solutions, SFMEs are just at the verge of being understood and systematic research is still restricted to a narrow range of model systems. Further research is required to grant a general comprehension of the influence of hydrotrope type and “oil” on the nano-ordering. In addition, solubilization characteristics and simultaneously the sensibility to the added substances must be trialed, since the solute-induced reorganization may not be straightforward to predict in this scheme of weak aggregation.

List of publications

The following research papers were published with the participation of the author during this doctorate:

S. SCHÖTTL, D. TOURAUD, W. KUNZ, T. ZEMB, and D. HORINEK. Consistent Definitions of "The Interface" in Surfactant-free Micellar Aggregates. *Colloids Surfaces A Physiochem. Eng. Asp.*, **480**, 222–227 (**2015**).

T. LOPIAN, S. SCHÖTTL, S. F. PÉVOST, S. PELLET-ROSTAING, D. HORINEK, W. KUNZ, and T. ZEMB. Morphologies Observed in Ultraflexible Microemulsions with and without the Presence of a Strong Acid. *ACS Cent. Sci.*, **2**(7), 467–485 (**2016**).

T. ZEMB, M. KLOSSEK, T. LOPIAN, J. MARCUS, S. SCHÖTTL, D. HORINEK, S. F. PÉVOST, D. TOURAUD, O. DIAT, S. MARČELJA, and W. KUNZ. How to Explain Microemulsions Formed by Solvent Mixtures without Conventional Surfactants. *Proc. Natl. Acad. Sci.*, **113**(16), 4260–4265 (**2016**).

S. SCHÖTTL and D. HORINEK. Aggregation in Detergent-free Ternary Mixtures with Microemulsion-like Properties. *Curr. Opin. Colloid Interface Sci.*, **22**, 8–13 (**2016**).

S. SCHÖTTL and D. HORINEK. Salt Effects in Surfactant-free Microemulsions. *J. Chem. Phys.*, **148**(22), 222818-1–222818-13 (**2018**).

References

[1] W. M. GELBART, A. BEN-SHAUL, and D. ROUX. *Micelles, Membranes, Microemulsions, and Monolayers*, page vi. New York: Springer-Verlag (**1994**).

[2] H. G. LIDELL and R. SCOTT. *A Greek-English Lexicon*, pages 89, 1845–1846, 1939, 1947. Oxford: Clarendon Press (**1940**).

[3] R. ZANA. *Dynamics of Surfactant Self-Assemblies. Micelles, Microemulsions, Vesicles, and Lyotropic Phases*, pages 2–3. Boca Raton: CRC Press (**2005**).

[4] M. J. ROSEN. *Surfactants and Interfacial Phenomena*, chap. 1, page 1. Hoboken: John Wiley & Sons, 3 edn. (**2004**).

[5] T. F. TADROS. *An Introduction to Surfactants*, chap. 2, pages 5–28. Berlin: Walter DeGruyter (**2014**).

[6] J. W. MCBAIN. Colloids and Their Viscosity. Discussion. *Trans. Faraday Soc.*, **9**, 99–101 (**1913**).

[7] J. W. MCBAIN and M. TAYLOR. Zur Kenntnis der Konstitution von Seifen-lösungen: Lösungen von “Natriumpalmitaten”. *Zeitschrift für Phys. Chemie*, **76U**(1), 179–209 (**1911**).

[8] J. W. McBain, E. C. V. Cornish, and R. C. Bowden. CCXV.—Studies of the Constitution of Soap in Solution: Sodium Myristate and Sodium Laurate. *J. Chem. Soc. Trans.*, **101**, 2042–2056 (**1912**).

[9] M. N. Khan. *Micellar Catalysis*, chap. 1, page 1. Boca Raton: CRC Press (**2007**).

[10] E. J. Fendler and S. N. Rosenthal. *Applications of NMR to Micellar Interactions and Catalysis,* in: *Magnetic Resonance in Colloid and Interface Science. Proceedings of a NATO Advanced Study Institute and Second International Symposium held at Menton, France, June 25 – July 7, 1979*, chap. 22, page 354. Dordrecht: D. Reidel (**1980**).

[11] W. C. Presto and W. Preston. Some Correlating Principles of Detergent Action. *J. Phys. Colloid Chem.*, **52**(1), 84–97 (**1948**).

[12] P. Mukerjee and K. J. Mysels. *Critical Micelle Concentrations of Aqueous Surfactant Systems*. Washington, D. C.: National Standard reference data system (**1971**).

[13] G. C. Kresheck. *Aqueous Solutions of Amphiphiles and Macromolecules,* in: *Water. A Comprehensive Treatise,*Vol. 4, chap. 2, page 96. New York: Plenum Press (**1975**).

[14] K. Hess and J. Gundermann. Über die Einwirkung von flüssigem Ammoniak auf Cellulosefaser (Bildung von Ammoniak-Cellulose I, Ammoniak-Cellulose II, und Cellulose III). *Ber. Dtsch. Chem. Ges.*, **40**, 1788–1799 (**1937**).

[15] J. W. McBain and O. A. Hoffman. Lamellar and Other Micelles, and Solubilization by Soaps and Detergents. *J. Phys. Chem.*, **53**(1), 39–55 (**1949**).

[16] R. W. Mattoon, R. S. Stearns, and W. D. Harkins. Structure for Soap Micelles as Indicated by a Previously Unrecognized X-ray Diffraction Band. *J. Chem. Phys.*, **15**(4), 209–210 (**1947**).

[17] P. Debye and E. W. Anacker. Micelle Shape from Dissymmetry Measurements. *J. Phys. Chem.*, **55**(5), 644–655 (**1951**).

[18] G. S. Hartley. State of Solution of Colloidal Electrolytes. *Q. Rev. Chem. Soc.*, **2**, 152–183 (**1948**).

[19] I. Reich. Factors Responsible for the Stability of Detergent Micelles. *J. Phys. Chem.*, **60**(3), 257–262 (**1956**).

[20] J. B. Hayter and J. Penfold. Self-consistent Structural and Dynamic Study of Concentrated Micelle Solutions. *J. Chem. Soc. Faraday*, **77**, 1851–1863 (**1981**).

[21] D. W. Gruen. A Model for the Chains in Amphiphilic Aggregates. 2. Thermodynamic and Experimental Comparisons for Aggregates of Different Shape and Size. *J. Phys. Chem.*, **89**(1), 153–163 (**1985**).

[22] B. CABANE, R. DUPLESSIX, and T. ZEMB. High Resolution Neutron Scattering on Ionic Surfactant Micelles: SDS in Water. *J. Phys.*, **46**(12), 2161–2178 (**1985**).

[23] S.-I. OHNISHI, T. J. R. CYR, and H. FUKUSHIMA. Biradical Spin-Labeled Micelles. *Bull. Chem. Soc. Jpn.*, **43**(3), 673–676 (**1970**).

[24] M. SHINITZKY, A. C. DIANOUX, C. GITLER, and G. WEBER. Microviscosity and Order in the Hydrocarbon Region of Micelles and Membranes Determined with Fluorescent Probes. I. Synthetic Micelles. *Biochemistry*, **10**(11), 2106–2113 (**1971**).

[25] F. M. MENGER and J. M. JERKUNICA. Anisotropic Motion inside a Micelle. *J. Am. Chem. Soc.*, **100**(3), 688–691 (**1978**).

[26] M. J. POVICH, J. A. MANN, and A. KAWAMOTO. ESR Spin Label Study of HDTAB Micelles. *J. Colloid Interface Sci.*, **41**(1), 145–147 (**1972**).

[27] R. C. DORRANCE and T. F. HUNTER. Absorption and Emission Studies of Solubilization in Micelles. Part 1. – Pyrene in Long-chain Cationic Micelles. *J. Chem. Soc. Faraday Trans. 1 Phys. Chem. Condens. Phases*, **68**, 1312–1321 (**1972**).

[28] H. J. POWNALL and L. C. SMITH. Viscosity of the Hydrocarbon Region of Micelles. Measurement by Excimer Fluorescence. *J. Am. Chem. Soc.*, **95**(10), 3136–3140 (**1973**).

[29] F. M. MENGER and D. W. DOLL. On the Structure of Micelles. *J. Am. Chem. Soc.*, **106**(4), 1109–1113 (**1984**).

[30] K. A. DILL and P. J. FLORY. Molecular Organization in Micelles and Vesicles. *Proc. Natl. Acad. Sci.*, **78**(2), 676–680 (**1981**).

[31] P. FROMHERZ. Micelle Structure: A Surfactant-block Model. *Chem. Phys. Lett.*, **77**(3), 460–466 (**1981**).

[32] D. STIGTER. Micelle Formation by Ionic Surfactants. II. Specificity of Head Groups, Micelle Structure. *J. Phys. Chem.*, **78**(24), 2480–2485 (**1974**).

[33] F. M. MENGER, J. M. JERKUNICA, and J. C. JOHNSTON. The Water Content of a Micelle Interior. The Fjord vs. Reef Models. *J. Am. Chem. Soc.*, **100**(15), 4676–4678 (**1978**).

[34] B. SVENS and B. ROSENHOLM. An Investigation of the Size and Structure of the Micelles in Sodium Octanoate Solutions by Small-angle X-ray Scattering. *J. Colloid Interface Sci.*, **44**(3), 495–504 (**1973**).

[35] N. MULLER. Investigation of Micelle Structure by Fluorine Magnetic Resonance. I. Sodium 10,10,10-Trifluorocaprate and Related Compounds. *J. Phys. Chem.*, **71**(4), 957–962 (**1967**).

[36] J. M. CORKILL, J. F. GOODMAN, and T. WALKER. Partial Molar Volumes of Surface-Active Agents in Aqueous Solution. *Trans. Faraday Soc.*, **63**, 768–772 (**1967**).

[37] J. L. KURZ. Effects of Micellization on the Kinetics of the Hydrolysis of Monoalkyl Sulfates. *J. Phys. Chem.*, **66**(11), 2239–2246 (**1962**).

[38] G. C. KRESHECK. *Aqueous Solutions of Amphiphiles and Macromolecules,* in: *Water. A Comprehensive Treatise,*Vol. 4, chap. 2, page 124. New York: Plenum Press (**1975**).

[39] R. C. MURRAY and G. S. HARTLEY. Equilibrium Between Micelles and Simple Ions, with Particular Reference to the Solubility of Long-chain Salts. *Trans. Faraday Soc.*, **31**, 183–189 (**1935**).

[40] M. L. CORRIN. The Effect of Salts and Chain Length on the Critical Concentrations of Colloidal Electrolytes. *J. Colloid Sci.*, **3**(4), 333–338 (**1948**).

[41] J. N. PHILLIPS. The Energetics of Micelle Formation. *Trans. Faraday Soc.*, **51**, 561–569 (**1955**).

[42] B. MATIJEVIĆ, E. PETHICA. The Heats of Micelle Formation of Sodium. *Trans. Faraday Soc.*, **67**, 587–592 (**1957**).

[43] P. ELWORTHY and K. MYSELS. The Surface Tension of SDS Solutions and the Phase Separation Model of Micelle Formation. *J. Colloid Interface Sci.*, **21**(3), 331–347 (**1966**).

[44] C. MINERO and E. PELIZZETTI. The Generalized Pseudophase Model: Treatment of Multiple Equilibria in Micellar Solutions. *Pure Appl. Chem.*, **65**(12), 2573–2582 (**1993**).

[45] G. STAINSBY and E. ALEXANDER. Studies of Soap Solutions. Part II. - Factors Influencing Aggregation in Soap Solutions. *Trans. Faraday Soc.*, **46**, 587–597 (**1950**).

[46] K. SHINODA. The Effect of Chain Length, Salts and Alcohols on the Critical Micelle Concentration. *Bull. Chem. Soc. Jpn.*, **26**(2), 101–105 (**1953**).

[47] K. SHINODA and E. HUTCHINSON. Pseudo-Phase Separation Model for Thermodynamic Calculations on Micellar Solutions. *J. Phys. Chem.*, **66**(4), 577–582 (**1962**).

[48] E. HUTCHINSON, A. INABA, and L. G. BAILEY. A New Interpretation of the Properties of Colloidal Electrolyte Solutions. *Zeitschrift für Phys. Chemie*, **5**, 344–371 (**1955**).

[49] Y. MOROI, N. NISHIKIDO, H. UEHARA, and R. MATUURA. An Interrelationship Between Heat of Micelle Formation and Critical Micelle Concentration. *J. Colloid Interface Sci.*, **50**(2), 254–264 (**1975**).

[50] J. M. CORKILL, J. F. GOODMAN, T. WALKER, and J. WYER. The Multiple Equilibrium Model of Micelle Formation. *Proc. R. Soc. Lond. A. Math. Phys. Sci.*, **312**(1509), 243–255 (**1969**).

[51] T. L. HILL. *Thermodynamics of Small Systems. Two Volumes Bound as One*. New York: Dover Publications (**1994**).

[52] P. DEBYE. Light Scattering in Soap Solutions. *Ann. N. Y. Acad. Sci.*, **51**(4), 575–592 (**1949**).

[53] H. S. FRANK and M. W. EVANS. Free Volume and Entropy in Condensed Systems III. Entropy in Binary Liquid Mixtures; Partial Molal Entropy in Dilute Solutions; Structure and Thermodynamics in Aqueous Electrolytes. *J. Chem. Phys.*, **13**(11), 507–532 (**1945**).

[54] K. W. MILLER and J. H. HILDEBRAND. Solutions of Inert Gases in Water. *J. Am. Chem. Soc.*, **90**(12), 3001–3004 (**1968**).

[55] J. H. HILDEBRAND. A Criticism of the Term "Hydrophobic Bond". *J. Phys. Chem.*, **72**(5), 1841–1842 (**1968**).

[56] K. SHINODA. "Iceberg" formation and solubility. *J. Phys. Chem.*, **81**(13), 1300–1302 (**1977**).

[57] K. SHINODA. Characteristic Property in Aqueous Solutions: Effect of Iceberg Formation of Water Surrounding Solute on the Solubility(or Cmc) and its Peculiar Temperature dependence. *Adv. Colloid Interface Sci.*, **41**, 81–100 (**1992**).

[58] E. RUCKENSTEIN. On the Phenomenological Thermodynamics of Hydrophobic Bonding. *J. Dispers. Sci. Technol.*, **19**(2-3), 329–338 (**1998**).

[59] A. HVIDT. Interactions of Water With Nonpolar Solutes. *Annu. Rev. Biophys. Bioeng.*, **12**(1), 1–20 (**1983**).

[60] T. LAZARIDIS. Solvent Size vs Cohesive Energy as the Origin of Hydrophobicity. *Acc. Chem. Res.*, **34**(12), 931–937 (**2001**).

[61] W. BLOKZIJL and J. B. F. N. ENGBERTS. Hydrophobe Effekte - Ansichten und Tatsachen. *Angew. Chemie*, **105**(11), 1610–1648 (**1993**).

[62] G. HUMMER, S. GARDE, A. E. GARCÍA, A. POHORILLE, and L. R. PRATT. An Information Theory Model of Hydrophobic Interactions. *Proc. Natl. Acad. Sci. U. S. A.*, **93**(17), 8951–8955 (**1996**).

[63] D. CHANDLER. Two Faces of Water. *Nature*, **417**(6888), 491 (**2002**).

[64] M. NISHIO. Myths in Modern Science: The Hydrogen Bond and its Surroundings. Part 2. The Hydrophobic-bond-myth. *Chem-Bio Informatcis J.*, **18**, 10–20 (**2018**).

[65] A. BEN-NAIM. Myths and Verities in Protein Folding Theories: from Frank and Evans Iceberg-conjecture to Explanation of the Hydrophobic Effect. *J. Chem. Phys.*, **139**(16), 165105–1–165105–8 (**2013**).

[66] N. GALAMBA. Water's Structure around Hydrophobic Solutes and the Iceberg Model. *J. Phys. Chem. B*, **117**(7), 2153–2159 (**2013**).

[67] B. KRONBERG. The Hydrophobic Effect. *Curr. Opin. Colloid Interface Sci.*, **22**, 14–22 (**2016**).

[68] A. BIELA, N. N. NASIEF, M. BETZ, A. HEINE, D. HANGAUER, and G. KLEBE. Dissecting the Hydrophobic Effect on the Molecular Level: the Role of Water, Enthalpy, and Entropy in Ligand Binding to Thermolysin. *Angew. Chemie - Int. Ed.*, **52**(6), 1822–1828 (**2013**).

[69] H. B. ROUTH, K. R. BHOWMIK, L. C. PARISH, and J. A. WITKOWSKI. Soaps: from the Phoenicians to the 20th Century–a Historical Review. *Clin. Dermatol.*, **14**(1), 3–6 (**1996**).

[70] K. KOSSWIG. *Surfactants,* in *Ullmann's encyclopedia of industrial chemistry*, chap. 5, pages 445–448. Wiley Online Library (**2000**).

[71] R. J. FARN. *Oxford: Chemistry and Technology of Surfactants*, chap. 1, pages 5–13. Blackwell Publishing (**2006**).

[72] H. WENNERSTRÖM and B. LINDMAN. Micelles. Physical Chemistry of Surfactant Association. *Phys. Rep.*, **52**(1), 1–86 (**1979**).

[73] Y. CHEVALIER and T. ZEMB. The Structure of Micelles and Microemulsions. *Reports Prog. Phys.*, **53**, 279–371 (**1990**).

[74] P. WINSOR. Hydrotropy, Solubilisation and Related Emulsification Processes. Part I-IV. *Trans. Faraday Soc.*, **44**, 376–398 (**1948**).

[75] P. WINSOR. Hydrotropy, Solubilization and Related Emulsification Processes. Part V-VIII. *Trans. Faraday Soc.*, **44**, 451–471 (**1948**).

[76] P. WINSOR. Hydrotropy, Solubilisation and Related Emulsification Processes. Part IX. *Trans. Faraday Soc.*, **46**, 762–772 (**1950**).

[77] P. EKWALL, L. MANDELL, and K. FONTELL. Solubilization in Micelles and Mesophases and the Transition from Normal to Reversed Structures. *Mol. Cryst. Liq. Cryst.*, **8**(1), 157–213 (**1969**).

[78] P. G. DE GENNES and C. TAUPIN. Microemulsions and the Flexibility of Oil/Water Interfaces. *J. Phys. Chem.*, **86**(13), 2294–2304 (**1982**).

[79] L. ARLETH, S. MARČELJA, and T. ZEMB. Gaussian Random Fields with Two Level-cuts – Model for Asymmetric Microemulsions with Nonzero Spontaneous Curvature? *J. Chem. Phys.*, **115**(8), 3923–3936 (**2001**).

[80] B. P. BINKS, J. MEUNIER, and D. LANGEVIN. Characteristic Sizes, Film Rigidity and Interfacial Tensions in Microemulsions Systems. *Trends Colloid Interface Sci. III. Prog. Colloid Polym. Sci.*, **79**, 208–213 (**1989**).

[81] R. STREY. Microemulsion Microstructure and Interfacial Curvature. *Colloid Polym. Sci.*, **272**(8), 1005–1019 (**1994**).

[82] E. RUCKENSTEIN and J. C. CHI. Stability of Microemulsions. *J. Chem. Soc. Faraday Trans. 2*, **71**, 1690–1707 (**1975**).

[83] H. REISS. Entropy-induced Dispersion of Bulk Liquids. *J. Colloid Interface Sci.*, **53**(1), 61–70 (**1975**).

[84] J. T. G. OVERBEEK. The First Rideal Lecture. Microemulsions, A Field at the Border Between Lyophobic and Lyophilic Colloids. *Faraday Discuss. Chem. Soc.*, **65**, 7–19 (**1978**).

[85] J. H. SCHULMAN, W. STOECKENIUS, and L. M. PRINCE. Mechanism of Formation and Structure of Micro Emulsions by Electron Microscopy. *J. Phys. Chem.*, **63**(10), 1677–1680 (**1959**).

[86] T. P. HOAR and J. H. SCHULMAN. Transparent Water-in-oil Dispersions: the Oleopathic Hydro-micelle. *Nature*, **152**(3847), 102–103 (**1943**).

[87] I. DANIELSSON and B. LINDMAN. The Definition of Microemulsion. *Colloids and Surfaces*, **3**(4), 391–392 (**1981**).

[88] S. SLOMKOWSKI, J. V. ALEMÁN, R. G. GILBERT, M. HESS, K. HORIE, R. G. JONES, P. KUBISA, I. MEISEL, W. MORMANN, S. PENCZEK, and R. F. T. STEPTO. Terminology of Polymers and Polymerization Processes in Dispersed Systems (IUPAC Recommendations 2011). *Pure Appl. Chem.*, **83**(12), 2229–2259 (**2011**).

[89] T. G. MASON, J. N. WILKING, K. MELESON, C. B. CHANG, and S. M. GRAVES. Nanoemulsions: Formation, Structure, and Physical Properties. *J. Phys. Condens. Matter*, **18**(41), 635–666 (**2006**).

[90] P. D. I. FLETCHER, B. H. ROBINSON, F. BERMEJO-BARRERA, and D. G. OAKENFULL. *Dynamic Processes in Water-in-oil Microemulsions,* in: *Microemulsions*, page 221. New York: Springer Science+Business Media (**1982**).

[91] H. N. W. LEKKERKERKER, W. K. KEGEL, and J. T. G. OVERBEEK. Phase Behavior of Ionic Microemulsions. *Berichte der Bunsengesellschaft für Phys. Chemie*, **100**(3), 206–217 (**1996**).

[92] S.-Y. CHOI, S.-G. OH, S.-Y. BAE, and S.-K. MOON. Effect of Short-Chain Alcohols as Co-surfactants on Pseudo-ternary Phase Diagrams Containing Lecithin. *Korean J. Chem. Eng.*, **16**(3), 377–381 (**1999**).

[93] S. EZRAHI, A. ASERIN, and N. GARTI. *Aggregation Behavior in One-Phase (Winsor IV) Microemulsion Systems,* in: *Handbook of Microemulsion Science and Technology*, chap. 7, pages 193–205. New York: Marcel Dekker (**1999**).

[94] F. M. MENGER. The Structure of Micelles. *Acc. Chem. Res.*, **12**(4), 111–117 (**1979**).

[95] G. D. SMITH, C. E. DONELAN, and R. E. BARDEN. Oil-continuous Microemulsions Composed of Hexane, Water, and 2-Propanol. *J. Colloid Interface Sci.*, **60**(3), 488–496 (**1977**).

[96] N. F. BORYS, S. L. HOLT, and R. E. BARDEN. Detergentless Water/Oil Microemulsions. *J. Colloid Interface Sci.*, **71**(3), 526–532 (**1979**).

[97] B. A. KEISER, D. VARIE, R. E. BARDEN, and S. L. HOW. Detergentless Water/Oil Microemulsions Composed of Hexane, Water, and 2-Propanol. 2. Nuclear Magnetic Resonance Studies, Effect of Added NaCl. *J. Phys. Chem.*, **83**(10), 1276–1280 (**1979**).

[98] Y. L. KHMELNITSKY. Detergentless Microemulsions - A New Microheterogeneous Medium for Enzymatic Reaction. *Ann. N. Y. Acad. Sci.*, **501**, 161–164 (**1987**).

[99] Y. L. KHMELNITSKY, R. HILHORST, and C. VEEGER. Detergentless Microemulsions as Media for Enzymatic Reactions. Cholesterol Oxidation Catalyzed by Cholesterol Oxidase. *Eur. J. Biochem.*, **176**(2), 265–271 (**1988**).

[100] F. M. MENGER and A. R. ELRINGTON. Organic Reactivity in Microemulsion Systems. *J. Am. Chem. Soc.*, **113**(25), 9621–9624 (**1991**).

[101] M. L. KLOSSEK, D. TOURAUD, T. ZEMB, and W. KUNZ. Structure and Solubility in Surfactant-free Microemulsions. *Chemphyschem*, **13**(18), 4116–4119 (**2012**).

[102] S. A. VITALE and J. L. KATZ. Liquid Droplet Dispersions Formed by Homogeneous Liquid-liquid Nucleation: "The Ouzo Effect". *Langmuir*, **19**(10), 4105–4110 (**2003**).

[103] M. L. KLOSSEK, D. TOURAUD, and W. KUNZ. Eco-solvents–cluster-formation, Surfactantless Microemulsions and Facilitated Hydrotropy. *Phys. Chem. Chem. Phys.*, **15**(26), 10971–10977 (**2013**).

[104] J. MARCUS, D. TOURAUD, S. F. PRÉVOST, O. DIAT, T. ZEMB, and W. KUNZ. Influence of Additives on the Structure of Surfactant-free Microemulsions. *Phys. Chem. Chem. Phys.*, **17**(48), 32528–32538 (**2015**).

[105] A. LUCIA, P. G. ARGUDO, E. GUZMÁN, R. G. RUBIO, and F. ORTEGA. Formation of Surfactant Free Microemulsions in the Ternary System Water/Eugenol/Ethanol. *Colloids Surfaces A Physicochem. Eng. Asp.*, **521**, 133–140 (**2017**).

[106] J. MARCUS, M. L. KLOSSEK, D. TOURAUD, and W. KUNZ. Nano-droplet Formation in Fragrance Tinctures. *Flavour Fragr. J.*, **28**(5), 294–299 (**2013**).

[107] J. MARCUS, M. MÜLLER, J. NISTLER, D. TOURAUD, and W. KUNZ. Nano-droplet formation in Water/Ethanol or Isopropanol/Mosquito Repellent Formulations. *Colloids Surfaces A Physicochem. Eng. Asp.*, **458**(1), 3–9 (**2014**).

[108] V. TCHAKALOVA, T. ZEMB, and D. BENCZÉDI. Evaporation Triggered Self-assembly in Aqueous Fragrance-ethanol Mixtures and its Impact on Fragrance Performance. *Colloids Surfaces A Physicochem. Eng. Asp.*, **460**, 414–421 (**2014**).

[109] M. ZOUMPANIOTI, M. KARALI, A. XENAKIS, and H. STAMATIS. Lipase Biocatalytic Processes in Surfactant Free Microemulsion-like Ternary Systems and Related Organogels. *Enzyme Microb. Technol.*, **39**(4), 531–539 (**2006**).

[110] M. ZOUMPANIOTI, H. STAMATIS, V. PAPADIMITRIOU, and A. XENAKIS. Spectroscopic and Catalytic Studies of Lipases in Ternary Hexane-1-propanol-water Surfactantless Microemulsion Systems. *Colloids Surfaces B Biointerfaces*, **47**(1), 1–9 (**2006**).

[111] A. XENAKIS, M. ZOUMPANIOTI, and H. STAMATIS. Enzymatic Reactions in Structured Surfactant-free Microemulsions. *Curr. Opin. Colloid Interface Sci.*, **22**, 41–45 (**2016**).

[112] O. DIAT, M. L. KLOSSEK, D. TOURAUD, B. DEME, I. GRILLO, W. KUNZ, and T. ZEMB. Octanol-rich and Water-rich Domains in Dynamic Equilibrium in the Pre-ouzo Region of Ternary Systems Containing a Hydrotrope. *J. Appl. Crystallogr.*, **46**(6), 1665–1669 (**2013**).

[113] P. BOŠKOVIĆ, V. SOKOL, T. ZEMB, D. TOURAUD, and W. KUNZ. Weak Micelle-Like Aggregation in Ternary Liquid Mixtures as Revealed by Conductivity, Surface Tension, and Light Scattering. *J. Phys. Chem. B*, **119**(30), 9933–9939 (**2015**).

[114] S. SCHÖTTL, J. MARCUS, O. DIAT, D. TOURAUD, W. KUNZ, T. ZEMB, and D. HORINEK. Emergence of Surfactant-free Micelles from Ternary Solutions. *Chem. Sci.*, **5**(8), 2949–2954 (**2014**).

[115] T. N. ZEMB, M. KLOSSEK, T. LOPIAN, J. MARCUS, S. SCHÖTTL, D. HORINEK, S. F. PRÉVOST, D. TOURAUD, O. DIAT, S. MARČELJA, and W. KUNZ. How to Explain Microemulsions Formed by Solvent Mixtures without Conventional Surfactants. *Proc. Natl. Acad. Sci.*, **113**(16), 4260–4265 (**2016**).

[116] S. SCHÖTTL. *Emergence of Micelles in Ternary Solutions without Surfactants*. Master's thesis, Universität Regensburg (**2013**).

[117] W. M. GELBART, A. BEN-SHAUL, and D. ROUX. *Micelles, Membranes, Microemulsions, and Monolayers*, page ix. New York: Springer-Verlag (**1994**).

[118] W. M. GELBART and A. BEN-SHAUL. *Statistical Thermodynamics of Amphiphile Self-Assembly: Structure and Phase Transitions in Micellar Solutions,* in: *Micelles, Membranes, Microemulsions, and Monolayers*, chap. 1, pages 1–104. New York: Springer-Verlag (**1994**).

[119] D. BALASUBRAMANIAN, V. SRINIVAS, V. G. GAIKAR, and M. M. SHARMA. Aggregation Behavior of Hydrotropic Compounds in Aqueous Solution. *J. Phys. Chem.*, **93**(9), 3865–3870 (**1989**).

[120] J. Y. KIM, S. KIM, M. PAPP, K. PARK, and R. PINAL. Hydrotropic Solubilization of Poorly Water-Soluble Drugs. *J. Pharm. Sci.*, **99**(9), 3959–3965 (**2010**).

[121] V. SRINIVAS, G. RODLEY, and K. RAVIKUMAR. Molecular Organization in Hydrotrope Assemblies. *Langmuir*, **13**(12), 3235–3239 (**1997**).

[122] K. NIDHI, S. INDRAJEET, M. KHUSHBOO, K. GAURI, and J. SEN, DHRUBO. Hydrotropy: A Promising Tool for Solubility Enhancement: A Review. *Int. J. Drug Dev. Res.*, **3**(2), 26–33 (**2011**).

[123] V. SAMPATH KUMAR, C. RAJA, and C. JAYAKUMAR. A Review on Solubility Enhancement Using Hydrotropic Phenomena. *Int. J. Pharm. Pharm. Sci.*, **6**(6), 1–7 (**2014**).

[124] W. KUNZ, K. HOLMBERG, and T. ZEMB. Hydrotropes. *Curr. Opin. Colloid Interface Sci.*, **22**, 99–107 (**2016**).

[125] J. J. BOOTH, S. ABBOTT, and S. SHIMIZU. Mechanism of Hydrophobic Drug Solubilization by Small Molecule Hydrotropes. *J. Phys. Chem. B*, **116**(51), 14915–14921 (**2012**).

[126] J. J. BOOTH, M. OMAR, S. ABBOTT, and S. SHIMIZU. Hydrotrope Accumulation around the Drug: the Driving Force for Solubilization and Minimum Hydrotrope Concentration for Nicotinamide and Urea. *Phys. Chem. Chem. Phys.*, **17**(12), 8028–8037 (**2015**).

[127] S. SHIMIZU, J. J. BOOTH, and S. ABBOTT. Hydrotropy: Binding Models vs. Statistical Thermodynamics. *Phys. Chem. Chem. Phys.*, **15**(47), 20625–20632 (**2013**).

[128] S. PRONK, S. PÁLL, R. SCHULZ, P. LARSSON, P. BJELKMAR, R. APOSTOLOV, M. R. SHIRTS, J. C. SMITH, P. M. KASSON, D. VAN DER SPOEL, B. HESS, and E. LINDAHL. GROMACS 4.5: A High-throughput and Highly Parallel Open Source Molecular Simulation Toolkit. *Bioinformatics*, **29**(7), 845–854 (**2013**).

[129] L. MARTÍNEZ, R. ANDRADE, E. G. BIRGIN, and J. M. MARTÍNEZ. Packmol: A Package for Building Initial Configurations for Molecular Dynamics Simulations. *J. Comput. Chem.*, **30**(13), 2157–2164 (**2009**).

[130] K. A. FEENSTRA, B. HESS, and H. J. C. BERENDSEN. Improving Efficiency of Large Time-scale Molecular Dynamics Simulations of Hydrogen-rich Systems. *J. Comput. Chem.*, **20**(8), 786–798 (**1999**).

[131] U. ESSMANN, L. PERERA, M. L. BERKOWITZ, T. DARDEN, H. LEE, and L. G. PEDERSEN. A Smooth Particle Mesh Ewald Method. *J. Chem. Phys.*, **103**(19), 8577–8593 (**1995**).

[132] M. PARRINELLO and A. RAHMAN. Polymorphic Transitions in Single Crystals: a New Molecular Dynamics Method. *J. Appl. Phys.*, **52**(12), 7182–7190 (**1981**).

[133] J. L. F. ABASCAL and C. VEGA. A General Purpose Model for the Condensed Phases of Water: TIP4P/2005. *J. Chem. Phys.*, **123**(23), 234505–1–234505–12 (**2005**).

[134] W. L. JORGENSEN, D. S. MAXWELL, and J. TIRADO-RIVES. Development and Testing of the OPLS All-atom Force Field on Conformational Energetics and Properties of Organic Liquids. *J. Am. Chem. Soc.*, **118**(45), 11225–11236 (**1996**).

[135] S. W. I. SIU, K. PLUHACKOVA, and R. A. BÖCKMANN. Optimization of the OPLS-AA Force Field for Long Hydrocarbons. *J. Chem. Theory Comput.*, **8**(4), 1459–1470 (**2012**).

[136] H. J. BERENDSEN, J. P. POSTMA, W. F. VAN GUNSTEREN, A. DINOLA, and J. R. HAAK. Molecular Dynamics with Coupling to an External Bath. *J. Chem. Phys.*, **81**(8), 3684–3690 (**1984**).

[137] D. HORINEK, S. I. MAMATKULOV, and R. R. NETZ. Rational Design of Ion Force Fields Based on Thermodynamic Solvation Properties. *J. Chem. Phys.*, **130**, 1–21 (**2009**).

[138] J. D. RIO, G. PRIETO, F. SARMIENTO, and V. MOSQUERA. Thermodynamics of Micellization of n-Octyltrimethylammonium Bromide in Different Media. *Langmuir*, **11**(8610), 1511–1514 (**1995**).

[139] G. D'ERRICO, O. ORTONA, L. PADUANO, A. TEDESCHI, and V. VITAGLIANO. Mixed Micellar Aggregates of Cationic and Nonionic Surfactants with Short Hydrophobic Tails. An Intradiffusion Study. *Phys. Chem. Chem. Phys.*, **4**(21), 5317–5324 (**2002**).

[140] E. JUNQUERA, E. AICART, and G. TARDAJOS. Inclusional Complexes of Decyltrimethylammonium Bromide and b-Cyclodextrin in Water. *J. Phys. Chem.*, **96**(11), 4533–4537 (**1992**).

[141] N. YOSHIDA, K. MATSUOKA, and Y. MOROI. Micelle Formation of n-Decyltrimethylammonium Perfluorocarboxylates. *J. Colloid Interface Sci.*, **187**, 388–395 (**1997**).

[142] M. A. BAHRI, M. HOEBEKE, A. GRAMMENOS, L. DELANAYE, N. VANDEWALLE, and A. SERET. Investigation of SDS, DTAB and CTAB Micelle Microviscosities by Electron Spin Resonance. *Colloids Surfaces A Physicochem. Eng. Asp.*, **290**, 206–212 (**2006**).

[143] W. BRUNING and A. HOLTZER. The Effect of Urea on Hydrophobic Bonds: The Critical Micelle Concentration of n-Dodecyltrimethylammonium Bromide in Aqueous Solutions of Urea. *J. Am. Chem. Soc.*, **83**(23), 4865–4866 (**1961**).

[144] K. L. HERRINGTON, E. W. KALER, D. D. MILLER, J. A. N. ZASADZINSKI, and S. CHIRUVOLU. Phase Behavior of Aqueous Mixtures of Dodecyltrimethylammonium Bromide (DTAB) and Sodium Dodecyl Sulfate (SDS). *J. Phys. Chem.*, **97**, 13792–13802 (**1993**).

[145] A. MALLIARIS and J. L. MOIGNE. Temperature Dependence of the Micelle Aggregation Number and Rate of Intramicellar Excimer Formation in Aqueous Surfactant Solutions. *J. Phys. Chem.*, **89**, 2709–2713 (**1985**).

[146] P. EKWALL, H. EIKREM, and L. MANDELL. The Properties and Structures of Aqueous Sodium Caprylate Solutions I. *Acta Chem. Scand.*, **17**, 111–122 (**1963**).

[147] T. DRAKENBERG and B. LINDMAN. 13C NMR of Micellar Solutions. *J. Colloid Interface Sci.*, **44**(1), 184–186 (**1973**).

[148] T. NAMANI and P. WALDE. From Decanoate Micelles to Decanoic Acid / Dodecylbenzenesulfonate Vesicles. *Langmuir*, **21**(14), 6210–6219 (**2005**).

[149] F. E. STANLEY, A. M. WARNER, E. SCHNEIDERMAN, and A. M. STALCUP. Rapid Determination of Surfactant Critical Micelle Concentrations Using Pressure-driven Flow with Capillary Electrophoresis Instrumentation. *J. Chromatogr. A*, **1216**(47), 8431–8434 (**2009**).

[150] L. X. DANG. Development of Nonadditive Intermolecular Potentials Using Molecular Dynamics: Solvation of Li^+ and F^- ions in Water. *J. Chem. Phys.*, **97**(2), 1614–1614 (**1992**).

[151] L. X. DANG and B. C. GARRETT. Photoelectron Spectra of the Hydrated Iodine Anion from Molecular Dynamics Simulations. *J. Chem. Phys.*, **99**(4), 2972–2977 (**1993**).

[152] L. X. DANG. Mechanism and Thermodynamics of Ion Selectivity in Aqueous Solutions of 18-Crown-6 Ether: A Molecular Dynamics Study. *J. Am. Chem. Soc.*, **117**(26), 6954–6960 (**1995**).

[153] M. E. LEE and N. F. VAN DER VEGT. A New Force Field for Atomistic Simulations of Aqueous Tertiary Butanol Solutions. *J. Chem. Phys.*, **122**(11), 0–13 (**2005**).

[154] H. J. C. BERENDSEN, J. R. GRIGERA, and T. P. STRAATSMA. The Missing Term in Effective Pair Potentials. *J. Phys. Chem*, **91**(24), 6269–6271 (**1987**).

[155] W. H. PRESS, S. A. TEUKOLSKY, W. T. VETTERLING, and B. P. FLANNERY. *Numerical Recipes in C (2nd ed.)*, pages 467–468. Cambridge: Press Syndicate of the University of Cambridge (**2002**).

[156] B. GÄRTNER. *Fast and Robust Smallest Enclosing Balls,* in: *Proc. 7th Annual European Symposium on Algorithms (ESA), Lecture Notes in Computer Science 1643*, pages 325–338. Springer Verlag (**1999**).

[157] E. JONES, T. OLIPHANT, P. PETERSON, ET AL. SciPy: Open Source Scientific Tools for Python (**2001–**). URL: http://www.scipy.org/ [Online; accessed 04/14/2018].

[158] S. SAKURABA and N. MATUBAYASI. ERmod: Fast and Versatile Computation Software for Solvation Free Energy with Approximate Theory of Solutions. *J. Comput. Chem.*, **35**(21), 1592–1608 (**2014**).

[159] N. MATUBAYASI and M. NAKAHARA. Theory of Solutions in the Energetic Representation. I. Formulation. *J. Chem. Phys.*, **113**(15), 6070–6081 (**2000**).

[160] N. MATUBAYASI and M. NAKAHARA. Theory of Solutions in the Energy Representation II. Functional for the Chemical Potential. *J. Chem. Phys.*, **117**(8), 3605–3616 (**2002**).

[161] N. MATUBAYASI and M. NAKAHARA. Erratum: Theory of Solutions in the Energy Representation II. Functional for the Chemical Potential (J. Chem. Phys. (2002) 117 (3605)). *J. Chem. Phys.*, **118**(5), 2446 (**2003**).

[162] K. HINSEN, E. PELLEGRINI, S. STACHURA, and G. R. KNELLER. NMoldyn 3: Using Task Farming for a Parallel Spectroscopy-oriented Analysis of Molecular Dynamics Simulations. *J. Comput. Chem.*, **33**(25), 2043–2048 (**2012**).

[163] D. CHANDLER. *Introduction to Modern Statistical Mechanics*, page 208. Oxford University Press (**1987**).

[164] V. CALANDRINI, P. CALLIGARI, K. HINSEN, and G. R. KNELLER. *nMoldyn: User's Guide*. Institut Laue-Langevin, 6, rue Jules Horowitz BP156, 38042 Grenoble, Cedex 9, France (**2006**).

[165] P. J. BROWN, A. G. FOX, E. N. MASLEN, M. A. O'KEEFE, and B. T. M. WILLIS. *Intensity of Diffracted Intensities,* in: *International Tables for Crystallography,* Vol. C*, Mathematical, Physical and Chemical Tables*, pages 554 – 595. Dordrecht: Kluwer Academic Publishers, 3 edn. (**2004**).

[166] V. CALANDRINI, E. PELLEGRINI, P. CALLIGARI, K. HINSEN, and G. R. KNELLER. nMoldyn-Interfacing Spectroscopic Experiments, Molecular Dynamics Simulations and Models for Time Correlation Functions. *Collect. SFN*, **12**, 201–232 (**2011**).

[167] D. S. SIVIA. *Elementary Scattering Theory*, page 118. Oxford: Oxford University Press (**2011**).

[168] R. MCGILL, J. W. TUKEY, and W. A. LARSEN. Variations of Box Plots. *Am. Stat.*, **32**(1), 12–16 (**1978**).

[169] M. FRIGGE, D. C. HOAGLIN, and B. IGLEWICZ. Some Implementations of the Boxplots. *Am. Stat.*, **43**(1), 50–54 (**1989**).

[170] J. W. TUKEY. *Exploratory Data Analysis: Past, Present, and Future*, page 11. Princeton: Department of Statistics, Princeton University (**1993**).

[171] C. TANFORD. Micelle Shape and Size. *J. Phys. Chem.*, **76**(1), 3020–3024 (**1972**).

[172] H. WENNERSTRÖM and B. LINDMAN. Water Penetration into Surfactant Micelles. *J. Phys. Chem.*, **83**(22), 2931–2932 (**1979**).

[173] H. WADELL. Volume, Shape, and Roundness of Rock Particles. *J. Geol.*, **40**(5), 443–451 (**1932**).

[174] H. EDELSBRUNNER, D. G. KIRKPATRICK, and R. SEIDEL. On the Shape of a Set of Points in the Plane. *IEEE Trans. Inf. Theory*, **29**(4), 551–559 (**1983**).

[175] A. GALTON and M. DUCKHAM. *What is the Region Occupied by a Set of Points?* in: *International Conference on Geographic Information Science*, pages 81–98. Berlin: Springer Verlag (**2006**).

[176] A. MOREIRA and M. Y. SANTOS. Concave Hull: A k-Nearest Neighbours Approach for the Computation of the Region Occupied by a Set of Points. *Proc. 2nd Int. Conf. Comput. Graph. Theory Appl. (GRAPP 2007), Barcelona, Spain*, pages 61–68 (**2006**).

[177] E. MEEKS, J. DAVIES, G. AISCH, and I. JOHNSON. d3.geom.concaveHull (**2015**). GitHub repository, URL: https://github.com/emeeks/d3.geom.concaveHull [Online; accessed 04/14/2018].

[178] J. HAYTER and T. ZEMB. Concentration-dependent Structure of Sodium Octanoate Micelles. *Chem. Phys. Lett.*, **93**(I), 91–94 (**1982**).

[179] R. HARGREAVES, D. T. BOWRON, and K. EDLER. Atomistic Structure of a Micelle in Solution Determined by Wide Q-Range Neutron Diffraction. *J. Am. Chem. Soc.*, **133**(41), 16524–16536 (**2011**).

[180] S. LEBECQUE, J. M. CROWET, M. N. NASIR, M. DELEU, and L. LINS. Molecular Dynamics Study of Micelles Properties According to Their Size. *J. Mol. Graph. Model.*, **72**, 6–15 (**2017**).

[181] R. NAGARAJAN. Molecular Packing Parameter and Surfactant Self-assembly: the Neglected Role of the Surfactant Tail. *Langmuir*, **18**(1), 31–38 (**2002**).

[182] B. CABANE. Structure of the Water/Surfactant Interface in Micelles: an NMR Study of SDS Micelles Labelled with Paramagnetic Ions. *J. Phys.*, **42**, 847–859 (**1981**).

[183] D. BENDEDOUCH, S.-H. CHEN, and W. C. KOEHLER. Structure of Ionic Micelles from Small Angle Neutron Scattering. *J. Phys. Chem.*, **87**(1), 153–159 (**1983**).

[184] B. AOUN, V. K. SHARMA, E. PELLEGRINI, S. MITRA, M. JOHNSON, and R. MUKHOPADHYAY. Structure and Dynamics of Ionic Micelles: MD Simulation and Neutron Scattering Study. *J. Phys. Chem. B*, **119**(15), 5079–5086 (**2015**).

[185] D. LANGEVIN. Micelles and Microemulsions. *Annu. Rev. Phys. Chem*, **43**, 341–369 (**1992**).

[186] J. B. ROSENHOLM, K. LARSSON, and N. DINH-NGUYEN. A Raman Spectroscopy Study of Micellar Structures in Ternary Systems of Water-sodium Octanoate-pentanol/Decanol. *Colloid Polym. Sci.*, **255**(11), 1098–1109 (**1977**).

[187] Y. CHEVALIER and C. CHACHATY. NMR Investigation of the Micellar Properties of Monoalkylphoshpates. *Colloid Polym. Sci.*, **262**(6), 489–496 (**1984**).

[188] K. WATANABE, M. FERRARIO, and M. L. KLEIN. Molecular Dynamics Study of a Sodium Octanoate Micelle in Aqueous Solution. *J. Phys. Chem.*, **92**(3), 819–821 (**1988**).

[189] B. LEE and F. M. RICHARDS. The Interpretation of Protein Structures: Estimation of Static Accessibility. *J. Mol. Biol.*, **55**(3), 379–400 (**1971**).

[190] A. BONDI. Van der Waals Volumes and Radii. *J. Phys. Chem.*, **68**(3), 441–451 (**1964**).

[191] S. PAL, B. BAGCHI, and S. BALASUBRAMANIAN. Hydration Layer of a Cationic Micelle, C10TAB: Structure, Rigidity, Slow Reorientation, Hydrogen Bond Lifetime, and Solvation Dynamics. *J. Phys. Chem. B*, **109**(26), 12879–12890 (**2005**).

[192] E. A. G. ANIANSSON and S. N. WALL. On the Kinetics of Step-Wise Micelle Association. *J. Phys. Chem.*, **78**(10), 1024–1030 (**1974**).

[193] E. A. G. ANIANSSON and S. N. WALL. Kinetics of Step-wise Micelle Association. Correction and Improvement. *J. Phys. Chem.*, **79**(8), 857–858 (**1975**).

[194] M. ALMGREN and E. A. G. ANIANSSON. The Kinetics of Redistribution of Micellar Sizes. *Chem. Phys.*, **19**, 1–16 (**1977**).

[195] S. N. WALL and G. E. ANIANSSON. Numerical Calculations on the Kinetics of Stepwise Micelle Association. *J. Phys. Chem.*, **84**(7), 727–736 (**1980**).

[196] J. RASSING, P. J. SAMS, and E. WYN-JONES. Kinetics of Micellization from Ultrasonic Relaxation Studies. *J. Chem. Soc. Faraday Trans. 2*, **70**, 1247–1258 (**1974**).

[197] H. HOFFMANN, R. NAGEL, G. PLATZ, and W. ULBRICHT. Zur Kinetik der Mizellbildung von Alkylpyridiniumhalogeniden. *Colloid Polym. Sci.*, **254**, 812–834 (**1976**).

[198] E. A. G. ANIANSSON, S. N. WALL, M. ALMGREN, H. HOFFMANN, I. KIELMANN, W. ULBRICHT, R. ZANA, J. LANG, and C. TONDRE. Theory of the Kinetics of Micellar Equilibria and Quantitative Interpretation of Chemical Relaxation Studies of Micellar Solutions of Ionic Surfactants. *J. Phys. Chem.*, **80**(9), 905–922 (**1976**).

[199] H. HOFFMANN, R. LANG, D. PAVLOVIĆ, and W. ULBRICHT. Kinetic Measurements on Alkylammonium Halides. *Croat. Chem. Acta*, **52**(2), 87–103 (**1979**).

[200] P. MUKERJEE. Size Distribution of Small and Large Micelles. Multiple Equilibrium Analysis. *J. Phys. Chem.*, **76**(4), 565–570 (**1972**).

[201] A. OLEINIKOVA, I. BROVCHENKO, A. GEIGER, and B. GUILLOT. Percolation of Water in Aqueous Solution and Liquid-liquid Immiscibility. *J. Chem. Phys.*, **117**(7), 3296–3304 (**2002**).

[202] N. ŠEGATIN and C. KLOFUTAR. Thermodynamics of the Solubility of Water in 1-Hexanol, 1-Octanol, 1-Decanol, and Cyclohexanol. *Monatshefte für Chemie/Chemical Mon.*, **135**(3), 241–248 (**2003**).

[203] S. SCHÖTTL, D. TOURAUD, W. KUNZ, T. ZEMB, and D. HORINEK. Consistent Definitions of "The Interface" in Surfactant-free Micellar Aggregates. *Colloids Surfaces A Physicochem. Eng. Asp.*, **480**, 222–227 (**2015**).

[204] J. W. GIBBS. *The Scientific Papers of J. Willard Gibbs,* Vol. 1*, Thermodynamics*, page 219. New York: Dover Publications (**1961**).

[205] R. EVANS. The Nature of the Liquid-vapour Interface and Other Topics in the Statistical Mechanics of Non-uniform, Classical Fluids. *Adv. Phys.*, **28**(2), 143–200 (**1979**).

[206] M. KANDUČ, E. SCHNECK, and R. R. NETZ. Hydration Interaction Between Phospholipid Membranes: Insight into Different Measurement Ensembles from Atomistic Molecular Dynamics Simulations. *Langmuir*, **29**(29), 9126–9137 (**2013**).

[207] D. K. CHATTORAJ and K. S. BIRDI. *Adsorption and the Gibbs Surface Excess*, chap. 3, pages 47–51. New York: Plenum Press (**1984**).

[208] I. BENJAMIN. Molecular Structure and Dynamics at Liquid-liquid Interfaces. *Annu. Rev. Phys. Chem.*, **48**(1), 407–451 (**1997**).

[209] M. M. KOZLOV and M. WINTERHALTER. Elastic Moduli and Neutral Surface for Strongly Curves Monolayers. Analysis of Experimental Results. *J. Phys. II*, **1**(9), 1085–1100 (**1991**).

[210] T. ZEMB and P. CHARPIN. Micellar Structure from Comparison of X-ray and Neutron Small-angle Scattering. *J. Phys.*, **46**(2), 249–256 (**1985**).

[211] M. ZULAUF, K. WECKSTROM, J. HAYTER, V. DEGIORGIO, and M. CORTI. Neutron Scattering Study of Micelle Structure in Isotropic Aqueous Solutions of Poly (Oxyethylene) Amphiphiles. *J. Phys. Chem.*, **89**(15), 3411–3417 (**1985**).

[212] P. GUILBAUD and T. ZEMB. Solute-induced Microstructural Transition from Weak aggregates towards a Curved Film of Surface-active Extractants. *ChemPhysChem*, **13**(3), 687–691 (**2012**).

[213] M. M. KOZLOV, M. WINTERHALTER, and D. LERCHE. Elastic Properties of Strongly Curved Monolayers. Effect of Electric Surface Charges. *J. Phys. II*, **2**(2), 175–185 (**1992**).

[214] S. E. MUDIYANSELAGE, M. HAMBURGER, P. ELSNER, and J. J. THIELE. Ultraviolet A Induces Generation of Squalene Monohydroperoxide Isomers in Human Sebum and Skin Surface Lipids In Vitro and In Vivo. *J. Invest. Dermatol.*, **120**(6), 915–922 (**2003**).

[215] D. S. GOODMAN. Squalene in Human and Rat Blood Plasma. *J. Clin. Invest.*, **43**(7), 1480–1485 (**1964**).

[216] K. E. BLOCH. Sterol. Structure and Membrane Function. *Crit. Rev. Biochem. Mol. Biol.*, **14**(1), 47–92 (**1983**).

[217] C. B. FOX. Squalene Emulsions for Parenteral Vaccine and Drug Delivery. *Molecules*, **14**(9), 3286–3312 (**2009**).

[218] H. T. LU, Y. JIANG, and F. CHEN. Preparative Separation and Purification of Squalene from the Microalga Thraustochytrium ATCC 26185 by High-speed Counter-current Chromatography. *J. Chromatogr. A*, **994**(1-2), 37–43 (**2003**).

[219] C. D. WICK and T.-M. CHANG. Computational Observation of Pockets of Enhanced Water Concentration at the 1-Octanol/Water Interface. *J. Phys. Chem. B*, **118**(28), 7785–7791 (**2014**).

[220] I. BENJAMIN. Polarity of the Water/Octanol Interface. *Chem. Phys. Lett.*, **393**(4-6), 453–456 (**2004**).

[221] B. J. PALMER and J. LIU. Effects of Solute–Surfactant Interactions on Micelle Formation in Surfactant Solutions. *Langmuir*, **12**(7), 6015–6021 (**1996**).

[222] M. P. PILENI, T. ZEMB, and C. PETIT. Solubilization by Reverse Micelles: Solute Localization and Structure Perturbation. *Chem. Phys. Lett.*, **118**(4), 414–420 (**1985**).

[223] R. SANDER. Compilation of Henry's Law Constants (Version 4.0) for Water as Solvent. *Atmos. Chem. Phys.*, **15**(8), 4399–4981 (**2015**).

[224] N. MATUBAYASI, K. K. LIANG, and M. NAKAHARA. Free-energy Analysis of Solubilization in Micelle. *J. Chem. Phys.*, **124**(15), 154908–1–154908–13 (**2006**).

[225] S. SCHÖTTL and D. HORINEK. Salt Effects in Surfactant-free Microemulsions. *J. Chem. Phys.*, **148**(22), 222818–1–222818–5 (**2018**).

[226] P. M. GROSS. The "Salting Out" of Non-electrolytes From Aqueous Solutions. *Chem. Rev.*, **13**(1), 91–101 (**1933**).

[227] V. F. SERGEEVA. Salting-out and Salting-in of Non-electrolytes. *Russ. Chem. Rev.*, **34**, 309–318 (**1965**).

[228] F. HOFMEISTER. Zur Lehre von der Wirkung der Salze. *Arch. für Exp. Pathol. und Pharmakologie*, **25**(1), 1–30 (**1888**).

[229] W. KUNZ, P. LO NOSTRO, and B. W. NINHAM. The Present State of Affairs with Hofmeister Effects. *Curr. Opin. Colloid Interface Sci.*, **9**(1-2), 1–18 (**2004**).

[230] T. F. TADROS. *General Principles of Colloid Stability and the Role of Surface Forces,* in: *Colloid Stability. The Role of Surface Forces – Part I*, chap. 1. Weilheim: Wiley-VCH (**2007**).

[231] Y. CHEVALIER, L. BELLONI, J. B. HAYTER, and T. ZEMB. Effect of Interfacial Charge on Micellar Structure. *J. Phys.*, **46**(5), 749–759 (**1985**).

[232] P. JUNGWIRTH and D. J. TOBIAS. Specific Ion Effects at the Air/Water Interface. *Chem. Rev.*, **106**(4), 1259–1281 (**2006**).

[233] D. HORINEK, A. HERZ, L. VRBKA, F. SEDLMEIER, S. I. MAMATKULOV, and R. R. NETZ. Specific Ion Adsorption at the Air/Water Interface: the Role of Hydrophobic Solvation. *Chem. Phys. Lett.*, **479**(4-6), 173–183 (**2009**).

[234] N. SCHWIERZ, D. HORINEK, U. SIVAN, and R. R. NETZ. Reversed Hofmeister Series – the Rule Rather than the Exception. *Curr. Opin. Colloid Interface Sci.*, **23**, 10–18 (**2016**).

[235] J. N. ISRAELACHVILI. *Intermolecular and Surface Forces*, chap. 14, pages 326–331. Waltham: Elsevier, 3 edn. (**2011**).

[236] T. LOPIAN, S. SCHÖTTL, S. F. PRÉVOST, S. PELLET-ROSTAING, D. HORINEK, W. KUNZ, and T. ZEMB. Morphologies Observed in Ultraflexible Microemulsions with and without the Presence of a Strong Acid. *ACS Cent. Sci.*, **2**(7), 467–475 (**2016**).

[237] N. JAN. Large Lattice Random Site Percolation. *Phys. A Stat. Mech. its Appl.*, **266**(1-4), 72–75 (**1999**).

[238] S. TORQUATO and Y. JIAO. Effect of Dimensionality on the Continuum Percolation of Overlapping Hyperspheres and Hypercubes. II. Simulation Results and Analyses. *J. Chem. Phys.*, **137**(7), 1–24 (**2012**).

[239] D. STAUFFER and A. AMNON. *Introduction to Percolation Theory*, chap. 2, pages 15–34. London: Taylor & Francis, 2 edn. (**1991**).

[240] J. M. HAMMERSLEY and G. MAZZARINO. *Markov Fields, Correlated Percolation, and the Ising Model,* in: *The Mathematics and Physics of Disordered Media: Percolation, Random Walk, Modeling, and Simulation*. Berlin: Springer-Verlag (**1983**).

[241] M. J. POWELL. Site Percolation in Randomly Packed Spheres. *Phys. Rev. B*, **20**(10), 4194–4198 (**1979**).

[242] R. M. ZIFF and S. TORQUATO. Percolation of Disordered Jammed Sphere Packings. *J. Phys. A Math. Theor.*, **50**(8), 1–8 (**2017**).

[243] M. RINTOUL and S. TORQUATO. Precise Determination of the Critical Threshold and Exponents in a Three-dimensional Continuum Percolation Model. *J. Phys. A. Math. Gen.*, **30**(16), L585–L592 (**1997**).

[244] S. A. SAFRAN, I. WEBMAN, and G. S. GREST. Percolation in Interacting Colloids. *Phys. Rev. A*, **32**(1), 506–511 (**1985**).

[245] A. DE CANDIA, E. DEL GADO, A. FIERRO, N. SATOR, and A. CONIGLIO. Colloidal Gelation, Percolation and Structural Arrest. *Phys. A Stat. Mech. its Appl.*, **358**(2-4), 239–248 (**2005**).

[246] O. GEREBEN and L. PUSZTAI. Cluster Formation and Percolation in Ethanol-water Mixtures. *Chem. Phys.*, **496**, 1–8 (**2017**).

[247] B. CHEN and J. I. SIEPMANN. Microscopic Structure and Solvation in Dry and Wet Octanol. *J. Phys. Chem. B*, **110**(8), 3555–3563 (**2006**).

[248] M. BORKOVEC, H. EICKE, H. HAMMERICH, and B. D. GUPTA. Two Percolation Processes in Microemulsions. *J. Phys. Chem.*, **92**(1), 206–211 (**1988**).

[249] A. H. NARTEN, M. D. DANFORD, and H. A. LEVY. X-Ray Diffraction Study of Liquid Water in the Temperature Range 4-200° C. *Discuss. Faraday Soc.*, **43**, 97–107 (**1967**).

[250] G. HURA, D. RUSSO, R. M. GLAESER, T. HEAD-GORDON, M. KRACK, and M. PARRINELLO. Water Structure as a Function of Temperature from X-ray Scattering Experiments and Ab Initio Molecular Dynamics. *Phys. Chem. Chem. Phys.*, **5**(10), 1981–1991 (**2003**).

[251] G. W. STEWART and R. M. MORROW. X-ray Diffraction in Liquids: Primary Normal Alcohols. *Phys. Rev.*, **30**(3), 232–244 (**1927**).

[252] K. S. VAHVASELKÄ, R. SERIMAA, and M. TORKKELI. Determination of Liquid Structures of the Primary Alcohols Methanol, Ethanol, 1-Propanol, 1-Butanol and 1-Octanol by X-ray Scattering. *J. Appl. Crystallogr.*, **28**(2), 189–195 (**1995**).

[253] A. H. NARTEN and S. I. SANDLER. X-ray Diffraction Study of Liquid Tertiary Butyl Alcohol at 26° C. *J. Chem. Phys.*, **71**(5), 2069–2073 (**1979**).

[254] A. H. NARTEN and A. HABENSCHUSS. Hydrogen Bonding in Liquid Methanol and Ethanol Determined by X-ray Diffraction. *J. Chem. Phys.*, **80**(7), 3387–3391 (**1984**).

[255] B. E. WARREN. X-ray Diffraction in Long Chain Liquids. *Phys. Rev.*, **44**(12), 969–973 (**1933**).

[256] N. P. FRANKS, M. H. ABRAHAM, and W. R. LIEB. Molecular Organization of Liquid n-Octanol: an X-ray Diffraction Analysis. *J. Pharm. Sci.*, **82**(5), 466–470 (**1993**).

[257] M. DUVAIL, J.-F. DUFRÊCHE, L. ARLETH, and T. ZEMB. Mesoscopic Modelling of Frustration in Microemulsions. *Phys. Chem. Chem. Phys.*, **15**(19), 7133–7141 (**2013**).

[258] B. HAYTER, M. HAYOUN, and T. ZEMB. Neutron Scattering Study of Pentanol Solubilization in Sodium Octanoate Micelles. *Colloid Polym. Sci.*, **262**(10), 798–803 (**1984**).

Acknowledgments

First of all, I would like to thank my supervisor Prof. Dr. Dominik Horinek for the opportunity of this PhD study. I highly appreciate the pleasant working climate and the amicable cooperation that made this doctorate not only an academic endeavor, but a truly enjoyable experience. Thank you for taking the time for countless discussions, the support during two theses, and many expert advice!

I would also like to take the opportunity to thank Prof. Dr. Thomas Zemb for many a fruitful exchange of ideas and for readily agreeing on reviewing this thesis and traveling to Regensburg for an examination.

Still, the past few years might have been a strenuous business were it not for my colleagues in the office. Our area of studies naturally involves a substantial amount of screen handling and anyone who has ever worked with computers for extended periods of time knows very well how good these machines can be at innocently and most frustratingly misinterpreting one's instructions. This makes it all the more important to be surrounded by co-workers that from time to time provide some diversion and a much needed change of perspective. For this I want to thank my teammates Ragnheiður Guðbrandsdóttir, Christoph Hölzl, and Maximilian Hahn, as well as my former colleague and advisor Beate Möser. My thanks also goes to all the guest researchers and students who joined us for projects over the years and brought more variety to our everyday work.

Based on personal experience, writing a scholarly manuscript appears to be governed by a hitherto little-explored law of nature that introduces a fair degree of uncertainty in spelling, grammar, and overall coherency. For this reason, I want to express my most sincere gratitude to my brother Andreas Marquardt, and my friends Johannes Stigloher and Johannes Ziegler for critically proof-reading this document and decorating the text with not too few indications of odd phrasings and orthographic mistakes.

Finally yet importantly, I want to thank my family: It is impossible to keep track of all the occasions on which you not only offered helpful advice, but unconditional support. And what makes this even more valuable is that I know I don't need to.

Eidesstattliche Erklärung

(1) Ich erkläre hier mit an Eides statt, dass ich die vorliegende Arbeit ohne unzulässige Hilfe Dritter und ohne Benutzung anderer als der angegebenen Hilfsmittel angefertigt habe; die aus anderen Quellen direkt oder indirekt übernommenen Daten und Konzepte sind unter Angabe des Literaturzitats gekennzeichnet.

(2) Bei der Auswahl und Auswertung folgenden Materials haben mir die nachstehend aufgeführten Personen in der jeweils beschriebenen Weise entgeltlich/unentgeltlich geholfen:

1. .....
2. .....
3. .....

(3) Weitere Personen waren an der inhaltlich-materiellen Herstellung der vorliegenden Arbeit nicht beteiligt. Insbesondere habe ich hierfür nicht die entgeltliche Hilfe eines Promotionsberaters oder anderer Personen in Anspruch genommen. Niemand hat von mir weder unmittelbar noch mittelbar geldwerte Leistungen für Arbeiten erhalten, die im Zusammenhang mit dem Inhalt der vorgelegten Dissertation stehen.

(4) Die Arbeit wurde bisher weder im In- noch im Ausland in gleicher oder ähnlicher Form einer anderen Prüfungsbehörde vorgelegt.